VOLCANIC ASH CLOUD HEIGHTS USING THE MODIS CO_2-SLICING ALGORITHM

by

Michael S. Richards

A thesis submitted in partial fulfillment of the requirements for

the degree of

Master of Science

(Atmospheric and Oceanic Sciences)

at the

UNIVERSITY OF WISCONSIN - MADISON

2006

APPROVED: Steven Ackerman DATE: 1/03/06

Steven Ackerman, Ph.D., CIMSS Director

Abstract

To make accurate volcanic ash cloud dispersion forecasts, certain parameters, including the altitude of the volcanic cloud, must be known. There are several methods used for estimating the height of an ash cloud, including correlation with ground-based video, correlation with wind data, cloud-shadow geometry, and the space-borne "11μm brightness temperature" technique. We introduce the Moderate Resolution Imaging Spectroradiometer (MODIS) "CO_2-slicing" technique as a method for retrieving volcanic cloud heights from space. This paper compares the heights retrieved from the CO_2-slicing method with heights estimated by the aforementioned methodologies, as well as height products from the Multiangle Imaging SpectroRadiometer (MISR). This paper also suggests a cloud emissivity correction to the CO_2-slicing algorithm in consideration of volcanic ash clouds

CO_2-slicing heights are found to agree well with operational methodologies for the majority of cases investigated in this study. For two stratospheric volcanic ash clouds, CO_2-slicing heights were within the height estimate window determined by operational methods. Six tropopause cases were investigated and the CO_2-slicing height retrievals were found to be within ±25hPa for two of the cases, with a third yielding a CO_2-slicing estimate within ±50hPa. Height retrieval comparisons with MISR's stereo height retrieval algorithm, including a pixel-to-pixel comparison of the two methods, show the MODIS CO_2-slicing height product to generally underestimate the height of the volcanic ash clouds; however, variability in the two data sets is similar. The CO_2-slicing methodology is determined to

under-perform when retrieving heights for 1) lower-altitude volcanic ash clouds and 2) optically thin volcanic ash clouds.

A cloud emissivity correction is also applied to the CO_2-slicing algorithm. A cloud emissivity ratio of 1.07 is used for the MODIS band36/band35 channel combination, and a ratio of 0.93 is substituted for the remaining four channel pairs. These emissivity adjustments raise the CO_2-slicing heights for fourteen of fifteen volcanic ash clouds, with an average increase of 755.4 meters.

Acknowledgements

The work that is presented in this paper would not have been possible without the help of the following individuals. I would like to thank my advisors Dr. Steve Ackerman and Wayne Feltz for giving me the opportunity to take on this project and for directing me through to its completion. I would also like to thank all at the Space and Science Engineering Center, the Cooperative Institute for Meteorological Satellite Studies, and the Department of Atmospheric and Oceanic Studies at the University of Wisconsin-Madison for providing a friendly and professional atmosphere that has truly been a pleasure to work in. Specifically, I would like to recognize Dr. Bryan Baum for his patience and willingness to lend insight into the details of the CO_2-slicing algorithm, as well as Liam Gumley, Kathy Strabala, and Richard Frey for their help in answering my MODIS and computer coding questions. I also wish to recognize Mike Pavolonis for his willingness to share his knowledge and research on volcanic ash.

This thesis is a compilation of cases whose completion required the assistance of numerous individuals across the globe. This author wishes to recognize Andrew Tupper of the Darwin Volcanic Ash Advisory Centre, Australia for his unbelievable help in analyzing many of the volcanic eruptions presented in this work, as well as for sharing his sources, data, and personal knowledge that truly made this study possible. In addition, this author wishes to recognize Catherine Moroney of the Jet Propulsion Laboratory in Pasadena, California, for her continuing patience in answering MISR questions, as well as her willingness to take time out of her own work to crunch new data for me. I would like to thank Sergey Senyukov of the Research Laboratory of Seismic and Volcanic Activity, Kamchatkan Experimental-Methodical Seismological Department, Russia for sharing his data and new, unpublished technique on the estimation of volcanic ash plumes. I would also like to thank Yasuhiro Kamada of the Tokyo Volcanic Ash Advisory Centre for his assistance with the Sheveluch eruption of 21 May 2001. Also presented in this study is an as-yet unpublished pixel-to-pixel MODIS/MISR comparison algorithm that was written at this point in time to facilitate work presented in this paper. For this, I would sincerely like to acknowledge the code's author Mike Garay of the Jet Propulsion Laboratory.

The foundation of this work is a CO_2-slicing algorithm version written by Greg McGarragh at the SSEC/CIMSS, University of Wisconsin-Madison (now with the NASA Langley Research Center). To Greg, I wish to extend a sincere 'thank you' for his extreme patience and assistance in helping me understand the code, as well his very prompt replies to questions and his willingness to take time to adjust his work to accommodate mine.

This research was supported by the NASA LaRC Subcontract #4400071484.

Table of Contents

I. Introduction ……………………………………………………………………………. 1

II. Direct impacts of volcanic ash on aircraft …………………………………………... 5

III. Current methods for estimating volcanic ash cloud height …………………………… 8

IV. The Moderate Resolution Imaging Spectrometer (MODIS) ………………………... 17

V. CO_2-slicing algorithm at 1000-meter resolution ……………………………………... 21

VI. The Multi-angle Imaging SpectroRadiometer (MISR) ……………………………... 32

VII. MISR height retrieval ……………………………………………………………… 36

VIII. CO_2-slicing heights compared with MISR heights ……………………………….. 40

IX. CO_2-slicing heights compared

with operational height estimation methods …………………………………….. 53

X. CO_2-slicing heights compared with

heights estimated by video and photographic techniques ………………………... 65

XI. Changes to the CO_2-slicing methodology in consideration of volcanic ash ………... 69

XII. Conclusions and Future Work ……………………………………………………... 77

XIII. References ………………………………………………………………………… 82

XIV. Appendices ………………………………………………………………………... 88

I. Introduction

Volcanic ash suspended in the atmosphere poses significant threats to aviation. The problems posed by airborne volcanic ash are not limited to the relatively minor financial and aircraft coordination inconveniences sustained by airlines when diversion around ash clouds is necessary. Rather, threats include loss of life that can occur with flight into airborne volcanic ash clouds, as well as the significant financial liabilities incurred with severely damaged aircraft, both of which may be direct results of airborne encounters with ash.

Due to the hazards posed by airborne volcanic ash, detection, monitoring, and the forecasting of the position of volcanic eruption clouds is necessary to ensure aircraft and passenger safety. Figure 1 shows how significant the volcanic ash cloud threat is to aviation, as the major North Pacific air routes come close to over 100 potentially active volcanoes. Between 1985 and 2000, over 100 jet aircraft were damaged due to unexpected encounters with volcanic ash, and the financial cost to commercial aircraft due to volcanic ash is estimated to have surpassed $250(US) (Simpson et al., 2000a). Avoidance of ash might be a relatively trivial issue when in close proximity to an erupting volcano in clear skies. However, volcanic ash is a significant hazard even at far distances from the eruption (Casadevall, 1994). While an ash plume emitting from a volcano might be easily recognizable in clear skies due to its location and visual attributes, the ash cloud might become difficult to recognize as it drifts from its source, loses particle concentration due to fallout, and possibly mixes with water and/or ice clouds. While the U.S. military considers mass loadings of greater than 50 milligrams per cubic meter a potential hazard to their aircraft (Prata and

Grant, 2001), it is not publicly known what ash particle concentrations are safe for jet engines. These problems are compounded by the fact that, at present, radar onboard commercial aircraft is not able to detect airborne volcanic ash (Simpson et al., 2000a). In order to ensure safety, complete avoidance of airborne volcanic ash is required (Casadevall, 1994).

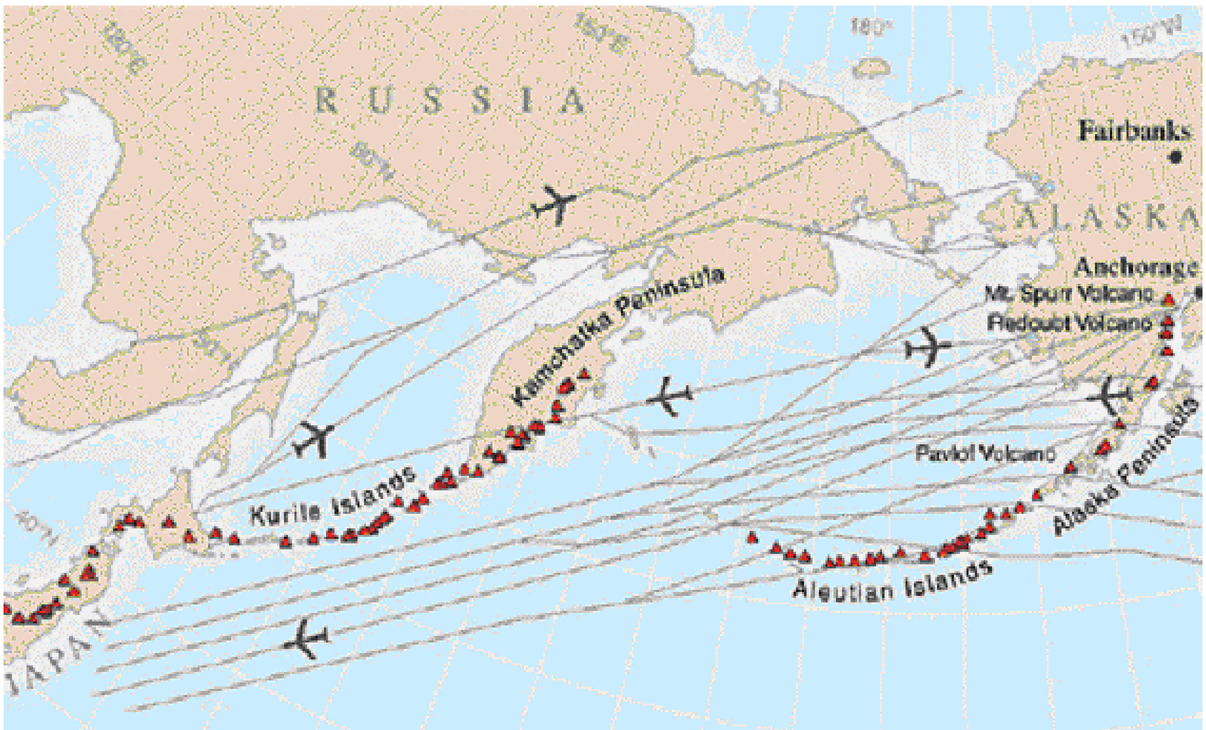

Figure 1. North Pacific and Russian Far East air routes (gray lines) pass over or near more than a hundred potentially active volcanoes (red triangles). *Image and caption courtesy of the Alaska Volcano Observatory.*

Routing aircraft around a volcanic ash cloud requires knowledge of the ash cloud's location in a three-dimensional space and at a specific time. If dangerous regions of an ash cloud could be accurately bounded and identified, avoidance would be relatively simple and cost effective. Unfortunately, accurately flagging volcanic ash in three-dimensional space is difficult. Numerous methods have been developed that utilize space-borne instrumentation to recognize and locate airborne ash. One approach (e.g. Prata, 1989a and 1989b) utilizes the 11µm and 12µm infrared channels available to numerous space-borne sensors, including the Moderate Resolution Imaging Spectrometer (MODIS). Although this method has limitations (Rose et al., 2000; Simpson et al., 2000a; Prata et al., 2001), it does, under certain conditions, allow ash to be "masked out" of images created from space-borne instruments, highlighting volcanic aerosols and effectively producing a "map" of volcanic ash in the atmosphere. This map, however, is two-dimensional, and it yields no information on the height or base of volcanic ash clouds. At present, there are several satellite cloud height estimation techniques that may be used when attempting to determine the height of volcanic ash clouds, and these will be discussed in a later section of this study. Although accurate height estimation is, in theory, possible, it does not address the question of how thick the cloud is (what is its base?). Although there is no space-borne technique currently available to determine the base of a volcanic ash cloud, "most commercial (aircraft) operators will not knowingly fly underneath an ash cloud" (Andrew Tupper – personal communication). With current methods (Figure 2) not allowing the three-dimensional bounding of dangerous regions of volcanic ash, the significance of knowing the height of volcanic ash clouds might seem to diminish. The knowledge of cloud height is, however, essential to accurate forecasting of cloud position.

This paper investigates the potential of the "CO_2-slicing" methodology in determining the height of volcanic ash plumes. While the CO_2-slicing algorithm has been validated for accurate height estimates of meteorological clouds to within ±50hPa (Menzel et al., 1983; Wylie and Menzel, 1989; Platnick et al., 2003) for many cases, it has not been applied specifically to volcanic scenes. Using the CO_2-slicing algorithm applied to MODIS data, this paper compares the CO_2-slicing results with results obtained by current volcanic cloud height estimate methods, as well as height estimates obtained by the Multiangle Imaging SpectroRadiometer (MISR).

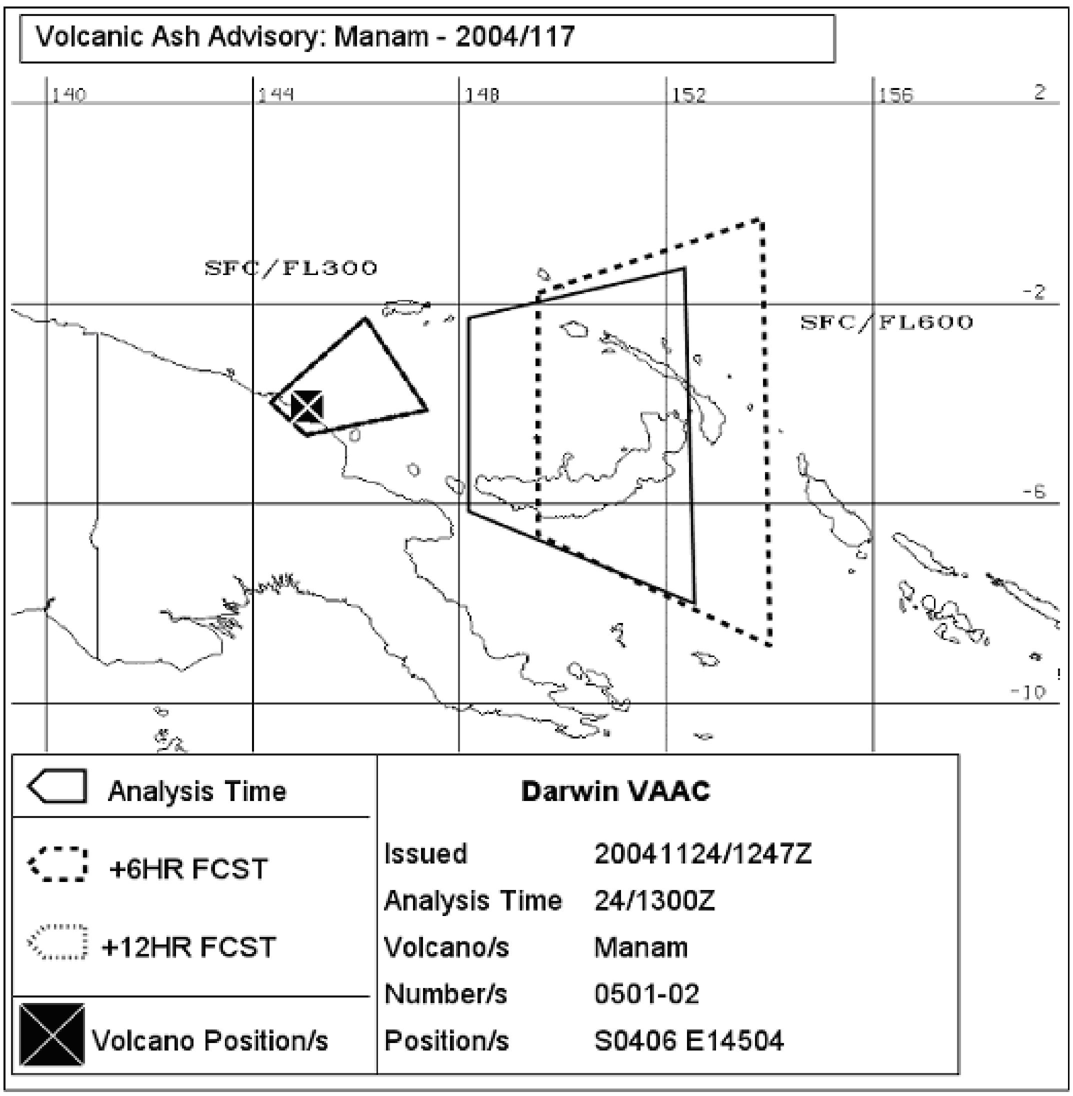

Figure 2. Example of current three-dimensional ash cloud forecast product put out by the Darwin VAAC. Regions where ash is expected to be presented are bounded two-dimensionally. Altitudes to be avoided are also included. *Image courtesy of Darwin VAAC.*

II. Direct impacts of volcanic ash on aircraft

The hazards that volcanic ash suspended in the atmosphere poses to aviation have been well documented (Casadevall, 1994; Casadevall and Krohn, 1995; Grindle and Burcham, 2002; Johnson and Casadevall, 1994; Rossier, 2002), and examples are provided in Figures 3 and 4. Perhaps the most familiar risk ash clouds pose to aircraft is that of engine flameout. When ash is encountered in high enough concentrations and ingested by a jet engine, the high contrasts in temperature inside the engine provide an environment that will cause the solid ash particles to melt and then resolidify, resulting in a "choking off" of the engine. Ash particles might also plug vital fuel pathways, ultimately resulting in engine flameout (Rossier, 2002). In 1989, a KLM 747-400 encountered a volcanic ash cloud while descending through 25,000 feet, seventy miles from Anchorage, Alaska. The cloud, which appeared to the flight crew to be nothing out of the ordinary, was the result of a volcanic eruption from the Redoubt volcano, located 110 miles west-southwest of Anchorage, on the previous day. Soon after entering the volcanic cloud, the flight crew began a high-powered climb, with all four aircraft engines failing fifty-eight seconds later. As the aircraft descended with no working flight deck instrumentation or electrical systems, all four engines were restarted as the aircraft passed through 13,000 feet. Not all airborne encounters with volcanic ash clouds cause immediate, life-threatening damage. On February 27, 2000, a DC-8 research aircraft operated by the National Aeronautics and Space Administration (NASA) inadvertently flew through the edge of a volcanic ash cloud for seven minutes. While all in-flight instrumentation reported no problems with the engines, all four engines were eventually disassembled and inspected. Thorough inspection of the engines reveled clogged turbine blade cooling passages and erosion of the leading-edge blade coating on some of the engines' blades (Grindle and Burcham, 2002). This flight was evidence of the major aircraft engine damage that can occur even with minimal contact with suspended volcanic ash.

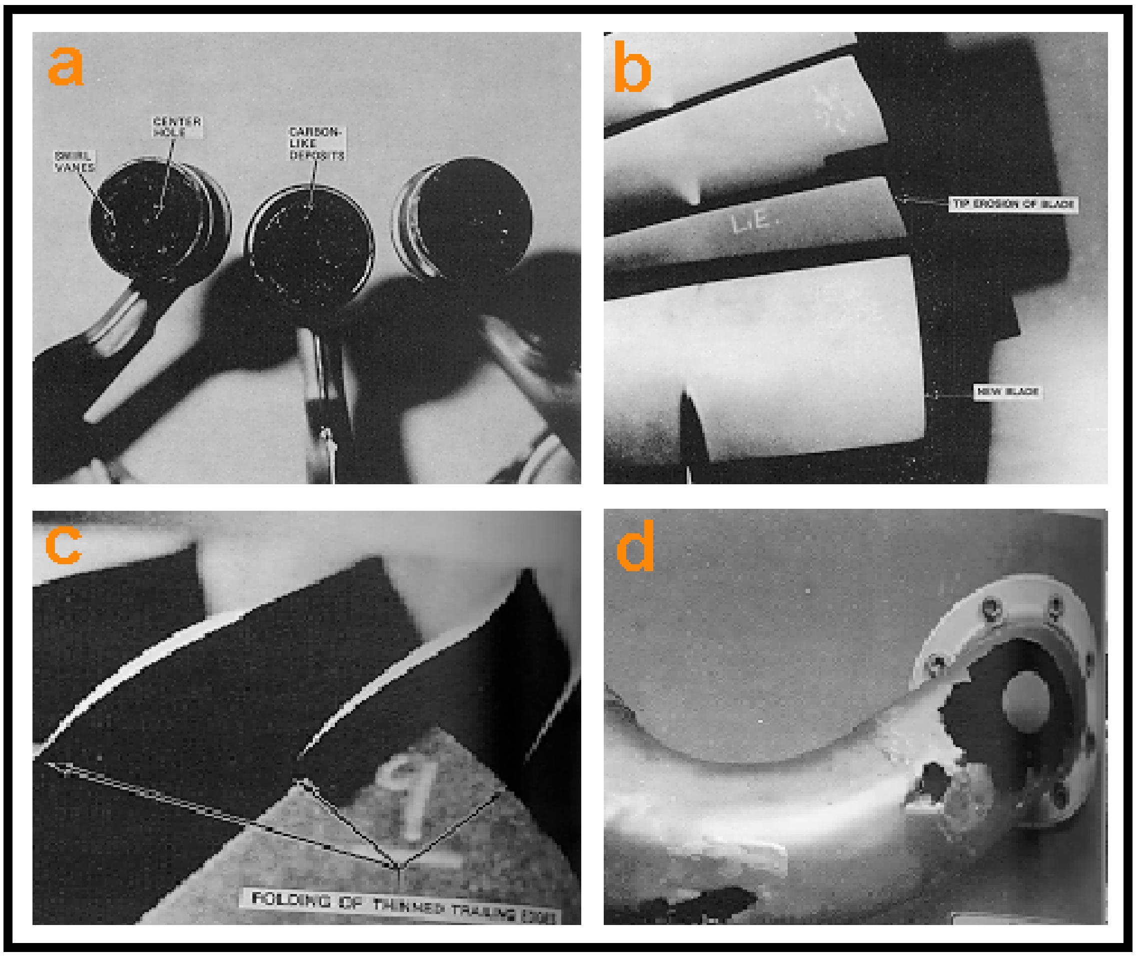

Figure 3. Damage to aircraft parts caused by volcanic ash. a) Fuel nozzles with the swirl vanes, center hole and carbon like deposits labeled. The center hole of the nozzle, from which the fuel is sprayed, was opened and capable of passing fuel at the design flow rate however, the swirl vanes were plugged, thus inhibiting atomization of the fuel; b) The lower blade of the second-stage fan is new, while the upper blades show erosion caused by ash. Throughout the compressor, tip-region erosion occurred on almost every stage; c) High-pressure compressor ninth-stage rotor. This shows an example of the ninth-stage compressor blade row. The trailing edge of the airfoil in the tip region became so thin that the material folded away from the pressure surface; d) Environmental control system plumbing showing erosion of duct walls. Scale in inches. *Images and caption taken from Dunn and Wade (1994).*

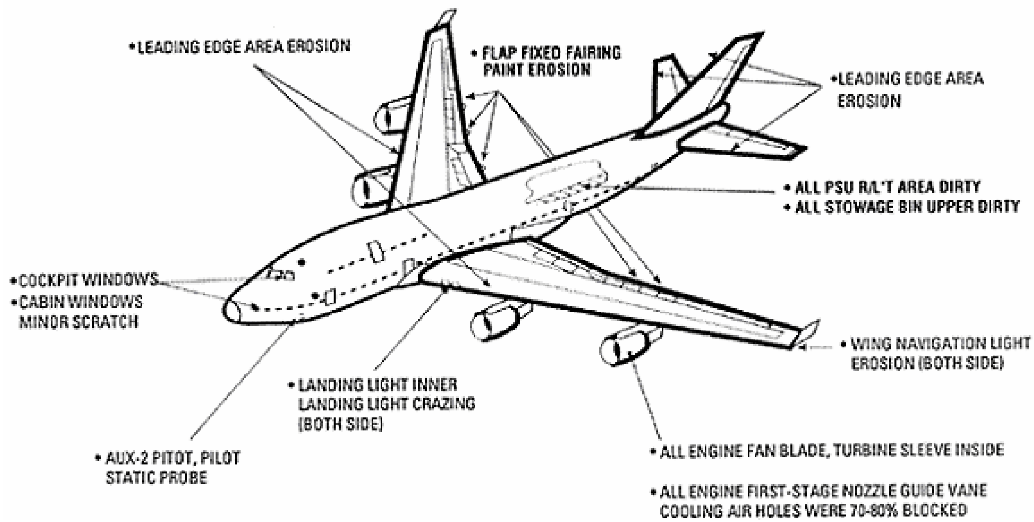

Figure 4. Damage to exterior surfaces of a 747-400 jumbo jet following an encounter with the June 15, 1991, ash cloud from Mount Pinatubo. *Image and caption taken from Casadevall et al. (1996).*

Engine damage is not the only significant threat posed to aviation by volcanic ash. Any aircraft surface that is exposed to volcanic ash can be damaged. Potential damage includes clogged cooling ducts, which leads to overheating and failure of vital electronics, and damaged exterior instrumentation, which can effect air data computers and the pilot-static system (Rossier, 2002). Another vital aircraft surface that is highly susceptible to ash cloud encounters are the cockpit windows. Flight through ash has the effect of "sandblasting", and even at relatively low airspeeds, this sandblasting of the cockpit windows can make it difficult or impossible for a flight crew to see forward (Rossier, 2002). In addition to physical dangers posed by volcanic ash, loss of aircraft communication can occur when a volcanic cloud envelops an aircraft. This loss of communication is due to the electrical charge that is generated by the volcanic ash, which can lead to problems sending or receiving radio messages (Rossier, 2002).

III. Current methods for estimating volcanic ash cloud height

Volcanic ash cloud heights can be estimated using both space-borne and ground based techniques. At present, the most common methodology for ash cloud height estimation is correlating atmospheric profiles with infrared brightness temperatures (BT) retrieved from satellites (Tupper et al., 2003). There are limitations to this method, however, and BT estimations are often supplemented with height estimates based on wind correlations, which may themselves be sufficient to give reasonable height estimates (Tupper et al., 2003). Another height estimation method that is dependant on space-borne instrumentation is the visible shadow method, which makes use of any visible shadow cast by the ash cloud/plume. There are scenes, however, where space-borne methods are useless due to overlying cloud or insufficient instrument resolution. In those cases, height estimates must be made by ground or air based methods. Outside of scientific investigations, air reports are limited to pilot reports from commercial, military, and general aviation. Ground-based height estimates are made utilizing several different methods, including weather radar and lidar (e.g. Lacasse et al., 2004; Tupper et al., 2004), as well as video (e.g. Sparks and Wilson, 1982) and seismic (e.g. McNutt, 1994) equipment.

Satellite brightness temperature method

Ash cloud height estimation using the BT-method (Holasek et al., 1996; Sawada, 1987; Oppenheimer, 1998; Prata and Grant, 2001; Tupper et al., 2004) is a relatively simple task. Brightness temperatures retrieved from the ash cloud (normally utilizing the 11μm window channel) are compared against the local atmospheric temperature profile (Figure 5). The altitude at which the retrieved BT matches the atmospheric temperature profile is considered to be the height of the ash cloud. Oppenheimer (1998) showed that there are several potential limiting factors to this technique. The first lies in the assumption that the ash cloud emissivity is unity. Using this assumption, brightness temperature retrievals for thick ash clouds may closely approximate the true brightness temperatures of the ash cloud. However, should the cloud be thin, the space-borne instrument will detect radiation from beneath the ash cloud, effectively lowering the heights. The second limiting factor lies in the assumption of thermal equilibrium. This method assumes that the ash cloud top is in thermal equilibrium with the ambient air (Oppenheimer, 1998). Should the ash plume have overshot its thermally equilibrated level, or should the ash plume still have sufficient energy to carry it to a higher altitude after the time of the satellite image, the BT-method will begin to break down. Another difficult issue with the BT technique involves the assumed atmospheric temperature profile. Errors in the height estimation will occur whenever the assumed atmospheric profile does not represent the true atmospheric state of the volcanic scene. A fourth limiting factor, put forth by Prata and Grant (2001), suggests that since temperature changes with height are very small near the tropopause, there will be indeterminacy in the height estimates.

Wind correlation method

Volcanic ash cloud heights are also estimated by correlating cloud movement with atmospheric winds (Holasek et al., 1996; Lynch and Stephens, 1996; Oppenheimer, 1998; Tupper et al, 2004). This method takes advantage of vertical wind profiles in the troposphere and lower stratosphere are often quite different. Thus, the horizontal wind component at any given altitude will likely be unique in its direction and/or speed as compared to horizontal wind components at neighboring altitudes. Airborne ash will move downwind with a rate and direction "closely matching the prevailing wind" (Lynch and Stephens, 1996). If the direction and speed of the airborne ash cloud can be determined with confidence, an estimation of its height is made by matching the ash cloud "vector" with the corresponding wind "vector", assuming the altitude of the wind vector to be that of the ash cloud.

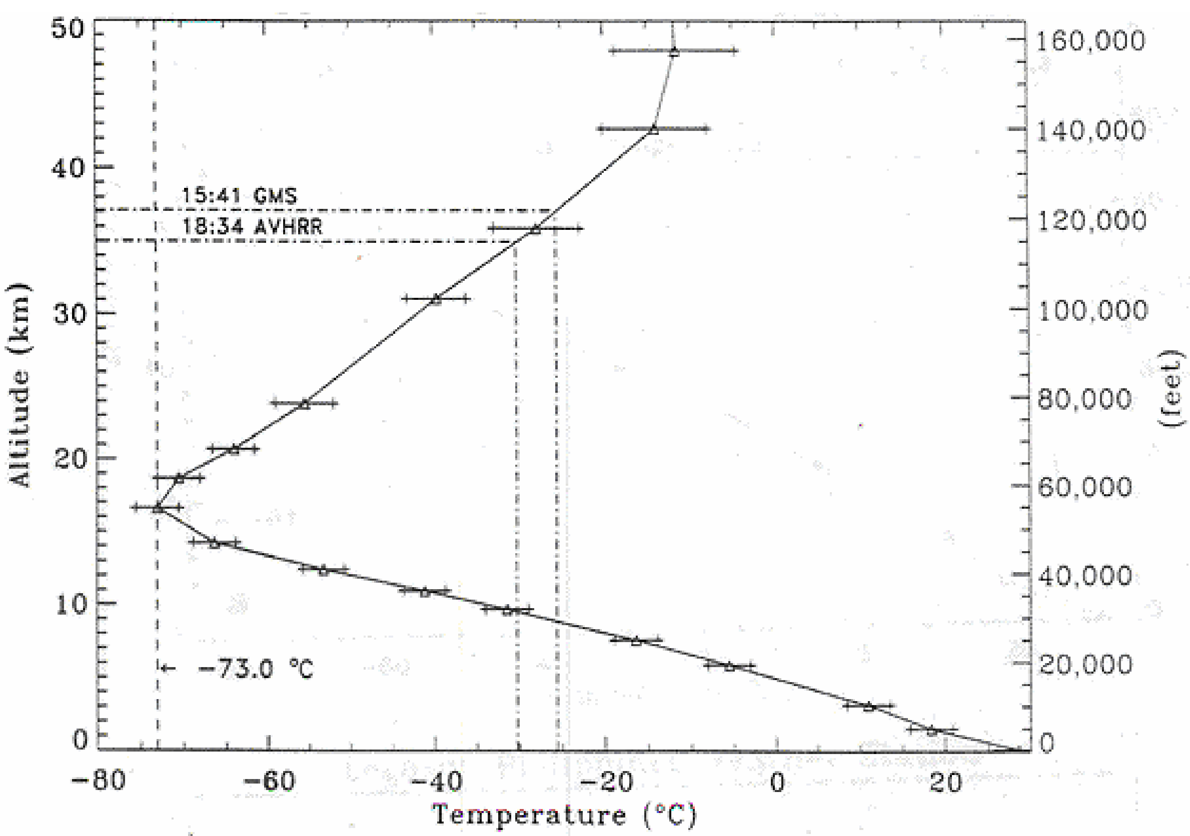

Figure 5. Comparison of satellite derived brightness temperatures and a local temperature profile. In this example, a brightness temperature of approximately –30°C, derived by the Advanced Very High Resolution Radiometer (AVHRR) at 1834Z, indicates an altitude of approximately 35 kilometers. *Image taken from Holasek et al. (1996).*

Shadow method

It is possible to estimate the height of the edge of a volcanic cloud using a geometric technique (Holasek et al., 1996; Oppenheimer, 1998; Simpson et al., 2000b; Prata and Grant, 2001) should the ash cloud cast a visible shadow on the underlying Earth's surface. To make heights estimates using this technique, data regarding the underlying terrain, as well as satellite viewing and sun angle information, must be known. A complete description of a height-from-shadow methodology can be found in Prata and Grant (2001); the geometry for this method has been reproduced in Figure 6, with height *h* defined by

$$h = \frac{d}{\sqrt{X^2 - Y^2}} \qquad \{1\}$$

where

$$X = \cos\phi \tan\theta - \cos\phi_0 \tan\theta_0 \qquad \{2\}$$

$$Y = \sin\phi \tan\theta - \sin\phi_0 \tan\theta_0 \qquad \{3\}$$

and *d* is the magnitude of vector **Δ**.

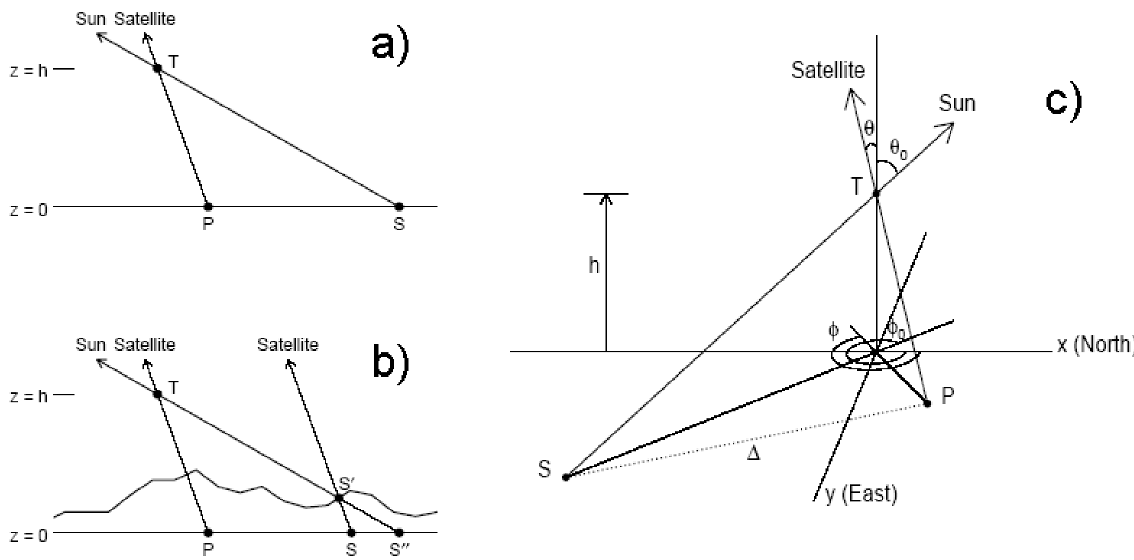

Figure 6. Height-from-shadow geometry. View and sun directions are in same vertical plane for cases of ocean (a) and over land (b). Point **T** is the plume edge, which casts its shadow at point **S** on the water surface (sea level). Point **P** is the position of **T** as it is projected along the satellite view direction to the surface. Point **S′** is the shadow cast by **T** on land, and point **S″** is the projection to sea level of **S′** along the sun view direction. For the higher detail geometry for ocean cases (c), θ angles represent zenith angle and ϕ angles represent azimuth angles. Distance **h** represents the altitude of the ash cloud edge (point **T**) above sea level (asl). *Images taken from Prata and Grant (2001).*

In addition, should the visible shadow from a volcanic cloud fall on an underlying meteorological cloud, the volcanic cloud height may be assessed if the height of the meteorological cloud is known (Oppenheimer, 1998). There are several trouble areas in this methodology, however. Prata and Grant (2001) apply their shadow technique separately over ocean and land. This height estimation technique is relatively simple when the shadow is cast on a uniform ocean surface.

Increased complexity occurs, however, when the shadow falls onto land, where the change in slope and elevation of the underlying surface must be taken into consideration when applying this geometric technique. Other trouble areas in this methodology, as put forth by Oppenheimer (1998), include cases where the volcanic clouds are at high elevation, the satellite scan angle is quite large, or the satellites themselves are in lower orbits. In these cases, parallax “can be significant” and should be taken into consideration. Several comparisons have been made between shadow-estimated heights and BT-estimated heights. Glaze et al. (1989) found relatively large differences between the two methods (Figure 7). However, another study done by Holasek et al. (1996) found both height estimation methods to agree closely. Oppenheimer (1998) suggests both cases were influenced by the limiting factors in the BT-estimation methodology. Tupper et al. (2004), while investigating the Ruang eruption of 24-26 September 2002, found relatively high differences between the two methods, as well as differences between the shadow-height estimations from different space-borne platforms. Tupper et al. (2004) estimated volcanic ash cloud heights to be approximately 21.5 kilometers using MODIS data and the shadow-height estimation methodology outlined in Prata and Grant (2001). Shadow-height estimations using Geostationary Meteorological Satellite 5 (GMS5) Visible Infrared Spin-Scan Radiometer (VISSR) data, utilizing an approximate shadow-height estimation method, yielded heights of approximately 18.7 kilometers. BT-estimation heights for this eruption were approximately 16 kilometers, but Tupper et al. (2004) notes that the minimum brightness temperature indicates that the eruption cloud was near or above the tropopause. For cases where stratospheric overshoot occurs above an anvil, the shadow technique only works when the height of the overshoot shadow (which casts its shadow on the anvil) can be added to the height of the anvil (which casts it shadow on the earth’s surface).

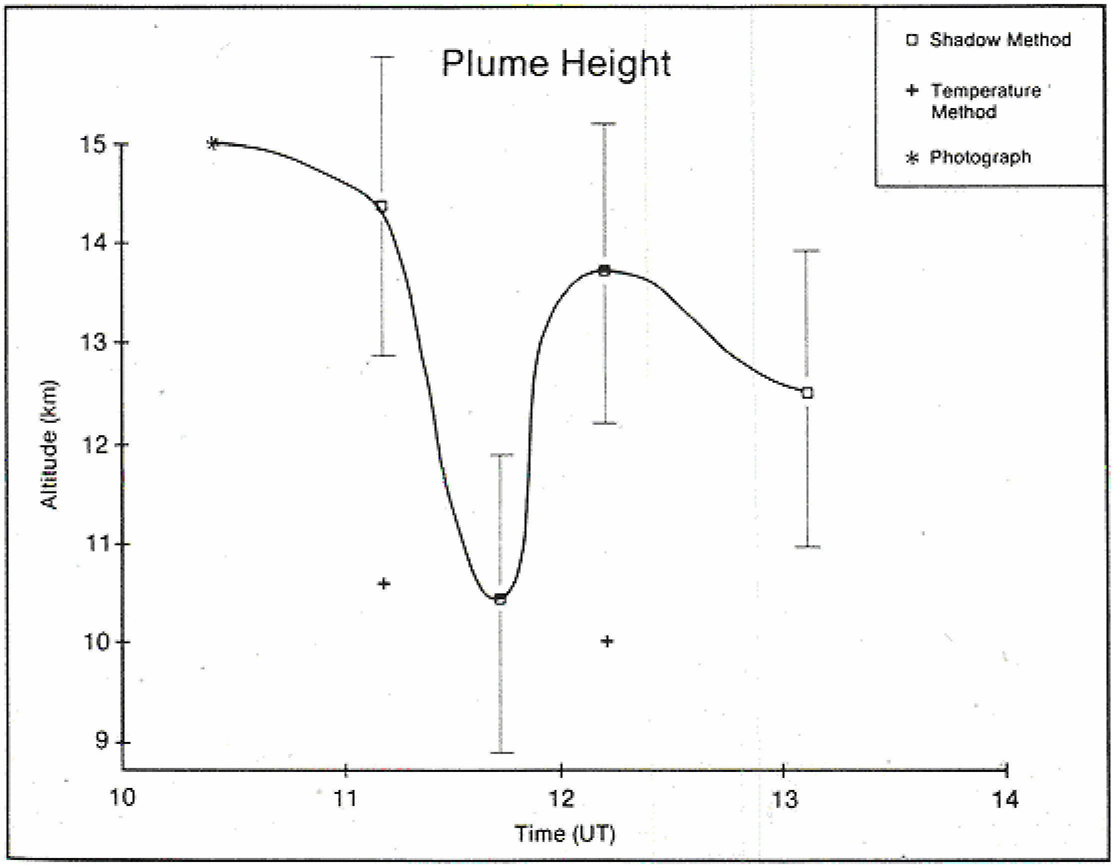

Figure 7. Heights retrieved by Glaze et al. (1989) for an eruption plume from the Lascar volcano (Chile) in 1986. Difference between heights retrieved by the BT-method and the shadow-method are approximately 4 kilometers. Error bars of 1.5 kilometers have been fitted to the shadow measurements. *Image taken from Glaze et al. (1989).*

Radar and lidar methods

Ground-based weather radar (Figure 8) has been used to detect the heights of volcanic ash clouds (Lacasse et al., 2004; Tupper et al., 2004; Tupper et al., 2005). This study will not discuss the specifics of the radar cloud height algorithm; for an extensive description of an algorithm used to determine meteorological cloud heights using weather radar, the reader is referred to Clothiaux et al. (2000). It is important, however, to note some of the limitations of this method, as discussed in Tupper and Kinoshita (2003). Because ground radar stations have limited range, the number of volcanic eruption clouds that pass within "reach" of a ground-based weather radar is quite limited. Radar stations are quite expensive as well, limiting the number of radar stations available worldwide. Radar estimates are also limited by requiring the ash cloud to consist of certain particle sizes. Should an ash cloud consist of only small particles, it may be invisible to weather radar. Also, heavy precipitation can obscure radar height retrievals. Lidar, which measures the backscatter intensity of a laser signal, has also been used to estimate volcanic cloud heights (Tupper et al., 2004).

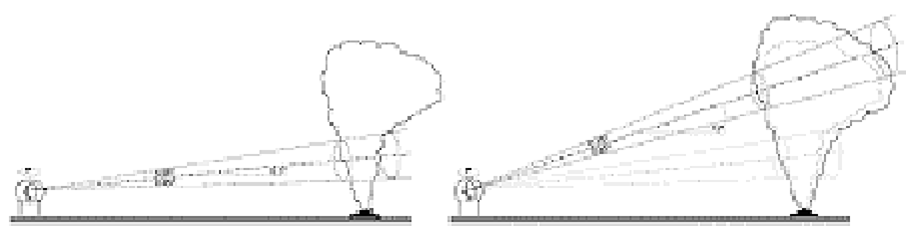

Figure 8. Diagram illustrating radar scan of a volcanic eruption. *Edited, original image taken from Lacasse et al. (2004).*

Video and seismic methods

Additional methods for estimating ash cloud heights utilize video and seismic instrumentation. Volcanic plume heights may be estimated using a geometric video technique (e.g. Sparks and Wilson, 1982). In their investigation, Sparks and Wilson (1982) use their calculated heights to assist in the estimation of other volcanic parameters including particle content and volume discharge rate of magma. While they acknowledge errors can occur when plumes stray from the vertical plane above the volcanic vent, they estimate that dimensions estimated in their study are "better than 2 percent." Volcanic ash plume heights may also be estimated/forecast by analyzing volcanic tremor data (McNutt, 1994). McNutt (1994) concludes that 'explosivity of eruptions', which is based on parameters such as ash-column height, is proportional to the amplitude of volcanic tremor (normalized to a common scale).

Pilot reports

Pilot reports (PIREPs) from commercial, general and military aircraft can be important sources of ash cloud height information. They are also vital to the safety of all aviation as PIREPs are often the first to inform of volcanic eruptions (Tupper and Kinoshita, 2003). Unfortunately, PIREPs have been known to inaccurately report cloud top information and/or be contradictory with other sources of data (Simpson et al., 2002; Tupper and Kinoshita, 2003; Tupper et. al., 2003). In general, pilot reporting is limited to daytime and good visibility conditions (visibility immediately following an eruption might be quite poor).

IV. The Moderate Resolution Imaging Spectrometer (MODIS)

The Moderate Resolution Imaging Spectrometer (MODIS) (Figure 9) was developed for the Terra and Aqua satellites of the National Aeronautics and Space Administration's (NASA) Earth Observing System (EOS). Soon after the successful launch of the Terra spacecraft on December 18, 1999, MODIS began acquiring data, with its science data stream beginning on February 24, 2000. A second MODIS instrument was launched with EOS' Aqua platform on May 4, 2002. Since this time, two MODIS instruments have observed the Earth, with each instrument providing global coverage every two days (Platnick et al., 2003). The spectral coverage, as well as the global spatial coverage that MODIS offers has yielded both new and improved space borne remote sensing algorithms (e.g. King et al., 2003; Platnick et al, 2003; Seemann et al., 2003). Although MODIS has a designed lifespan of approximately six years, it is anticipated that the instruments will live much longer (Soulakellis et al., 2003). Only a brief description of the MODIS instrument will be given here. For more complete descriptions of MODIS and its products, the reader is referred to Ardanuy et al. (1991), King et al. (1992), Barnes et al. (1998), and Platnick et al. (2003).

MODIS orbits the Earth in a near-polar, sun-synchronous orbit at an altitude of 705 kilometers. Terra is in descending orbit and has an equatorial crossing time of 1030 (local solar time). Aqua is in an ascending orbit, with an equatorial crossing time of 1330 (local solar time). This three-hour lag is advantageous in that it allows "characterization of diurnal patterns" (Platnick et al., 2003). MODIS has an orbit period of ninety-nine minutes and repeats its cycle every sixteen days.

Table 1. MODIS' thrity-six spectral channels. *Edited, original table taken from Barnes et al. (1998).*

Primary Use	Band No.	Bandwidth (nm)	Spectral Radiance	Required SNR
Land/Cloud Boundaries	1**	620-670	21.8	128
	2**	841-876	24.7	201
Land/Cloud Properties	3*	459-479	35.3	243
	4*	545-565	29.0	228
	5*	1230-1250	5.4	74
	6*	1628-1652	7.3	275
	7*	2105-2155	1.0	110
Ocean Color/ Phytoplankton/ Biogeochemistry	8	405-420	44.9	880
	9	438-448	41.9	838
	10	483-493	32.1	802
	11	526-536	27.9	754
	12	546-556	21.0	750
	13	662-672	9.5	910
	14	673-683	8.7	1087
	15	743-753	10.2	586
	16	862-877	6.2	516
Atmospheric Water Vapor	17	890-920	10.0	167
	18	931-941	3.6	57
	19	915-965	15.0	250

Primary Use	Band	Bandwidth (μm)	Spectral Radiance	Required NEDT (K)
Surface/Cloud Temperature	20	3.660-3.840	0.45(300K)	0.05
	21	3.929-3.989	2.38(335K)	2.00
	22	3.929-3.989	0.67(300K)	0.07
	23	4.020-4.080	0.79(300K)	0.07
Atmospheric Temperature	24	4.433-4.498	0.17(250K)	0.25
	25	4.482-4.549	0.59(275K)	0.25
Cirrus Clouds	26	1.360-1.390	6.00	150 (SNR)
Water Vapor	27	6.535-6.895	1.16(240K)	0.25
	28	7.175-7.475	2.18(250K)	0.25
	29	8.400-8.700	9.58(300K)	0.05
Ozone	30	9.580-9.880	3.69(250K)	0.25
Surface/Cloud Temperature	31	10.780-11.280	9.55(300K)	0.05
	32	11.770-12.270	8.94(300K)	0.05
Cloud Top Altitude	33	13.185-13.485	4.52(260K)	0.25
	34	13.485-13.785	3.76(250K)	0.25
	35	13.785-14.085	3.11(240K)	0.25
	36	14.085-14.385	2.08(220K)	0.35

* 500m Spatial Resolution
** 250m Spatial Resolution

Spectral Radiance values are in W/m^2-um-sr
SNR = Signal-to-noise ratio
NEDT = Noise-equivalent temperature difference

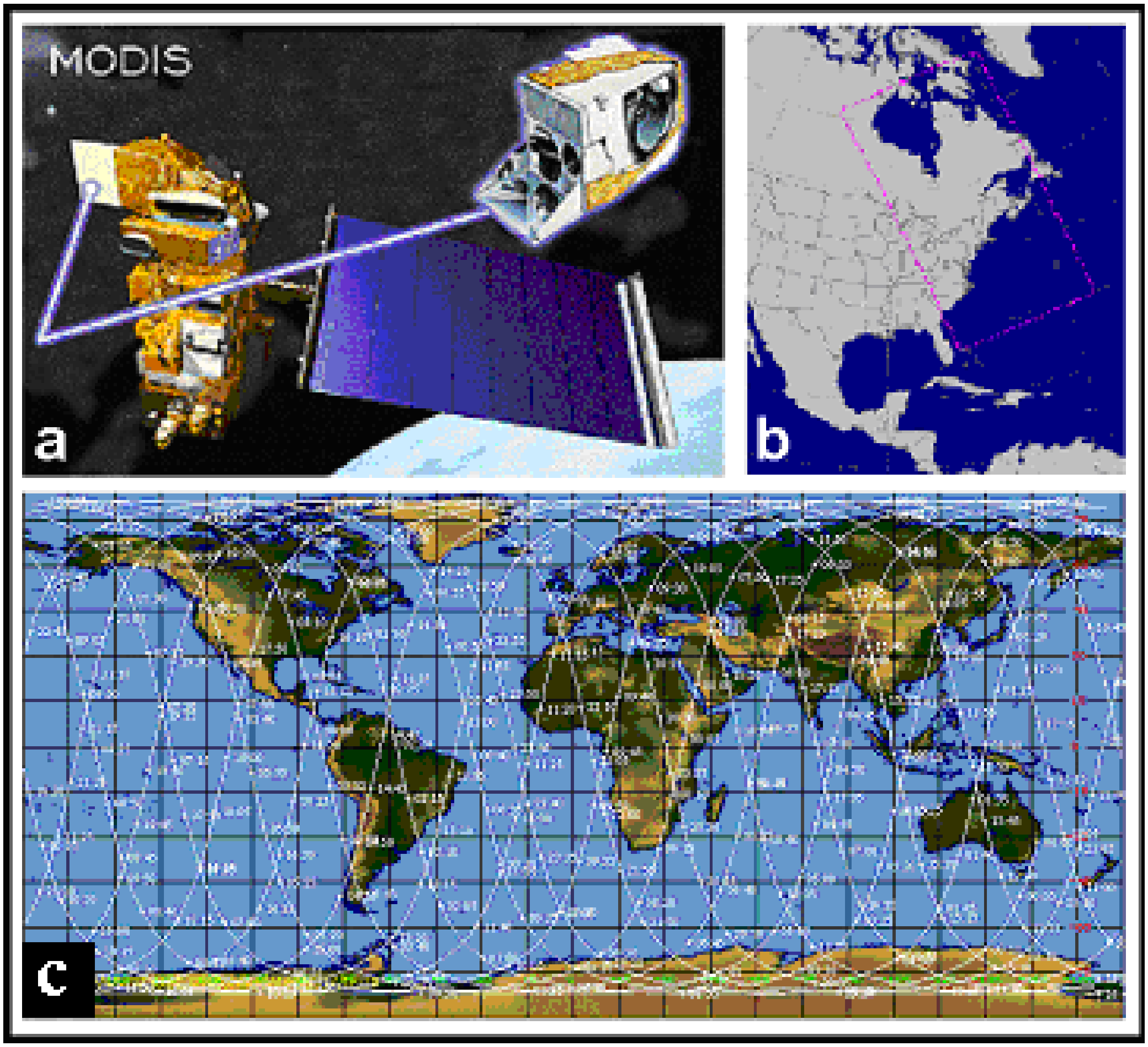

Figure 9. a) the MODIS instrument, *courtesy of NASA*; b) the area cut out by one MODIS granule over the continental United States (CONUS). *Image courtesy of SSEC UW-Madison EOS Direct Broadcast*; c) TERRA/MODIS orbit map and schedule for one 24-hour period (approximate). *Image courtesy of NASA MODIS Rapid Response System & SSEC UW-Madison.*

MODIS is a scanning radiometer that scans in "whiskbroom" fashion with a scan angle of ±55°. Its spectral capabilities consist of thirty-six unique channels, or "bands", whose centerfrequencies range from approximately 0.415 to 14.235μm. Although the MODIS instrument is capable of sub-kilometer spatial resolution at nadir, all but seven bands are at one-kilometer resolution (at nadir). The two 250-meter channels, bands 1-2, are centered at 0.65 and 0.86μm, respectively, with the five 500-meter resolution channels, bands 3-7, centered at 0.47, 0.56, 1.24, 1.63, and 2.13μm, respectively. A listing of all thirty-six MODIS channels is provided in Table 1. MODIS' swath dimensions are 2330 kilometers (cross-track) by 10 kilometers (along-track), yielding ten, twenty, and forty along-track element arrays for the 1000-meter, 500-meter, and 250-meter bands, respectively (Platnick et al., 2003). MODIS has a scan rate of 1.477 scans per second.

Numerous algorithms for cloud property retrievals have been developed for MODIS with their products having relevance to many areas of atmospheric science. Such optical and physical cloud properties include cloud-top pressure, cloud-top temperature, optical thickness, and effective particle radius. MODIS cloud-top pressures are inferred by utilizing the CO_2-slicing methodology (Menzel et al, 1992), which takes advantage of the four MODIS channels (bands 33-36) located within the 15μm CO_2 absorption region as well as the 11μm "atmospheric window" (band 31). The traditional MODIS cloud-top pressure product has a spatial resolution of five kilometers at nadir. A description of the MODIS CO_2-slicing algorithm at 1000-meter resolution is presented in the next section.

V. CO_2-slicing algorithm at 1000-meter resolution

Cloud top pressure may be inferred by application of the radiance-ratioing version of the CO_2-slicing technique (Wielicki and Coakley, 1981; Menzel et al., 1983; Wylie and Menzel, 1989; Baum and Wielicki, 1994; Wylie et al., 1994; McGarragh, 2004). The CO_2-slicing technique uses five infrared bands available on MODIS, with four of these bands located within the 15μm CO_2 absorption region (13.3μm – band 33; 13.6μm – band 34; 13.9μm – band 35, and 14.2μm – band 36). The fifth infrared band is the 11μm window (band 31). The CO_2-slicing methodology takes advantage of the fact that the CO_2 bands become more transmissive with decreasing wavelength (Figure 10), i.e., as the bands move away from the peak of the CO_2 absorption at 15μm. This behavior is encapsulated by the peaks in the weighting functions for these four CO_2 bands (Figure 11), which are derived from the change in transmission t with lnP in an atmospheric column. Three assumptions inherent in this method are: 1) the clouds being observed are infinitesimally thick, 2) the surface emissivity is that of a blackbody for the CO_2 bands, and 3) that the cloud emissivity is identical in the two bands being used (Menzel et al., 1983). We also make the assumption that scattering may be neglected. For clouds above three kilometers above sea level (asl) (approximately 700hPa), cloud top pressures derived from the CO_2-slicing method have accuracies to within approximately ±50hPa (Menzel et al., 1983; Wylie and Menzel, 1989; Platnick et al., 2003, Bedka et al., 2005) for many cases. The following description of the radiance-ratioing version of the CO_2-slicing technique closely follows Baum and Wielicki (1994) and McGarragh (2004).

For a black surface (i.e. surface emissivity $\varepsilon_s = 1$), the clear-sky spectral radiance I_{CLR} may be given by

$$I_{CLR}(\nu^i, P_s) = B(\nu^i, T_s)t(\nu^i, P_s) + \int_{P_s}^{0} B\left[\nu^i, T(P)\right]\frac{dt(\nu^i, P)}{d\ln P}\, d\ln P \qquad \{4\}$$

where $B(\nu^i, T_s)$ is the Planck radiance at temperature T (with subscript "*s*" denoting the surface), ν^i is the wavenumber of band number i, and $t(\nu^i, P)$ is the transmittance from atmospheric level P to the space-borne instrument at $P = 0$.

For a black cloud (i.e. cloud emissivity $\varepsilon_c = 1$) at pressure level P_c, the radiance I_{BLK} may be given by

$$I_{BLK}(\nu^i, P_c) = B(\nu^i, T_c)t(\nu^i, P_c) + \int_{P_c}^{0} B\left[\nu^i, T(P)\right]\frac{dt(\nu^i, P)}{d\ln P}\, d\ln P \qquad \{5\}$$

where the subscript "*c*" denotes the cloud.

For a single cloud layer in a single field of view (FOV), the top-of-the-atmosphere (TOA) radiance I is given as

$$I = (1 - N)\, I_{CLR} + N I_{CLD} \qquad \{6\}$$

where N is the cloud fraction (the percentage of the FOV that contains cloud). I_{CLD} is expressed as

$$I_{CLD} = (1-\varepsilon_c)\, I_{CLR} + \varepsilon_c\, I_{BLK} \qquad \{7\}$$

Substitution of Equation {7} into Equation {6} yields

$$I = (1 - N\,\varepsilon_c)\, I_{CLR} + N\,\varepsilon_c\, I_{BLK} \qquad \{8\}$$

Equation {8} is an expression for the radiance from a partially cloudy FOV, and may be rearranged to produce the "cloud signal" (I - I_{CLR}).

$$I - I_{CLR} = N\,\varepsilon_c\,(I_{BLK} - I_{CLR}) \qquad \{9\}$$

We now substitute Equations {4} and {5} into Equation {9}, which, after further simplification, yields

$$I(\nu^i) - I_{CLR}(\nu^i) = N\,\varepsilon_c \int_{P_s}^{P_c} t(\nu^i, P)\, dB\left[\nu^i, T(P)\right] \qquad \{10\}$$

We now create a ratio of cloud signals for two different bands, dubbed the "G-function", where we introduce the superscript "*j*" as a second band number.

$$G^{ij}(P_c) = \frac{I(\nu^i) - I_{CLR}(\nu^i)}{I(\nu^j) - I_{CLR}(\nu^j)} = \frac{\int_{P_s}^{P_c} t(\nu^i, P)\, dB\left[\nu^i, T(P)\right]}{\int_{P_s}^{P_c} t(\nu^j, P)\, dB\left[\nu^j, T(P)\right]} \qquad \{11\}$$

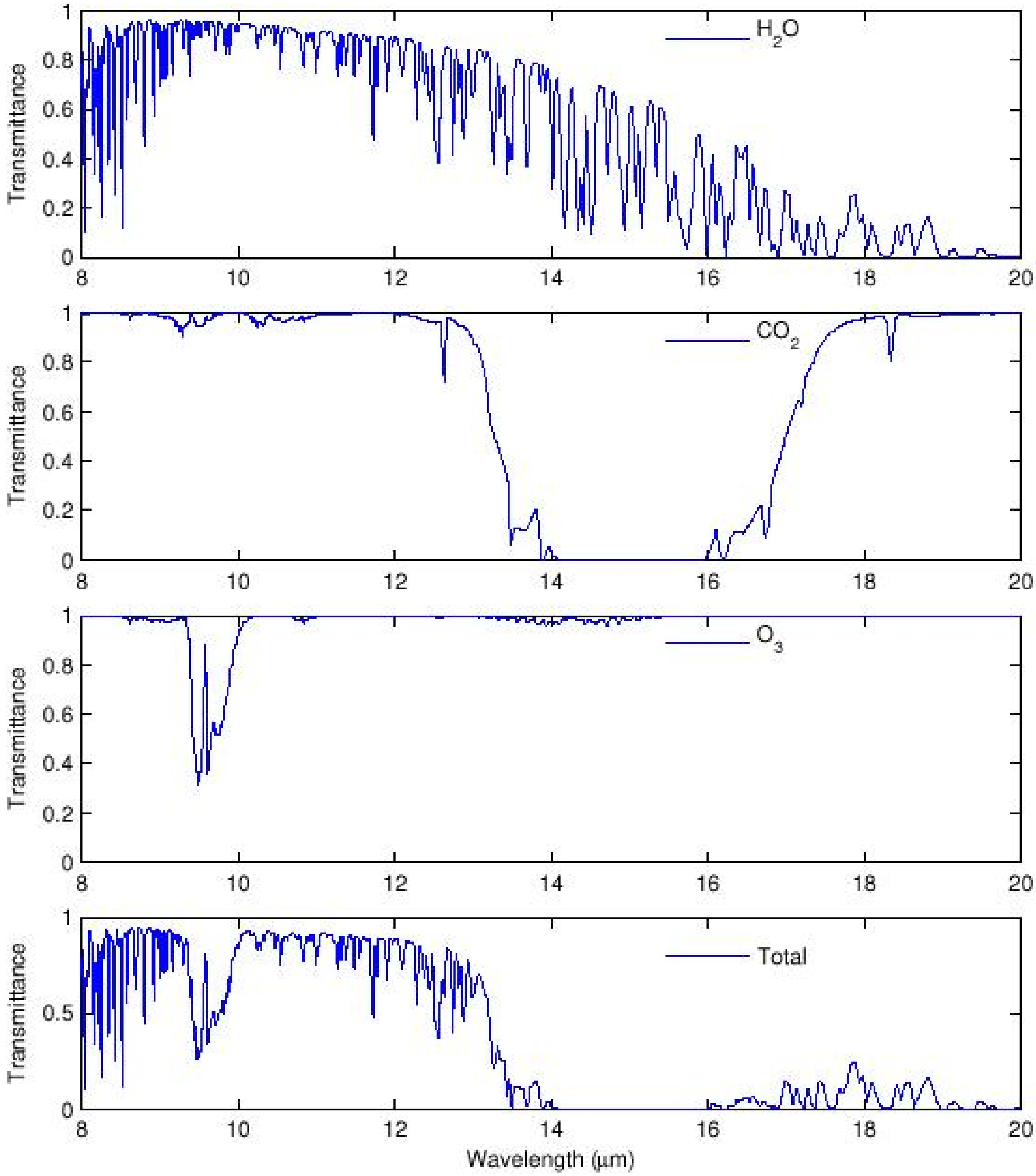

Figure 10. Transmittance from the top of the atmosphere to the surface for H_2O, CO_2, and O_3, and for all three constituents combined. Calculated with LBLRTM 7.04 using the U.S. standard 1976 atmosphere. *Image and caption taken from McGarragh (2004).*

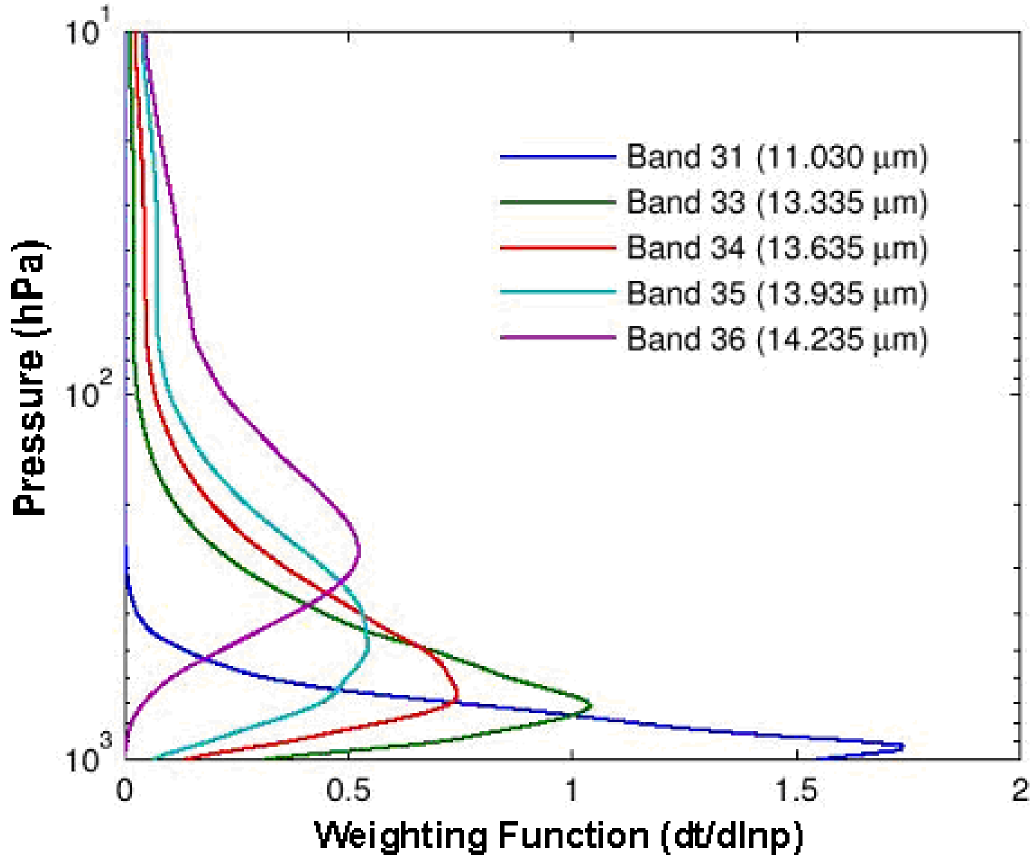

Figure 11. Weighting functions (dt/dl*np*) for five MODIS CO_2 infrared bands as functions of pressure (mb). Calculated with the GDAS atmosphere for March 20, 2003 at 1200Z located on the equator at -30^o longitude using a sensor view angle of 0^o. *Image and edited caption taken from McGarragh (2004).*

We arrive at Equation {11} by making the assumption that both emissivities are equal for the two closely spaced bands *i* and *j* (i.e. $\varepsilon_c^i = \varepsilon_c^j$). This assumption is the focus of research presented later in this study.

The cloud signal ratio on the left side of Equation {11} is determined from radiances measured by MODIS and the NOAA NCEP Global Data Assimilation System (GDAS) gridded meteorological product, with the cloud signal ratio on the right side of {8} calculated from a forward radiative transfer model (Menzel et al., 1983). The GDAS product provides the temperature and water vapor mixing ratio data that is required to obtain the atmospheric transmittance profiles. The temperature and water vapor mixing ratio data is provided at 16 separate pressure levels, however this data is extrapolated to 101 pressure levels, which is required to calculate the transmittance profile. Also required to calculate the transmittance profile is a 101-pressure level atmospheric ozone profile. This ozone profile is extrapolated from LBLRTM model atmospheres. For a more complete description of the creation and caching procedures of the transmittance profile, the reader is referred to the work of McGarragh (2004). All CO_2-slicing height retrievals presented in this study have been derived from the GDAS profiles. It should be noted that true local atmospheric profiles might differ significantly from the GDAS profiles used. Additional research must to be conducted to determine how great an effect these potential discrepancies might have on the CO_2-slicing height product.

The G-function ratios are set up using pre-determined combinations of the four MODIS CO_2 bands, as outlined in Platnick et al. (2003), with the addition of an additional band combination (McGarragh, 2004). To summarize, the five band ratios used for this CO_2-slicing algorithm are band36/band35 (14.235μm/13.935μm), band36/band34 (14.235μm/13.635μm), band35/band34 (13.935μm/13.635μm), band35/band33 (13.935μm/13.335μm), and band34/band33 (13.635μm/13.335μm). For each band combination, the cloud pressure P_c that best minimizes the difference between the observed and calculated cloud signal (Equation {11}) is considered the most representative for that pair. For the bands combinations outlined above, we will now be left with five representative values for P_c. For each value of P_c, an "effective cloud amount" $N\varepsilon_c$ may be calculated by rearranging Equation {9}.

$$N\varepsilon_c = \frac{I(w) - I_{CLR}(w)}{I_{BLK}(w) - I_{CLR}(w)} \qquad \{12\}$$

where the w function dependence translates to radiances retrieved through the atmospheric window channel (~11µm). Due to MODIS' 1000-meter resolution in the infrared region, the effective cloud amount will be interpreted as cloud emissivity (McGarragh, 2004). Following the work of Menzel et al. (1983), a final cloud-top pressure is chosen from the five representative P_c values by error analysis.

$$M_{ik} = \left(I - I_{CLR}\right)_i - N\varepsilon_{ck} \int_{P_s}^{P_{ck}} t(\nu^i, P_{ck})\, dB\left[\nu^i, T(P_{ck})\right] \qquad \{13\}$$

$$\sum_{i=1}^{4} M_{ik}^2 \qquad \{14\}$$

We use Equation {13} to check the difference between the cloud signal values and those calculated from the radiative transfer equation. The subscripts "i" and "k" refer to the band number (four in total) and representative P_c solution (five in total), respectively. The final cloud-top pressure P_{ck} is obtained when Equation {14} is a minimum. This final cloud top pressure is converted to a height asl using the meteorological profiles in the GDAS product.

There are two situations that produce unacceptable retrievals (hereafter referred to as "invalid" results) via the CO_2-slicing method. The first considers the noise equivalent delta radiance (NEDR) for the wavelength in question. A solution is considered invalid if either cloud signal on the right-hand-side of Equation {11} falls within the NEDR for their wavelength. The second refers to an issue regarding the interpolation of pressure levels, and the reader is referred to McGarragh (2004) for a description of this limitation. In either case, invalid CO_2-slicing results are supplemented with heights obtained by using the BT-method discussed in section III of this paper. This method is accomplished by interpolating the 11μm BTs into the atmospherically corrected BT profile, with the effective emissivity set to unity. Height estimates at altitudes beneath the 700hPa pressure level are automatically obtained using the BT-method, although, if desired, CO_2-slicing results may be forced at these altitudes. The forcing of the CO_2-slicing method at altitudes lower than 700hPa does not circumvent the NEDR limitation, however, as the BT-method will still be used for height retrievals should the cloud-signal fall within the NEDR for their wavelength. Except where noted, the results presented in this paper utilize the BT-method for altitudes beneath 700hPa.

There are several situations that are known to cause height retrieval errors with the CO_2-slicing methodology. The first, and perhaps the most significant when considering volcanic eruptions, is the presence of temperature inversions in the atmosphere. The P_c solutions are determined by the G-function (Equation {11}), which is a strongly dependant on the atmospheric temperature profile. When a temperature inversion is present, the G-function (Figure 12) inverts as well, creating two possible solutions (one above and one below the inversion point). G-function retrieval problems also occur in isothermal regions of the atmosphere. Surface temperature inversions and isothermal regions of the atmosphere are more commonly present in polar atmospheres; therefore we limit our investigations in this study to scenes located in tropical and mid-latitude atmospheres. One source of G-function error that may be unavoidable, however, is the tropopause, where a temperature inversion is always present. As will be shown in a later section, volcanic eruptions can pierce the tropopause. The CO_2-slicing algorithm begins by searching for the tropopause (the point where the temperature begins to increase with decreasing height, moving downward from the stratosphere). Should the tropopause be located at an altitude higher than the 100hPa pressure level, the algorithm will assign the "tropopause" to be at 100hPa. In either case, the "tropopause" assigns the maximum allowable G-function value (calculated). Should a cloud lie in the isothermal layer, the observed G-function value might be greater than the maximum G-function value allowed, in which case the pressure solution P_c is assigned according to the maximum allowable G-function value. If a cloud lies near the tropopause, where the observed G-function value corresponds to two different calculated G-function values (one above and one below the physical tropopause), the higher pressure (lower height) is retained. This assumption can lead to errors should a cloud pierce the tropopause, as the stratospheric portions of the cloud would be assigned a height too low. If it is known that stratospheric penetration has occurred, the algorithm may be forced to raise the "tropopause" well into the stratosphere, and well above any physical cloud element that may be present. Should this be done, stratospheric clouds would be assigned pressure values that correspond to the higher of the two acceptable calculated G-function values (both now below the "tropopause"). Tropospheric clouds near the physical tropopause, however, would be assigned heights too high.

CO_2-slicing can retrieve heights of stratospheric clouds if the clouds are known independently to be located well above the isothermal layer. To retrieve these heights, a separate version of the CO_2-slicing algorithm that uses different interpolation logic must be implemented. To retrieve the heights for a cloudy scene that contains both tropospheric and stratospheric clouds, both the tropospheric and stratospheric versions of the CO_2-slicing algorithm must be run. Because the CO_2-slicing methodology cannot distinguish between these cloud types, the stratospheric version of the CO_2-slicing algorithm may only be applied to the cloudy regions otherwise known to contain stratospheric cloud elements. Unless otherwise noted, all heights retrievals presented in this study were processed using the tropospheric version of the CO_2-slicing algorithm.

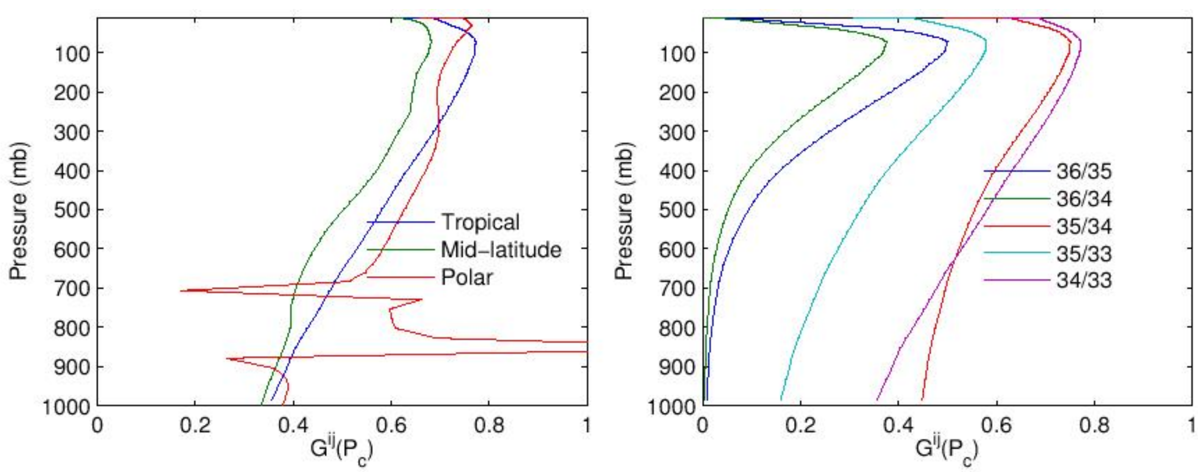

Figure 12. Cloud pressure function $G^{ij}(P_c)$ for (left) band ratio 34/33 calculated using tropical, mid-latitude, and polar profiles and for (right) band ratios 36/35, 36/34, 35/34, 35/33, and 34/33 calculated using a tropical profile. Calculated with the GDAS atmosphere for March 20, 2003 at 1200 using a sensor view angle of 0^o. All atmospheres are located at –30^o longitude with the tropical, mid-latitude, and polar atmospheres at 0^o, 45^o, and 90^o latitude respectively. *Image and caption taken from McGarragh (2004).*

Menzel et al. (1992) and McGarragh (2004) also detail other potentially significant sources of error that can arise from the assumptions made by the CO_2-slicing algorithm. Two such assumptions consider the surface properties that factor into the calculation of the clear-sky spectral radiance, where the surface skin temperature is assumed to be the same as the atmospheric temperature immediately above the surface, and surface emissivity is assumed to be unity. Both assumptions can lead to error as warm and cold air advection and boundary layer inversions can create drastic differences between the skin and surface air temperatures, and surface emissivity is not always unity. These errors may be considered negligible (McGarragh, 2004), however, if the MODIS CO_2 band weighting functions (Figure 11) peak above the surface.

Another assumption made by the CO_2-slicing algorithm is that the clouds are infinitesimally thick. This will lead to errors when observing optically thin clouds, as radiation originating from within and below the cloud will be detected by the space-borne sensor (Menzel et al., 1983). This, in-turn, leads the space-borne sensor to effectively "see" the thin clouds at lower altitudes and underestimate the heights. As the clouds increase in optical thickness, the "radiative center" of the clouds will increase in altitude, leading to more accurate height assignments for the most optically thick clouds. There is, however, an overall low height bias in CO_2-slicing cloud height retrievals due to this assumption. For more detailed descriptions of this limitation, the reader is referred to Smith and Platt (1978), Wielicki and Coakley (1981), Menzel et al. (1983), and Menzel et al. (1992). Errors can also occurs can also occur in the presence of multiple cloud layers. For complete descriptions of this limitation and its error analysis, the reader is referred to Menzel et al. (1992), Baum and Wielicki (1994), Frey et al. (1999), and McGarragh (2004).

The CO_2-slicing height products presented in this paper do not consist entirely of fields of view whose heights have been retrieved specifically by the CO_2-slicing algorithm. Rather, this paper presents the standard operational CO_2-slicing product at 1000-meter resolution. The standard product yields heights that are retrieved specifically by the CO_2-slicing algorithm, as well as the 11μm BT-method when the aforementioned limitations hinder the application of the CO_2-slicing algorithm. Although these results are presented as the "CO_2-slicing height product," the reader should know that, except where noted, they may include significant coverage by the 11μm BT-method.

VI. The Multi-angle Imaging SpectroRadiometer (MISR)

The Multi-angle Imaging SpectroRadiometer (MISR) was one of five instruments launched December 18, 1999 aboard NASA's Terra spacecraft. Built by the Jet Propulsion Laboratory, MISR utilizes nine separate cameras that observe the earth in "pushbroom" fashion in four spectral bands from Terra's near-polar, sun-synchronous orbit. These nine cameras "acquire moderately high-resolution imagery over a wide angular range in the along-track direction" (Diner et al., 2002), with each camera viewing the earth at unique angles to the local vertical (Figure 13). This unique nine-camera configuration allows MISR to retrieve such cloud parameters as cloud-top heights using a "purely geometrical technique" (Moroney, et al., 2002a). Provided here is a brief overview of the instrument and a description of the cloud-top height retrieval methodology. A more complete description of the MISR instrument may be found in Diner et al. (1998).

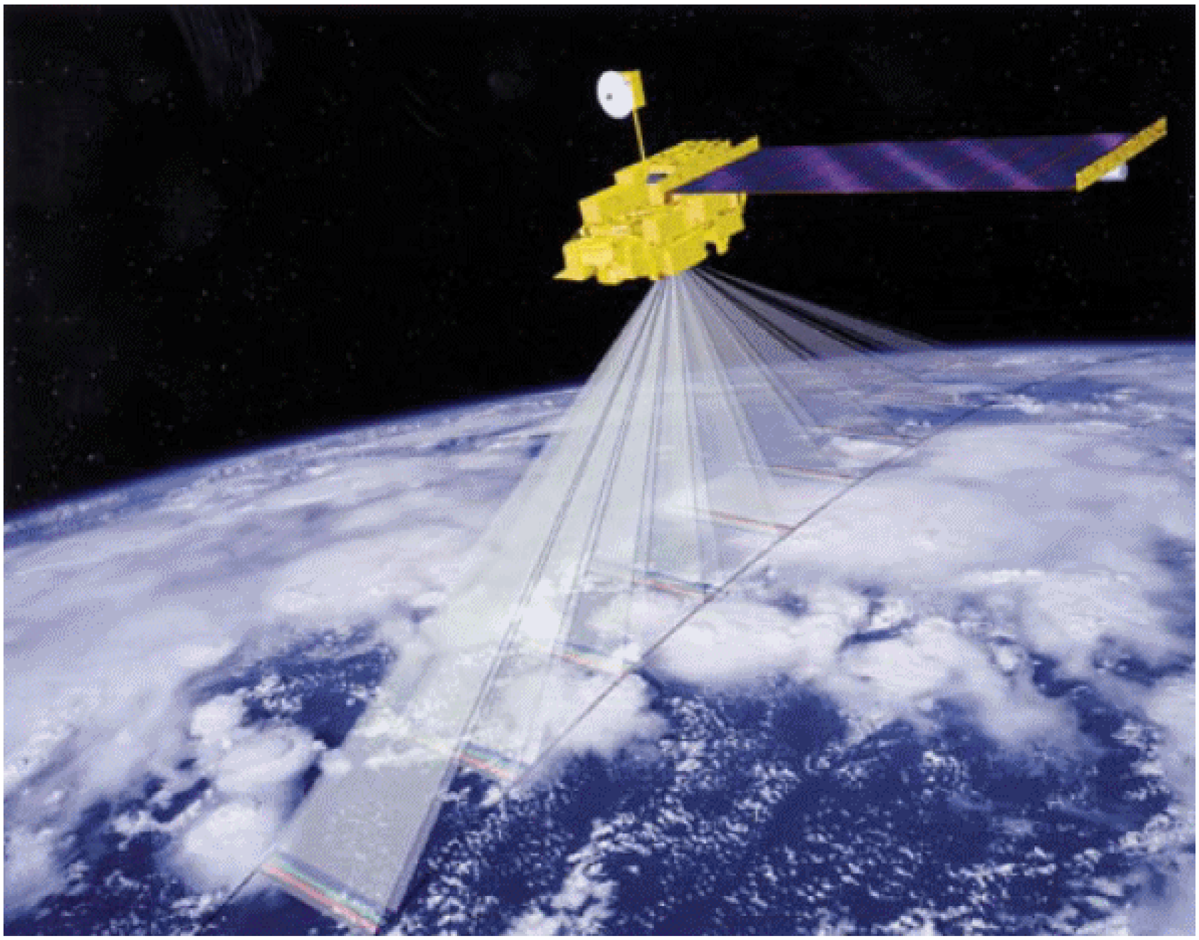

Figure 13. This graphic illustrates the measurement approach of the MISR instrument. Nine pushbroom cameras point at discrete angles along the spacecraft ground track, and data in four spectral bands are obtained for each camera. *Image and caption taken from Diner et al. (2002).*

The MISR instrument's nine cameras (Table 2) are situated to provide a relatively large angular range for along-track viewing. One camera is positioned at 0^{o} (nadir, designated as camera *An*), four cameras are pointed in the forward (along-track) direction, with the remaining four cameras pointed in the aft direction. The four forward viewing cameras are positioned at 26.1^o (camera *Af*), 45.6^o (camera *Bf*), 60.0^o (camera *Cf*), and 70.5^o (camera *Df*) from nadir, with the aft viewing *Aa, Ba*, *Ca*, and *Da* cameras also positioned at 26.1^o, 45.6^o, 60.0^o, and 70.5^o from nadir, respectively. From Terra's 705-kilometer orbit, MISR has an in-nadir swath width of 376 kilometers and an off-nadir swath width of 413 kilometers, and the time interval between a distinct point on the earth being viewed by the *Df* camera and the *Da* cameras (the time it takes a point on the earth to be viewed by all nine MISR cameras) is seven minutes (Diner et al., 2002). To account for the earth's rotation during these seven minutes, each camera's cross-track angle is slightly offset (Diner et al., 1998), maximizing the overlap by all cameras. The MISR instrument has a maximum resolution of 250 meters at nadir, with a maximum off-nadir resolution of 275 meters. MISR views the entire Earth's surface in a period of nine days.

Table 2. MISR camera pointing requirements and as-built specifications. *Table and caption taken from Diner et al. (1998).*

	View angle		Boresight angle		Swath offset angle		Effective focal length (mm)	
Camera	Specification	As-Built	Specification	As-Built	Specification	As-Built	Specification	As-Built
Df	70.5° (forward)	70.3°	58.0 ± 0.2°	57.88°	-2.7 ± 0.2°	-2.62°	123.8 ± 1.9	123.67
Cf	60.0° (forward)	60.2°	51.2 ± 0.2°	51.30°	-2.3 ± 0.2°	-2.22°	95.3 ± 1.4	95.34
Bf	45.6° (forward)	45.7°	40.0 ± 0.2°	40.10°	-1.7 ± 0.2°	-1.71°	73.4 ± 1.1	73.03
Af	26.1° (forward)	26.2°	23.3 ± 0.2°	23.34°	-1.0 ± 0.2°	-1.06°	59.3 ± 0.9	58.90
An	0.0° (nadir)	0.1°	0.0 ± 0.2°	-0.04°	0.0 ± 0.2°	0.04°	59.3 ± 0.9	58.94
Aa	26.1 (aftward)	26.2°	-23.3 ± 0.2°	-23.35°	1.0 ± 0.2°	1.09°	59.3 ± 0.9	59.03
Ba	45.6° (aftward)	45.7°	-40.0 ± 0.2°	-40.06°	1.7 ± 0.2°	1.76°	73.4 ± 0.9	73.00
Ca	60.0° (aftward)	60.2°	-51.2 ± 0.2°	-51.31°	2.3 ± 0.2°	2.24°	95.3 ± 1.4	95.33
Da	70.5° (aftward)	70.6°	-58.0 ± 0.2°	-58.03°	2.7 ± 0.2°	2.69°	123.8 ± 1.9	123.66

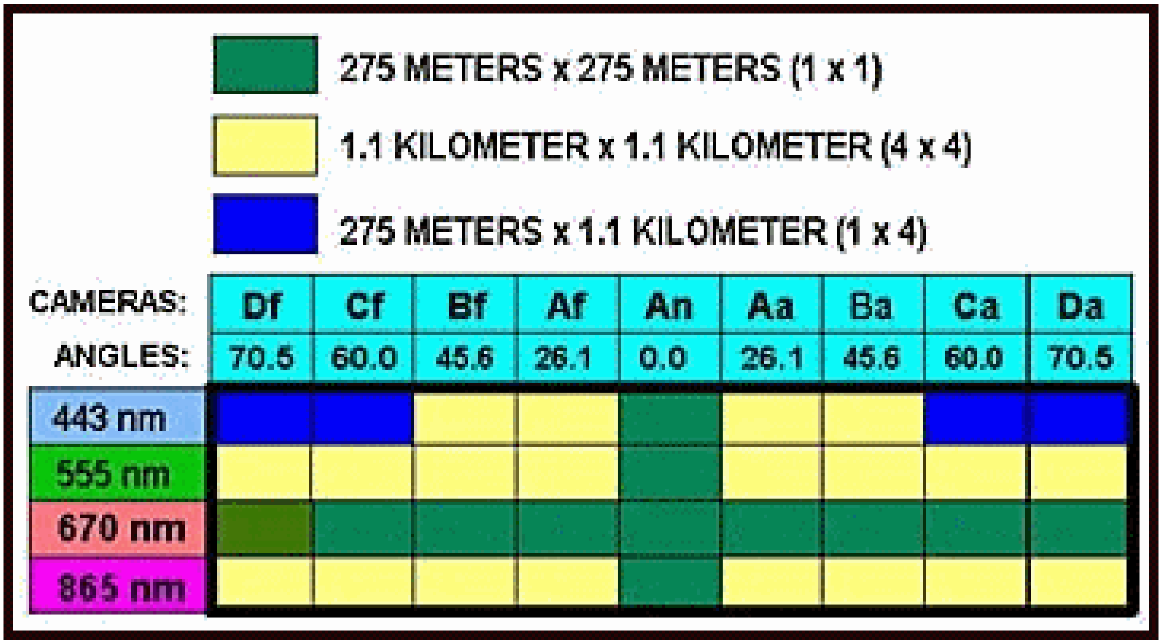

Figure 14. Typical MISR camera configuration. *Image courtesy of NASA (http://www-misr.jpl.nasa.gov/mission/mibigres.html)*

Each of the nine MISR cameras consists of their own individual lens and is sensitive to four unique spectral bands (Figure 14). The center wavelengths for these four bands are 446.3 (blue), 557.5 (green), 671.8 (red), and 866.5 (near-infrared) nanometers, and have widths of 40.9, 27.2, 20.4, and 38.6 nanometers, respectively (Bruegge, 1998). The wavelengths were chosen for the MISR mission to avoid known regions of strong atmospheric gas absorption and solar Fraunhofer lines. These wavelengths were also chosen for their applicability to specific areas of research. The red and near-infrared wavelengths have applications to marine aerosol studies (Kahn et al., 2001), while the green wavelength is very useful in albedo studies (Jin et al, 2002).

VII. MISR height retrieval

The MISR cloud-top height product is produced using a stereophotogrammetric technique, which, unlike the CO_2-slicing methodology, does not require assuming any particular state of the Earth's atmosphere. The cloud-top height retrieval consists of two main steps, both of which require the use of stereo-matching algorithms, which are described in detail in Diner et al. (1999), Moroney et al. (2002a) and Muller et al. (2002). The first step involves retrieving cloud-motion vectors (hereafter referred to as "wind") and cloud-top height values at relatively low resolution, with the second step being the cloud-top height retrieval at a higher resolution. The "current operational processing" methodology will be briefly described and details may be found in Moroney et al. (2002a). Analyses from early on in MISR's operational life suggest cloud-top heights to be accurate to within ±562 meters at 1.1-kilometer resolution (Moroney et al., 2002a).

In truth, cloud-top heights may be retrieved without utilizing the aforementioned first step. However, any cloud motion due to advection during the seven minute time interval required for all nine MISR cameras to view a specific scene may lead to significant errors. The wind correction process utilizes three cameras and pairs them as *Bf-Df* and *Bf-An* (Figure 15). The use of three cameras allows for solutions from the stereo-matching algorithm to be achieved for both wind and cloud-top height simultaneously. These retrievals are made at a coarse 70.4-kilometer resolution. The winds are then decomposed into their north-south and east-west components and are binned in a two-dimensional histogram. For each 70.4-kilometer domain, the modal value of the histogram is considered its representative wind field.

Additionally, all winds must pass a quality test. Error analysis suggests wind speed errors of ±3 m/s, corresponding to heights errors (from these winds) of ±400 meters (Moroney et al., 2002a).

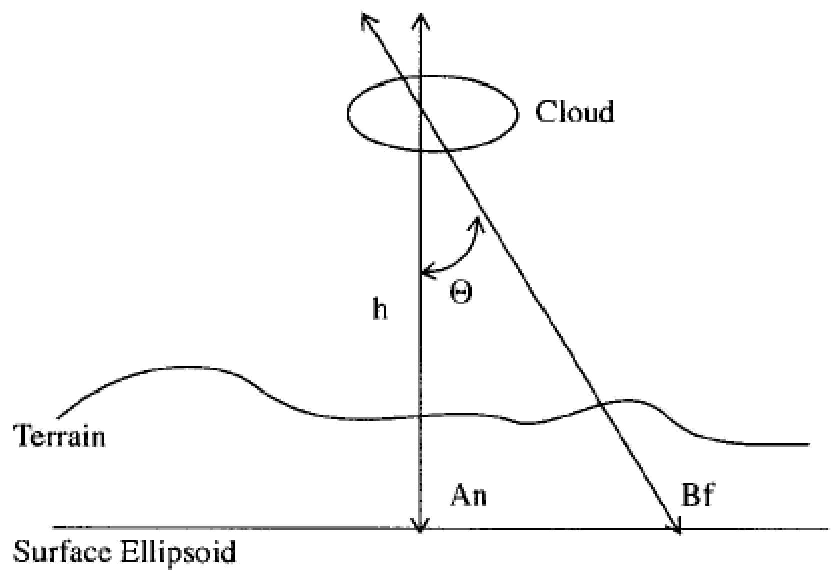

Figure 15. MISR viewing geometry for the *An* and *Bf* cameras. *Image and caption taken from Moroney et al. (2002b).*

The second step in the MISR cloud-top height retrieval method first consists of dividing the 70.4-kilometer domain into smaller, 1.1-kilometer sub-region. Considering the previously calculated wind correction values (identical for each 1.1-km sub-region within a 70.4-km domain), the stereo-matching algorithm is run twice in each sub-region to obtain cloud-top height values, once for the *Af-An* camera pair and once for the *Aa-An* camera pair. While the data ingested by the stereo-matching algorithm is at 275-kilometer resolution, time restrictions require cloud-top height values to be retrieved for every fourth pixel (1.1-kilometer resolution). In each sub-region, the stereo-matching algorithm may not find a valid match within the allowable search window. If only one camera pair retrieves a valid match, the height is accepted. If both camera pairs return valid matches and both resultant heights agree within a certain threshold, the higher of the two heights is retained. This threshold is described in detail in Diner et al. (1999), but may be summarized by

$$\Delta h \geq [\mathrm{mean}\Delta h] - N_{\sigma} \bullet \sigma_{\Delta h} \qquad \{15\}$$

$$\Delta h \geq [\mathrm{mean}\Delta h] + N_{\sigma} \bullet \sigma_{\Delta h} \qquad \{16\}$$

where Δh is the difference between the two heights, $[\mathrm{mean}\Delta h]$ is the mean of the height differences for all points in the domain containing the pixel in question, $\sigma_{\Delta h}$ is the standard deviation for this distribution, and N_{σ} is a configurable parameter (Diner et al., 1999). If both Equation {15} and {16} prove true, both heights are considered to agree within the threshold. If the two heights do not agree, both are rejected. One limitation to the height algorithm occurs in the presence of multi-layered clouds. Multi-layered cloudy scenes have been known to cause confusion for the stereo-matching algorithms and are known problem areas for MISR's cloud-top height retrieval method. A recent investigation published in Naud et al. (2004) concludes "Optically thin clouds were found to be accurately characterized by the MISR cloud-top height product as long as no other cloud was present at a lower altitude." A more detailed description of the limitations to MISR's cloud-top height retrieval methodology may be found in Moroney et al. (2002a).

The final cloud-top height product can be viewed in several ways. The two main ways the height products are the “Best Winds” and “Without Winds”. Without Winds simply means that there was no wind correction applied in the two-step height retrieval process. This view does not yield the “true” height field (unless the real wind speed was uniformly zero), but rather gives an “overview” of the heights in the scene. Best Winds yield the “best guess” as to the true height field. Because wind retrievals of good quality only occur 55-60% of the time (Catherine Moroney, personal communication 2005), Best Wind views might not yield the entire height field.

There have been studies published in which MISR’s height product is compared with both the operational MODIS CO_2-slicing algorithm (Moroney et al., 2002a) and lidar data (Naud et al., 2004). In the MISR comparison, a TERRA overpass was collocated in time and space with reflectivities retrieved from a 94-GHz ground-based radar. This study found heights to be in MODIS heights to be in agreement with the radar to ±1.5 kilometers, while MISR heights were in agreement to ±500 meters. In the lidar comparison, one year of back-scattering lidar cloud boundaries and optical depth were compared with MISR. MISR was found to differ with the lidar from –0.1 and 0.4 kilometers for low clouds and from 0.1 and 3.1 kilometers for high clouds.

VIII. CO_2-slicing heights compared with MISR heights

For the MODIS/MISR comparisons presented in this section, we utilize two different versions of the MISR height product. The first version of the MISR height algorithm is a product of the production code publicly available at the time of this investigation, and we hereafter refer to this MISR algorithm version as version *alpha*. The second version of the MISR height algorithm is a product of a prototype height algorithm (hereafter referred to as version *beta*) that has been specially run for this investigation by Catherine Moroney of the MISR science team. The *beta* height algorithm contains two main improvements to version *alpha*. The first improvement is a more accurate wind calculation algorithm. The second improvement is better wind quality control measures, as the winds in the *beta* version are calculated separately for the forward- and aft- viewing cameras, which are then compared. Because of these improved wind quality flags, coverage in the "best winds" version of the *beta* MISR height algorithm might be significantly decreased. The new wind calculations are now believed to be more accurate (Catherine Moroney – personal communication 2005), which will improve the "best winds" height retrievals. The *beta* version of the MISR height algorithm is, as yet, not public, however it is slated to become operational by late 2005.

To facilitate pixel-to-pixel comparisons for MODIS' 1.0-kilometer resolution and MISR's 1.1-kilometer resolution height products, a special collocation algorithm was required. The MODIS/MISR collocation algorithm used in this investigation was written by and is provided courtesy of Michael Garay of the Jet Propulsion Laboratory in Pasadena, California, USA. This algorithm regrids the MODIS and MISR data to a third grid of lower resolution, allowing 100 percent coverage of both instruments' height products.

In this section, we compare CO_2-slicing height retrievals with MISR's stereo heights for four volcanic plumes (Table 3). All MISR data presented in this section is of format number 7 and software version 11 or higher. The statistics for these comparisons (Table 4) were generated after collocation of the MODIS and MISR data. Following the collocation, a section of each volcanic plume known to have coverage with MISR's *alpha* version best winds height product was isolated. These sections were isolated by bounding them in a latitude/longitude box; the boxes' corner points are printed in Table 3. The corner points were determined so as to also eliminate contamination by meteorological cloud and erroneous height retrievals from the earth's surface. Trimmed-means (middle 80%) were calculated from the bounded, collocated pixels.

The following analysis concerns only the best wind heights retrieved by MISR by both the *alpha* and *beta* versions. The without winds height product is presented as a reference to the coverage that MISR did have for each individual plume, however, its height product should not be considered representative of the plumes' heights without knowledge of the true local wind field. In addition, the CO_2-slicing height product utilizes the 11µm BT-method to estimate heights for fields of view where the CO_2-slicing algorithm fails. Should noise levels become too high, the 11µm method may, at times, be applied to the entire MODIS granule.

Anatahan

24 May 2003

The Anatahan Volcano is located in the Pacific Ocean 320 kilometers north of Guam and approximately 120 kilometers north of Saipan Island. Its first historical eruption was on 10 May 2003 (US Geological Survey – 2005). Volcanic activity continued during the following weeks, and TERRA's instruments captured one of Anatahan's volcanic plumes on 24 May 2004 (Figure 16). For the area of the volcanic plume selected for analysis (Table 3), both MODIS (panel "b") and MISR's *alpha* algorithm (panels "d") agree that the height of this plume was 2000 meters ± 300 meters. MISR's *beta* algorithm, however, suggests that the heights might have been higher. The *beta* best winds product presents a trimmed-mean value close to 5000 meters, with a standard deviation (sd) of zero meters. Graphical inspection of the entire plume for this product (panel "f"), however, shows that the *beta* best wind product did, in fact, yield heights that were less than 3000 meters for parts of the plume. The discontinuity in the height field is representative of discontinuities in the MISR retrieved wind field. For the plume's selected region, however, MISR's *beta* best winds suggests much higher heights than both the MODIS and MISR *alpha* algorithm products, although the drastic discontinuity in the wind field causes some lack of confidence in this bounded region's height retrieval.

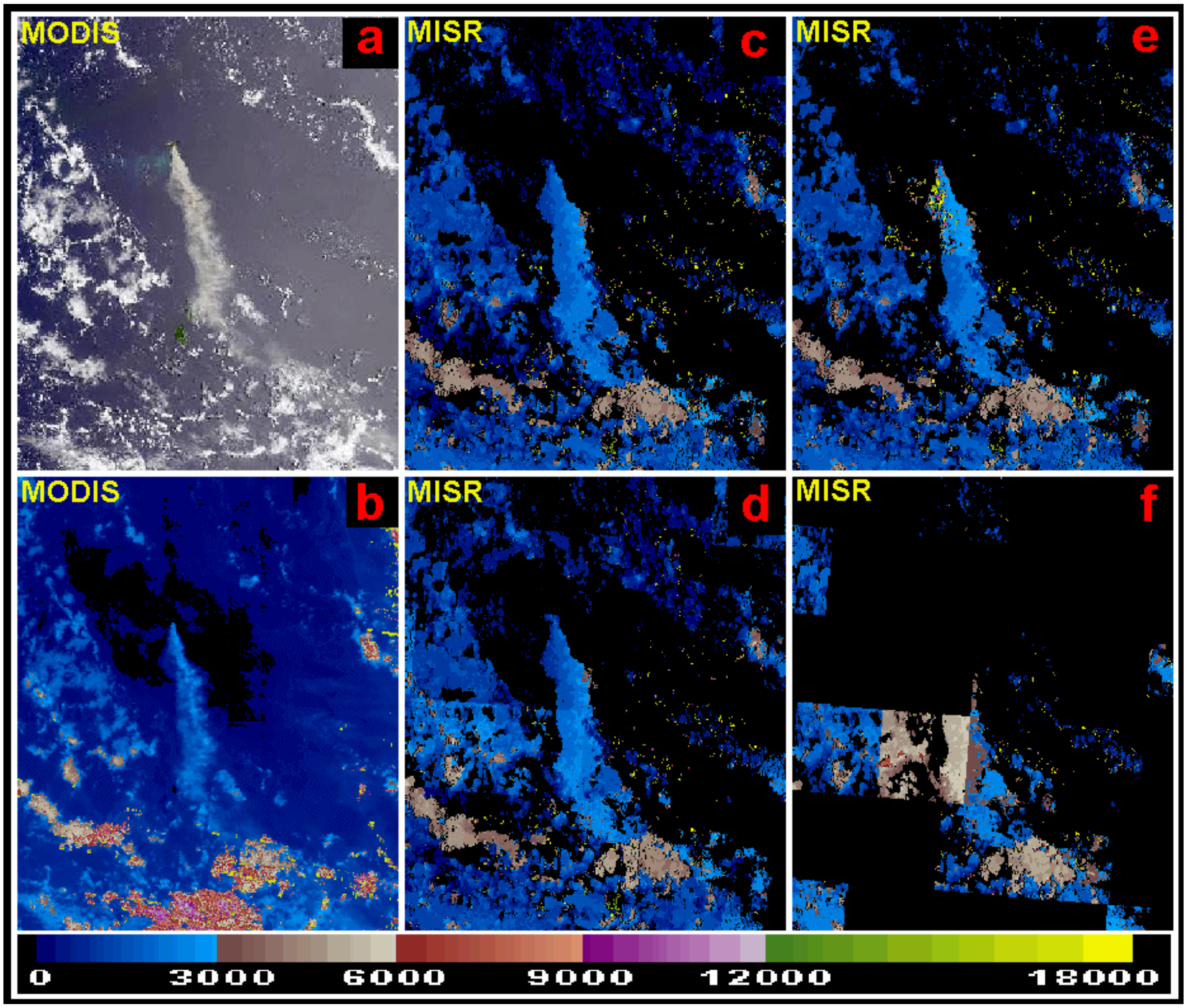

Figure 16. Eruption of the Anatahan Volcano, 24 May 2003, 0055Z, observed by TERRA. a) MODIS true color image; b) MODIS CO_2-slicing height product; c) MISR *alpha* version "without winds" height product; d) MISR *alpha* version "best winds" height product; e) MISR *beta* version "without winds" height product; f) MISR *beta* version "best winds" height product.

Chikurachki

22 April 2003

The Chikurachki Volcano is located on Paramushir Island in the northern Kurile Islands, Russia. MODIS and MISR captured an ash plume from Chikurachki on 22 April 2003

(Figure 17). MISR's *alpha* height product retrieved a trimmed-mean height of 2038 meters and the MODIS CO_2-slicing algorithm retrieved a trimmed mean height of 878 meters, with standard deviations of 604 meters and 475 meters, respectively. MISR's *beta* algorithm again yielded higher heights with a trimmed-mean height of 3210 meters (252 sd). There were, however, only 12 pixels considered for the MISR *beta* best wind algorithm. Panel "f" shows the drastic lack of coverage for this plume in the MISR *beta* height product.

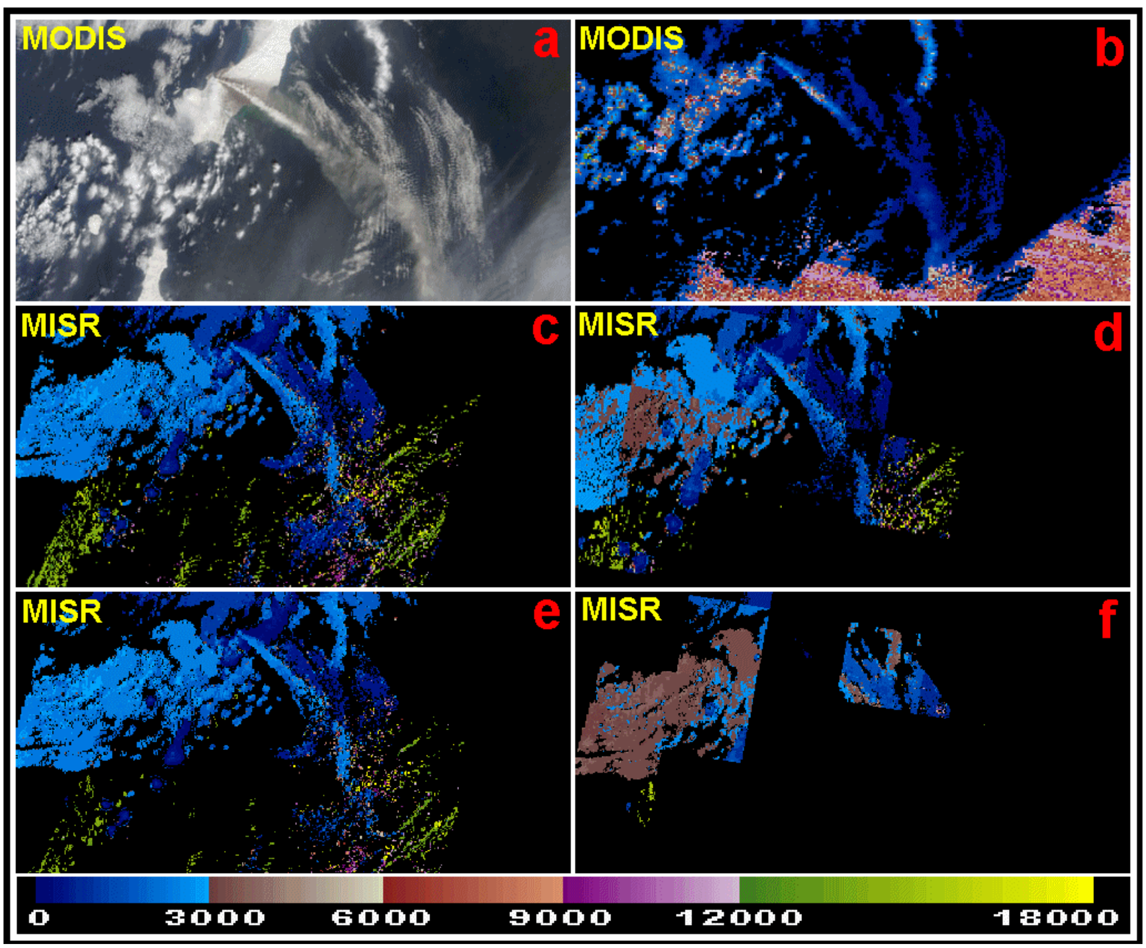

Figure 17. Eruption of the Chikurachki Volcano, 22 April 2003, 0054Z, observed by TERRA. a) MODIS true color image; b) MODIS CO_2-slicing height product; c) MISR *alpha* version "without winds" height product; d) MISR *alpha* version "best winds" height product; e) MISR *beta* version "without winds" height product; f) MISR *beta* version "best winds" height product.

Etna

29 October 2002

Mount Etna is located on the island of Sicily in Italy at 37.73^{o}N and 15.0^{o}E. MODIS and MISR height retrievals for the volcanic plume captured on 19 October 2002 (Figure 18) are in relative disagreement. MODIS CO_2-slicing yields a trimmed-mean height of 2161 meters, with an sd of 1833 meters. MISR's *alpha* and *beta* algorithms yield trimmed-mean heights of 4354 meters (1527 meters sd) and 3610 meters (2128 meters sd), respectively. Although MISR's *beta* algorithm does not retrieve much of Etna's plume, the trimmed data contains 731 points.

Manam

29 November 2004

The Manam Volcano is described in detail in Section IX of this study. On 29 November 2004, a low-level plume from Manam (Figure 19) was captured by MODIS and MISR. The CO_2-slicing and MISR *alpha* trimmed-means for the selected volcanic domain are again in disagreement with trimmed-mean heights of 866 meters (356 meters sd) and 2154 meters (1490 meters sd), respectively. It is clear from panels "d" and "f" that the MISR coverage for the volcanic plumes in the best winds product is lacking. This was definitely taken into account when determining the plume region selected for this plume's statistics. Unfortunately, MISR's *beta* height algorithm didn't retrieve any heights for this plume as seen in panel "f". Although 48 pixels from this algorithm were found in the collocated third grid, these pixels may have been extrapolated from anomalous surface retrievals and are not being considered in this analysis.

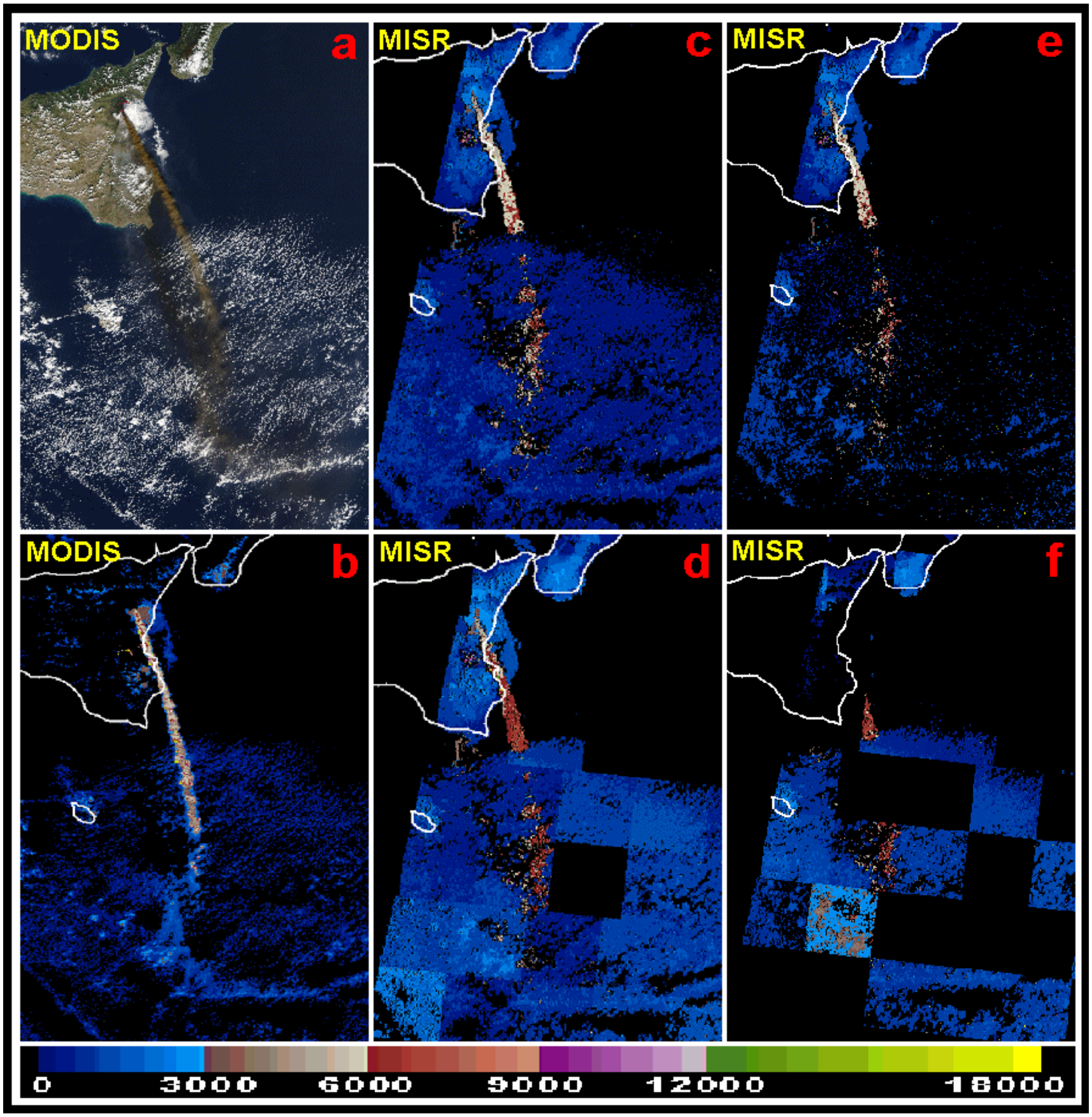

Figure 18. Eruption of the Etna Volcano, 29 October 2002, 0945Z, observed by TERRA. a) MODIS true color image; b) MODIS CO_2-slicing height product; c) MISR *alpha* version "without winds" height product; d) MISR *alpha* version "best winds" height product; e) MISR *beta* version "without winds" height product; f) MISR *beta* version "best winds" height product.

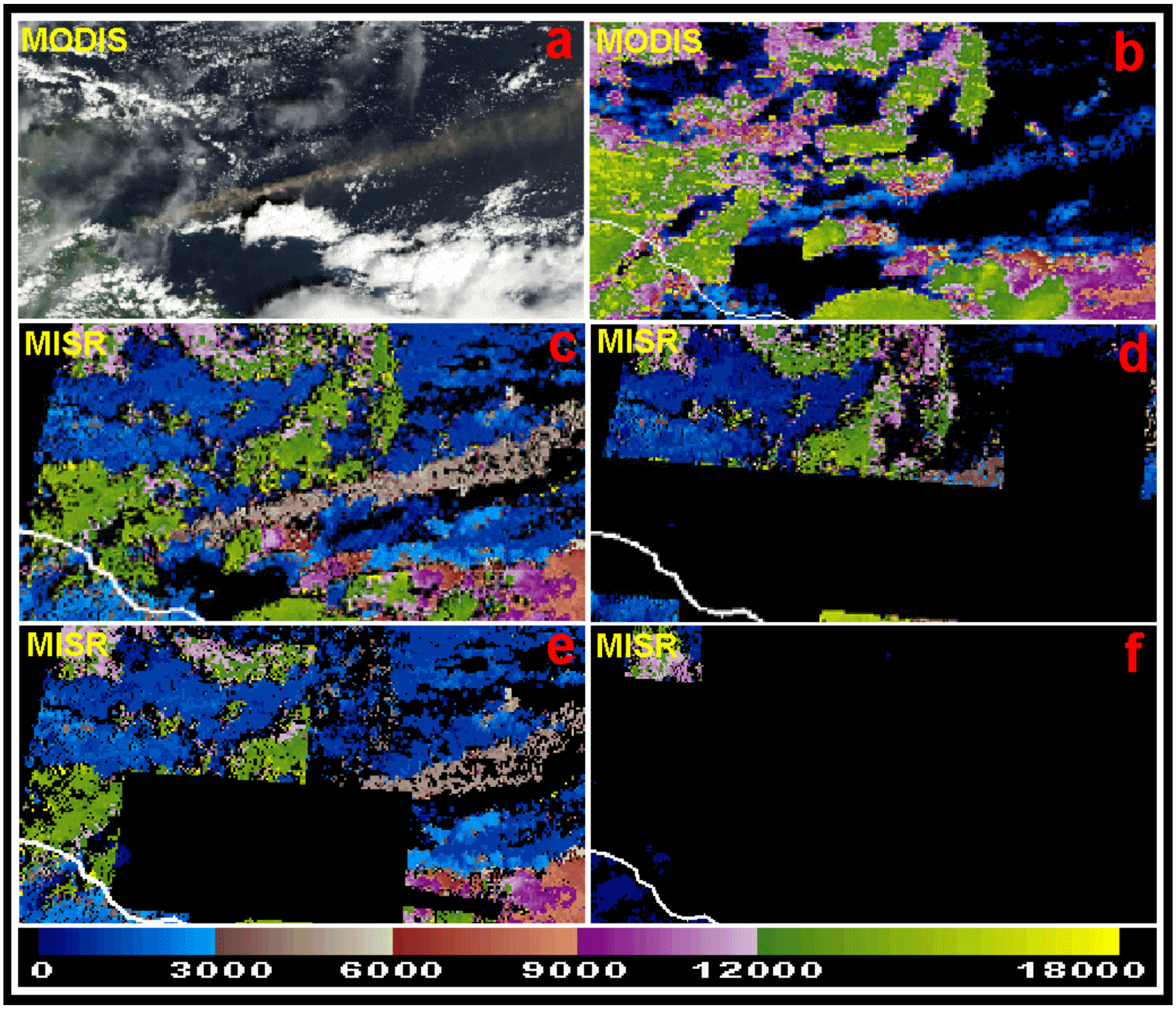

Figure 19. Eruption of the Manam Volcano, 29 November 2004, 0040Z, observed by TERRA. a) MODIS true color image; b) MODIS CO_2-slicing height product; c) MISR *alpha* version "without winds" height product; d) MISR *alpha* version "best winds" height product; e) MISR *beta* version "without winds" height product; f) MISR *beta* version "best winds" height product. *CO_2-slicing heights for this scene have been forced down to 1000mb.*

Table 3. Details on volcanic cases investigated for MODIS/MISR height retrieval comparison.

Volcano	Date	MODIS scan time	MISR orbit#/blocks	Lat/Lon box*
Anatahan	24 May 2003	0055Z	18242/77-79	lats: 16.0 / 15.25 lons: 145.9 / 145.8
Chikurachki	22 April 2003	0045Z	17776/49-51	lats: 50.25 / 50.0 lons: 156.0 / 155.75
Etna	22 July 2001	0955Z	08476/61-63	lats: 37.5 / 36.5 lons: 16.0 / 15.25
Etna[%,1]	27 October 2002	1000Z	15204/61-63	lats: 37.4 / 37.0 lons: 15.1 / 15.0
Etna[%,2]	27 October 2002	1000Z	15204/61-63	lats: 35.75 / 34.75 lons: 14.75 / 14.25
Etna	29 October 2002	0945Z	15233/60-62	lats: 37.0 / 36.5 lons: 15.5 / 15.25
Manam	29 November 2004	0040Z	26324/93-95	lats: -3.62 / -3.8 lons: 146.5 / 146.25

* Corners for latitude/longitude box that encapsulates the pixels used for the MODIS/MISR comparison. These corners were chosen so as to capture only volcanic pixels.
[%] This case refers to data plotted in Figure 22.
[1] Region 1 for this plume
[2] Region 2 for this plume

Figure 20 is a graphical representation of the data presented in Table 4. An alternative MODIS/MISR comparison is presented in Figure 22. This plot presents an additional two volcanic cases to the four already analyzed in this section. The additional two volcanic cases (Figure 21 – two separate regions) were not previously analyzed because, while they were 'collocatable' with the collocation algorithm, the plume region could not be segregated. This code issue is under investigation. The trimmed-mean heights presented in Figure 22 are not results from collocated data as in Figure 20. Figure 22 presents statistics from the segregated plume sections (as listed in Table 3) without collocation. Because MISR's height product is at a slightly higher resolution than MODIS', the number of pixels investigated for MISR will be less. Statistics for the MISR data come from MISR's *alpha* best winds height retrievals. The small discrepancies for these products' statistics between Figure 20 and Figure 22 are assumed to stem from the lower-resolution third grid used for the collocation.

Table 4. Comparison of MODIS CO_2-slicing and MISR height retrievals. Data is the trimmed-mean (middle 80%) for all heights retrieved in lat/lon box (in meters). Numbers in parentheses indicate number of pixels (from neutral third grid) used in retrieval. Numbers in brackets are the standard deviation for the trimmed data (in meters).

Eruption	MODIS CO_2-slicing*	MISR *alpha* "without winds"	MISR *alpha* "best winds"	MISR *beta* "without winds"	MISR *beta* "best winds"
Anatahan	**1732.6** (1538) [257.0]	**2127.3** (1538) [263.0]	**2247.3** (1538) [243.3]	**2354.2** (1523) [419.0]	**4980.5** (917) [0.0]
Chikurachki	**877.6** (720) [475.1]	**2061.5** (550) [500.2]	**2037.9** (561) [604.2]	**2087.7** (482) [442.7]	**3209.6** (12) [252.1]
Etna[1]	**2161.0** (2057) [1833.1]	**4364.2** (1413) [1601.3]	**4354.3** (1317) [1526.6]	**4274.3** (1330) [1723.5]	**3609.7** (731) [2127.9]
Manam	**865.9** (779) [356.3]	**3691.3** (877) [1482.8]	**2154.3** (753) [1490.4]	**3300.9** (760) [1524.4]	n/a[2]

* 11μm brightness temperature method is applied on fields of view where CO_2-slicing fails (see text for description).
[1] Etna eruption on 29 October 2002
[2] data believed invalid; see description in text

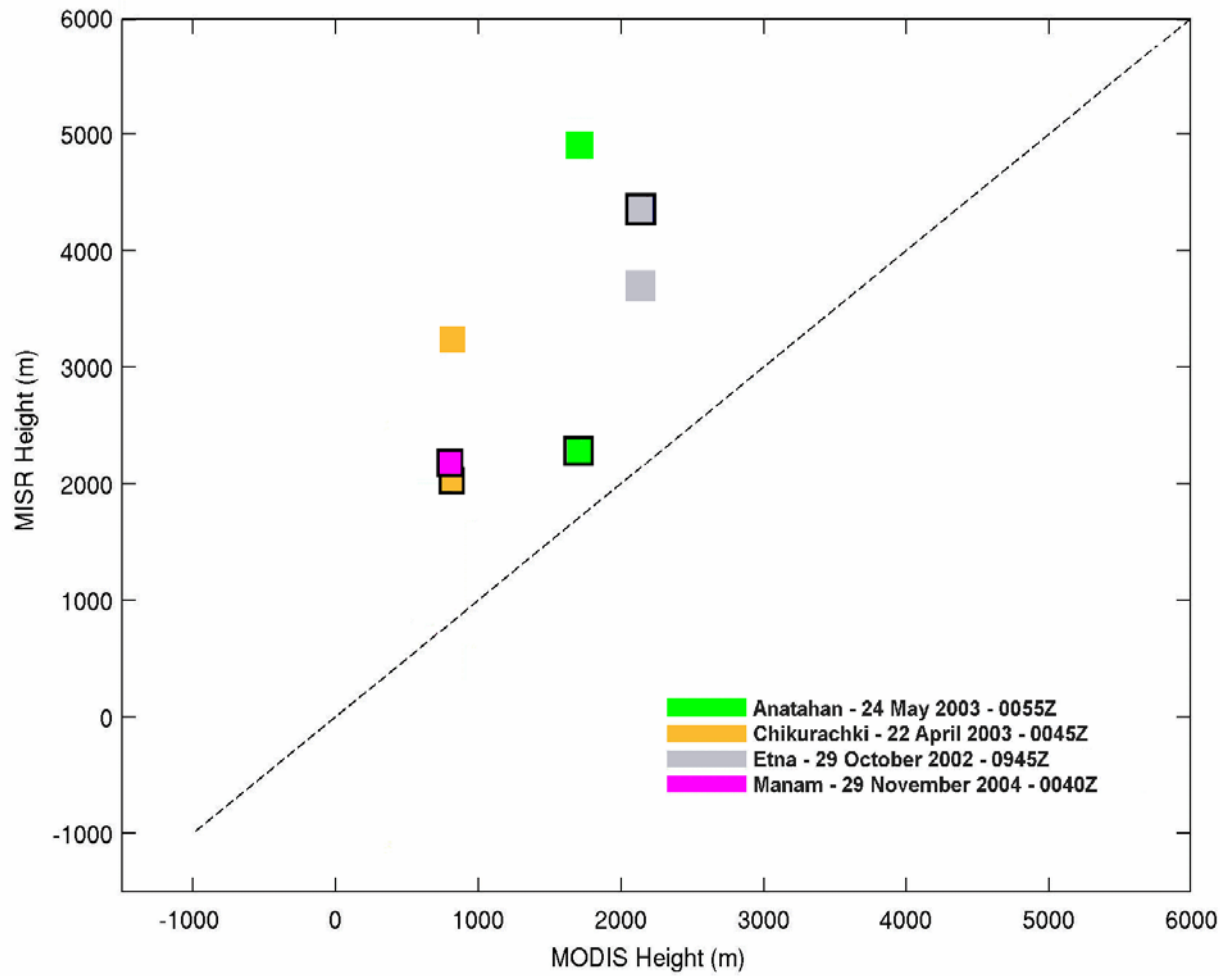

Figure 20. MODIS and MISR trimmed mean heights (middle 80%) for four volcanic eruptions after collocation. Plots representative of data in Table 4. Plots bounded in a black box refer to MISR's *alpha* height algorithm, non-black-box-bounded plots refer to MISR's *beta* height algorithm.

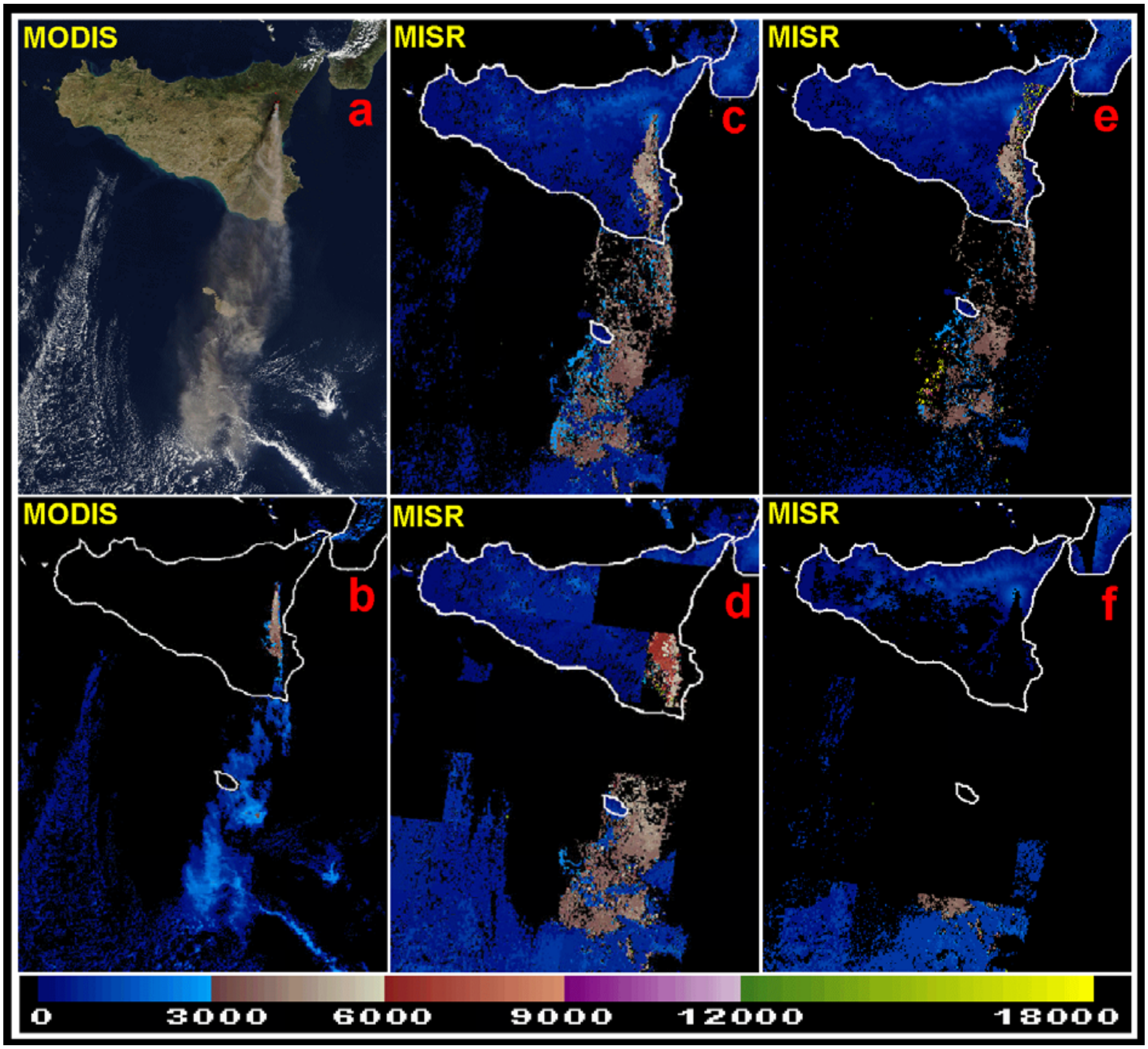

Figure 21. Eruption of the Etna Volcano, 27 October 2002, 1000Z, observed by TERRA. a) MODIS true color image; b) MODIS CO_2-slicing height product; c) MISR *alpha* "without winds" height product; d) MISR *alpha* "best winds" height product; e) MISR *beta* "without winds" height product; f) MISR *beta* "best winds" height product.

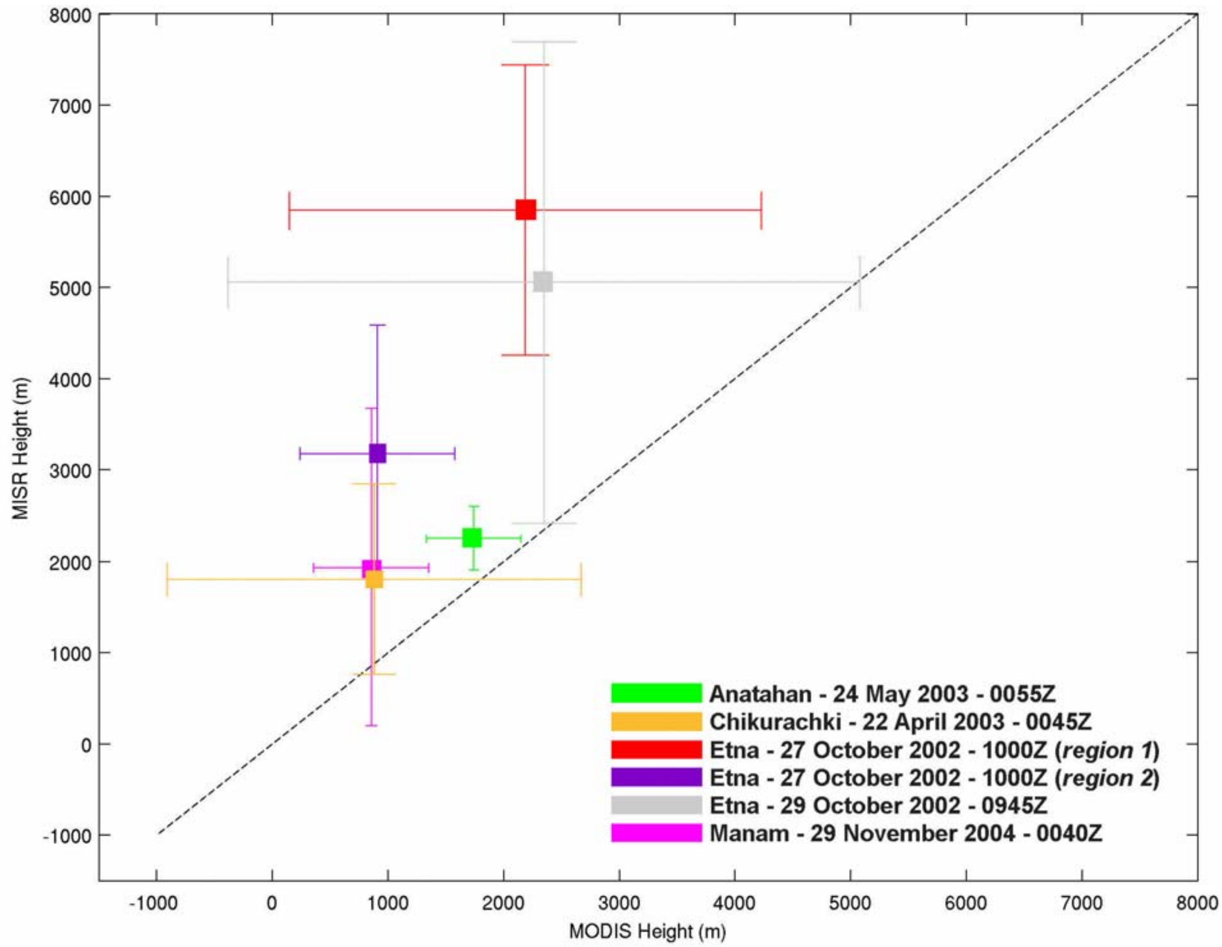

Figure 22. MODIS and MISR trimmed mean heights (middle 80%) for six volcanic eruptions without collocation. Whiskers on each plot represent the standard deviation for the trimmed data.

IX. CO_2-slicing heights compared with operational height estimation methods

Manam

The Manam volcano is located 12 kilometers north of Papua New Guinea at latitude 4.1S and longitude 141.06E. The Manam volcano is measured to be 1807 meters high. Numerous eruptions occurred at Manam between October 2004 and January 2005. These eruptions have been documented meteorologists, including those at the Darwin Volcanic Ash Advisory Centre (VAAC), Australia. The following analyses of the Manam eruptions are based on personal correspondence with Andrew Tupper (senior meteorologist – Darwin VAAC).

24 October 2004

The eruption of the Manam Volcano on 24 October 2004 was observed by MODIS (from both AQUA and TERRA) (Figure 23). Panels "b", "d" and "e" show the CO_2-slicing height products for 0105Z, 0355Z and 1620Z, respectively. The 0105Z height product indicates that the eruption plume disperses from the vent in two distinct sections. The first section travels to the northwest at a lower altitude then the other plume, eventually descending to a height indicated by CO_2-slicing to be below 3000 meters. The second plume section is the updraft column, which at this time has reached a CO_2-slicing retrieved height of 16.8km. The 0355Z MODIS imagery reveals that the updraft column had begun to drift to the north and expand, almost completely shielding the lower plume from view by the MODIS instrument on AQUA. CO_2-slicing heights put this higher cloud also at 16.8km. The 1620Z MODIS image shows that the CO_2-slicing technique has retrieved the heights for a volcanic ash cloud (enclosed in red circle) that is over twelve hours old. Maximum heights here are near

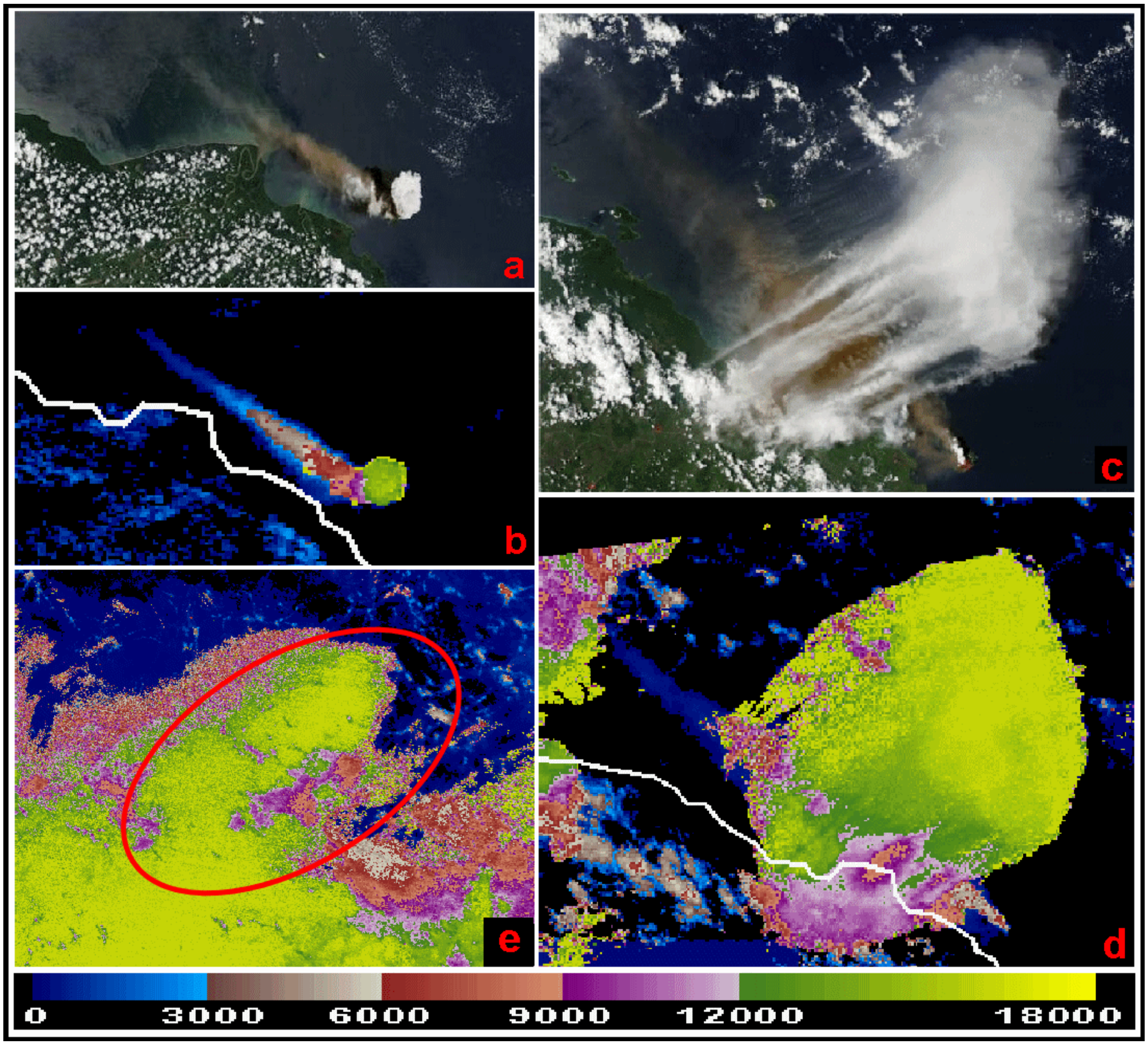

Figure 23. Eruption of Manam Volcano, 24 October 2004. a) MODIS [TERRA] true color image at 0105Z; b) MODIS [TERRA] CO_2-slicing height product at 0105Z; c) MODIS [AQUA] true color image at 0355Z; d) MODIS [AQUA] CO_2-slicing height product at 0355Z; e) MODIS [AQUA] CO_2-slicing height product at 1620Z, ash region circled in red.

16.4km. The heights retrieved for the three MODIS scans suggest that the volcanic cloud approached or entered the tropopause (defined using the GDAS profile used in the CO_2-slicing retrieval). Because CO_2-slicing cannot retrieve heights very near an isothermal region, maximum heights for this eruption are estimated to be between 16.5km and 17.0km.

The lowest infrared BTs for this eruption are –69^{o}C, which, according to local radiosonde data, places the cloud below the tropopause. The local radiosonde data, taken from Momote (approximately 348km northeast of Manam), at 00Z 24 October 2004 indicates the tropopause is near a height of 17.8km (Appendix A). Forward trajectories, however, indicate a height assignment of 18.5km might be more appropriate. Final operational estimates for this eruption cloud's height are 17-18.5km (Andrew Tupper – personal communication 2005). CO_2-slicing's height retrievals when compared to the operational estimates are within ±50hPa.

31 October 2004

CO_2-slicing heights for the 31 October 2004 eruption of the Manam Volcano are illustrated in Figure 24. The highest height value retrieved by CO_2-slicing in this eruption cloud is near 16.8km, presumably very near the tropopause region. An atmospheric sounding from Momote at 00Z, about one hour prior to the MODIS overpass, put the tropopause at approximately 16.4km. Darwin VAAC estimates for the height of this eruption cloud were made using shadow height and the BT method. The shadow height estimation method suggested height greater than 15.0km, while infrared cloud top brightness temperatures of approximately -80^{o}C put cloud top height near the 16.4km high tropopause. Final operational height estimates for this cloud are 16-16.5km (Andrew Tupper – personal communication 2005) with a final CO_2-slicing height estimate of 16.5-17.0km.

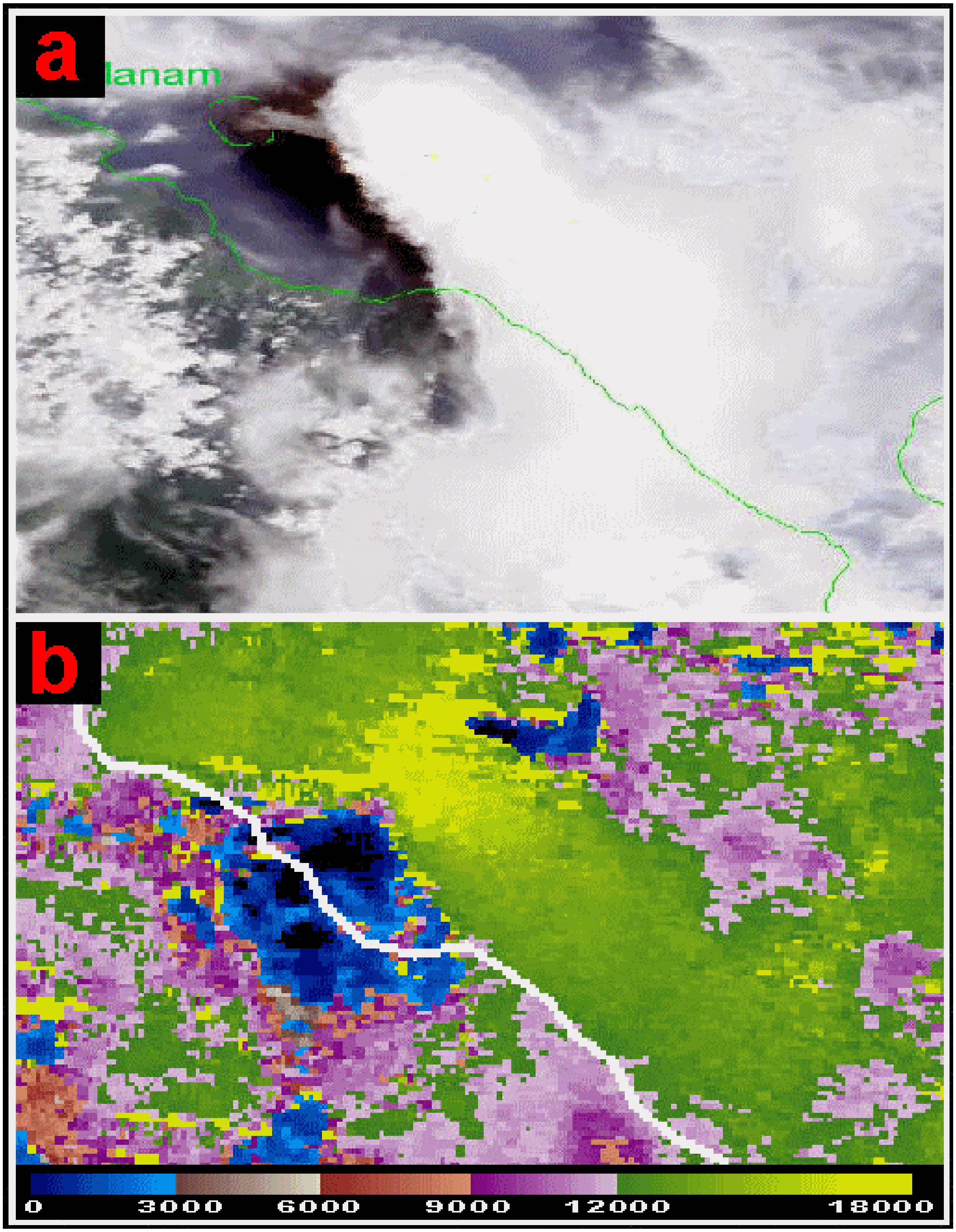

Figure 24. Eruption of Manam Volcano, 31 October 2004, 0110Z, observed by TERRA. a) MODIS true color image; b) MODIS CO_2-slicing height product for the troposphere at 1km resolution. *True color image courtesy of the Darwin VAAC.*

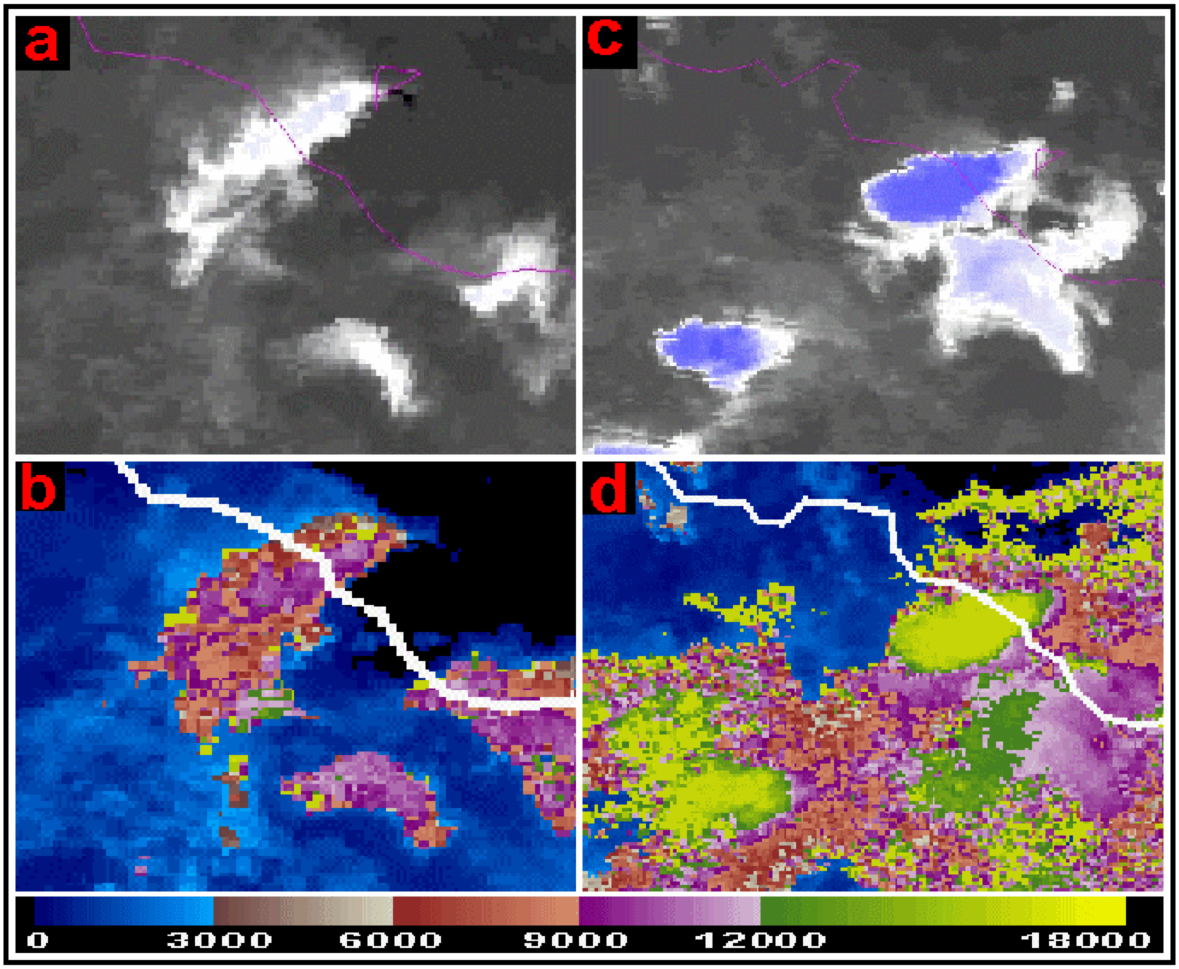

Figure 25. Eruption of Manam Volcano, 19 December 2004. a) MODIS [TERRA] 11μm image at 1235Z; b) MODIS [TERRA] CO_2-slicing height product at 1235Z; c) MODIS [AQUA] 11μm image at 1530Z; d) MODIS [AQUA] CO_2-slicing height product at 1530Z.

19 December 2004

The eruption of the Manam volcano on 19 December 2004 was captured twice by MODIS (Figure 25). Panels "c" and "d" show a well-defined plume extending east-southeast from the vent. CO_2-slicing height retrievals for the 1530Z MODIS scan yield maximum ash cloud heights near 16.7km. This case is quite similar to the 24 October 2004 and 31 October 2004

Manam cases as the highest parts of this cloud are believed to be at or in the tropopause region (where CO_2-slicing will retrieve a height coinciding with the coldest GDAS altitude). CO_2-slicing suggest maximum heights of 16.5-17.0km for this eruption scene. Minimum brightness temperatures of –80^{o}C from the 1530Z MODIS image, compared with a Momote radiosonde at 00Z on 20 December 2004 (Appendix B), put operational height estimates also at 16.5-17.0km.

27 January 2005

CO_2-slicing heights were also retrieved for the Manam eruption of 27 January 2005 (Figure 26). The center portions of this cloud were stratospheric (panel "c", green arrow) with an overshooting, 'undercooled' top of –71^{o}C, with a total stratospheric overshoot of 19^o-22^{o}C. The tropospheric version of the CO_2-slicing algorithm (panel "b") is not able to identify the stratospheric portions of the cloud as being above the tropopause and places heights near 12km. Because this portion of the cloud is independently known to be stratospheric, the stratospheric version of the CO_2-slicing algorithm may be applied to this case. CO_2-slicing yields maximum heights of 22-23km for the stratospheric cloud that had not been 'undercooled.' These height estimates correspond very well with operational estimates from the temperature data, which put the coldest stratospheric portions (-63^{o}C) in a height range of 21-24km. This height range was determined from radiosonde data from Momote at 00Z on 27 January 2005 (Appendix C).

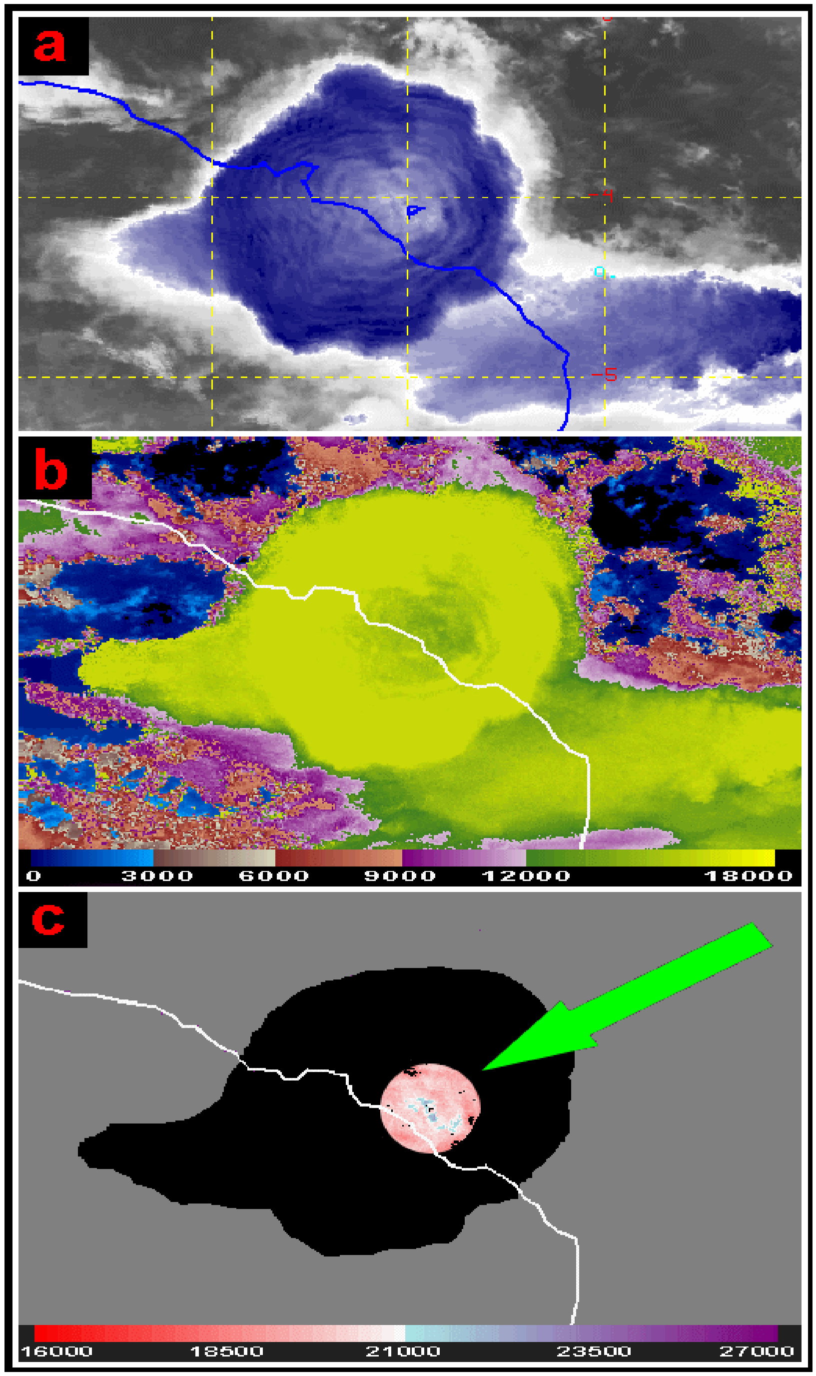

Figure 26. Eruption of Manam Volcano, 27 January 2005, 1535Z, observed by AQUA. a) MODIS 11µm image; b) MODIS CO_2-slicing height product for the troposphere; c) MODIS CO_2-slicing product for stratosphere. The majority of the volcanic cloud has been 'blacked out' to highlight the stratospheric cloud height retrievals. *11µm image courtesy of Darwin VAAC.*

Miyakejima

18-19 August 2000

Mount Oyama is located on the Japanese island of Miyake-Jima at latitude 34.08°N and longitude 139.52°E, and it has a height of 818.7 meters. Tupper et al. (2004) investigated this eruption (Figure 27) and, using wind-correlation methods, estimates that the ash cloud

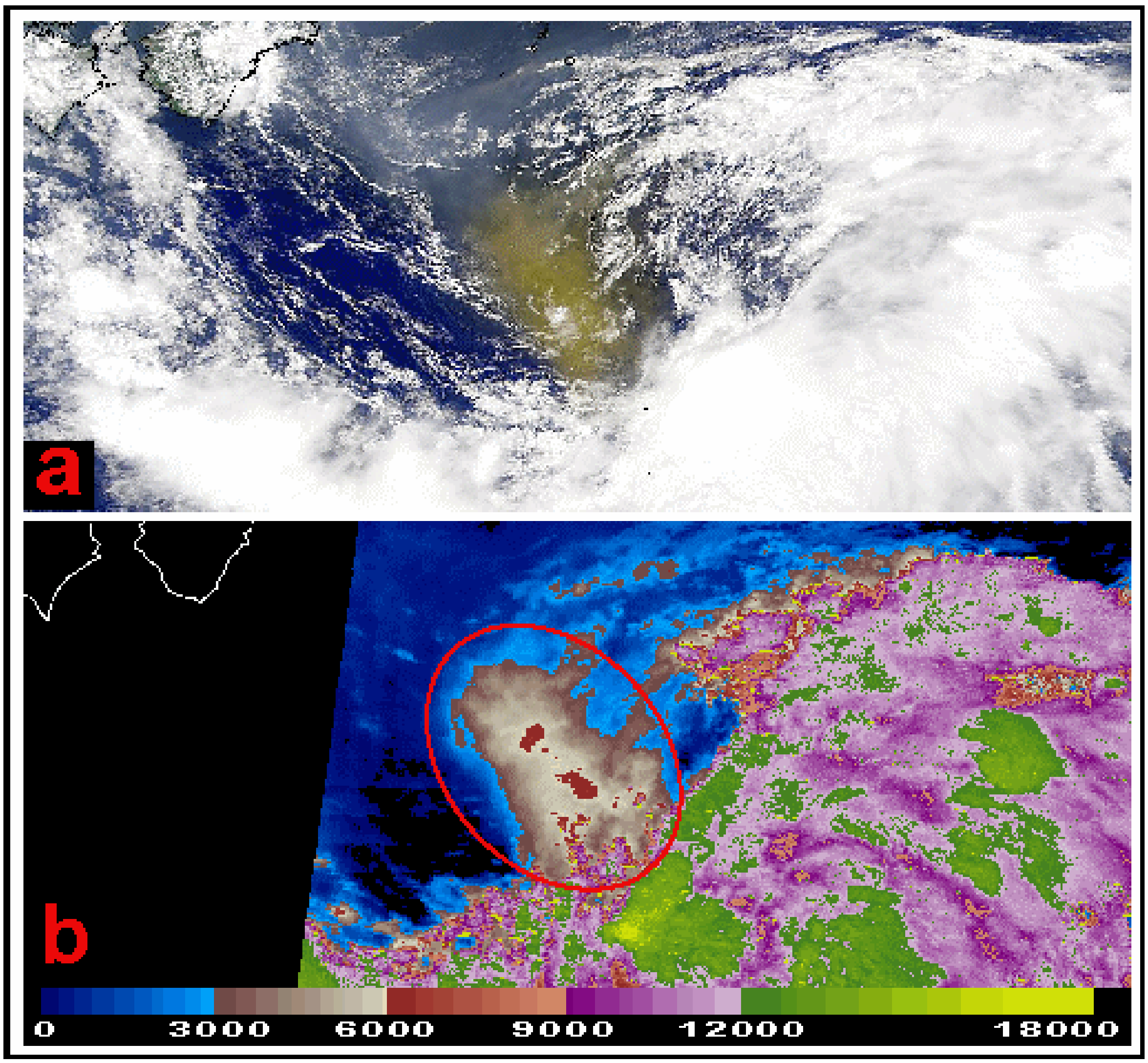

Figure 27. Eruption cloud from Miyakejima Volcano, 19 August 2000, 0105Z, observed by TERRA. a) MODIS true color image; b) MODIS CO_2-slicing height product, eruption cloud circled in red.

identified in panel "b" is at a height of 5-8km. CO_2-slicing height retrievals average at a lower altitude, with most cloud elements assigned heights of 3-6km. Maximum CO_2-slicing heights (6.5km) appear in the center of the cloud, where optical thickness is greatest. These height retrievals are a good match to the operational estimates (Andrew Tupper – personal communication 2005), however CO_2-slicing does appear to underestimate the heights in the optically thinner regions.

Ruang

25 September 2002

The Ruang Volcano is located at latitude 2.28^{o}N and longitude 125.425^{o}E in the Sangihe Islands of Indonesia. Its height is measured at 725 meters. MODIS passes at 0450Z and 1415Z on 25 September 2002 retrieved heights for volcanic clouds from Ruang (Figure 28). AQUA's pass at 0450Z captured the eruption cloud soon after it had pierced the stratosphere. Tupper et al. (2004) indicates that the highest heights retrieved operationally for this eruption were 21.5km by shadow method applied to MODIS. When all other height estimation techniques were considered, Tupper et al. (2004) arrived at a final height estimate of 20±2km. Because portions of this cloud are believed to be stratospheric, the stratospheric version of the CO_2-slicing methodology was applied to the 0450Z MODIS scan (panel "b", green arrow). CO_2-slicing technique yielded heights up to 21.2km for this scene. This height retrieval is in very good agreement with the operational estimates. Agreement with operational estimates for the CO_2-height retrievals from the 1415Z TERRA pass (panel "d") was not as strong, however. Cloud "D" found in panel "c" was estimated to be between 16-18km through operational methods (Tupper et al., 2004) while CO_2-slicing retrieved heights around 9±1km. The 16-18km operational estimate is made with high confidence (Andrew Tupper – personal communication 2005) and it is possible that MODIS missed the high cloud completely due to the cloud's low optical depth. The 9±1km heights may actually be retrievals from another cloud at a lower altitude.

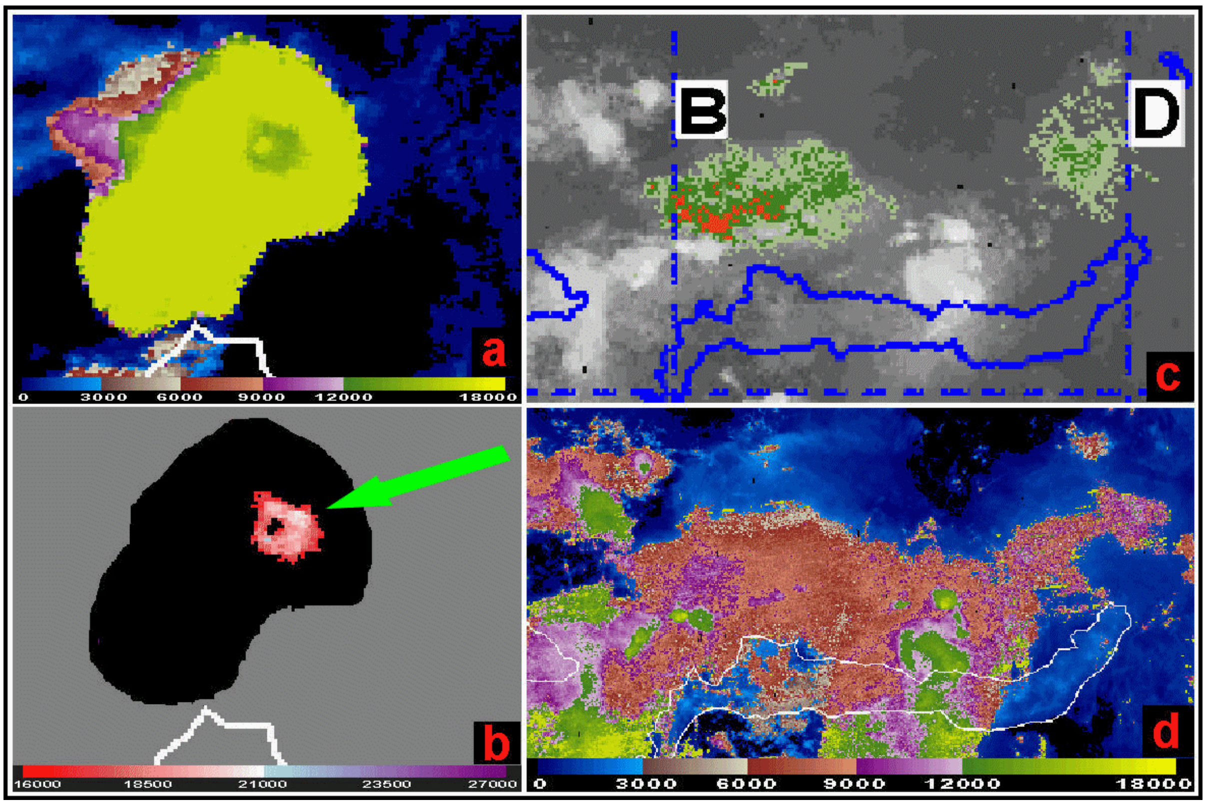

Figure 28. Eruption clouds from Ruang Volcano, 25 September 2002: a) MODIS [AQUA] CO_2-slicing height product for the troposphere at 0450Z; b) MODIS [AQUA] CO_2-slicing height product for the stratosphere at 0450Z. The majority of the volcanic cloud has been 'blacked out' to highlight the stratospheric cloud height retrievals; c) Image highlighting volcanic clouds for the TERRA 1415Z pass, colored regions highlight ash clouds with high confidence; d) MODIS [TERRA] CO_2-slicing height product at 1415Z. *Image in panel "c" taken from Tupper et al. (2004).*

Table 5. CO_2-slicing height estimates compared with operational estimates for volcanic eruptions. Except where noted, 'Times after eruptions' is the time after the initial volcanic eruption and are approximate.

Volcano	Date	MODIS time(s) (UTC)	Time after eruption	CO_2-slicing height estimate*	Operational height estimate#
Manam	24 October 2004	0105, 0355, & 1620	3 hours%	16.5km – 17km	17km – 18.5km (BT/wind)
Manam	31 October 2004	0110	16 hours	16.5km – 17km	16km – 16.5km (BT/shadow)
Manam	19 December 2004	1235 & 1530	12 hours$	16.5km – 17km	16.5km – 17km (BT)
Manam	27 January 2005	1535	1.5 hours	22km – 23km	21km – 24km (BT)
Miyakejima	19 August 2000	0105	17 hours[1]	3km – 6km, max ~6.5km	5km – 8km [1] (wind)
Ruang	25 September 2002	0450	70 min[1]	max ~21.2km	20±2km[1] (shadow/others)
Ruang	25 September 2002	1415	10.5 hours[1]	9±1km[2]	16km – 18km[1,2] (?)
Sheveluch	21 May 2001	0120	7 hours[4]	3km – 9km, max ~12km	max heights 6.7km & 4.9km[3] (BT)

* 11μm brightness temperature method is applied on fields of view where CO_2-slicing fails (see text for description).

Operational estimates courtesy Darwin/VAAC except where noted. Operational method(s) used in parenthesis.

% Corresponding to 0105Z MODIS pass

$ Time after intensification of eruption that began at 00Z 18 December 2004; corresponds to 1235Z MODIS pass

1 Tupper et al. (2004)

2 Estimation for cloud "D" in Figure 28, panel "c".

3 Operational estimates courtesy Tokyo/VAAC, see text for explanation.

4 Kamchatkan Volcanic Eruptions Response Team (KVERT) – via Tokyo VAAC

Sheveluch

20-21 May 2001

The Sheveluch Volcano (Figures 30 and 31) is located on the Kamchatka Peninsula in Russia at a latitude/longitude of 55.38°N/161.19°E with a summit height of 24447 meters. A TERRA pass on 21 May 2001 at 0120Z allowed MODIS to capture an eruption plume from Sheveluch. The height retrievals from this pass are presented in Figure 29, with the maximum CO_2-slicing heights approaching 12km, however most of the volcanic pixels seems to range from 3-9km. BT analysis performed by the Tokyo VAAC on products from the Japanese Geostationary Meteorological Satellite (GMS) estimate ash top heights at approximately 6.7km and 4.9km for 2132Z on 20 May 2001 and 0232Z on 21 May 2001, respectively (Yasuhiro Kamada/Tokyo VAAC – personal communication 2005). Yasuhiro Kamada does suggest, however, that if these volcanic clouds were semi-transparent, the BT-method heights would be under-estimates.

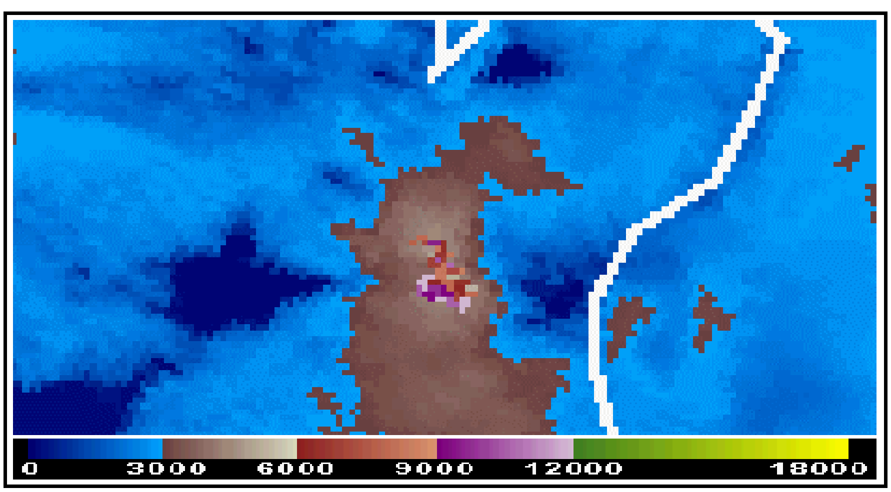

Figure 29. MODIS [TERRA] CO_2-slicing height product for eruption plume from the Sheveluch Volcano at 0120Z on 21 May 2001.

X. CO_2-slicing heights compared with heights estimated by video and photographic techniques

In this section, volcanic ash cloud heights produced by the CO_2-slicing methodology are compared to height estimates made by video and photographic and techniques. The volcanic eruptions presented here (Figure 32) occurred at the Sheveluch Volcano, and were chosen based on their recognizable plume signature. The video and photo height estimation techniques described here have been taken from Senyukov et al. (2004 – unpublished data) and personal correspondence with Sergey Senyukov (Research Laboratory of Seismic and Volcanic Activity, Kamchatkan Experimental-Methodical Seismological Department).

Video and photo imagery used for plume height analysis for the Sheveluch Volcano were made from the "Kluchi" seismic station (Figure 30). The volcano profile has been scaled using well-known altitudes of local features (Figure 31). For height estimates, each video or photographic image is rescaled to this volcano profile, allowing each eruption cloud to be measured by the same altitude scale. Senyukov et al. (data not yet published) indicates that there is error in the linear scale of the volcano profile. This error, however, which has been estimated to be 2% at 3 kilometer elevation, 3% at 10 kilometer elevation, and 5% at 15 kilometer elevation, is considerably less than errors that may arise from "deviation of the ash column from the vertical line." Senyukov et al. (2004 – unpublished data) also describes a method where volcanic plumes heights from Sheveluch are estimated using a purely seismic technique, and these results are compared to the photographic and video estimates. Results from this seismic method will not be presented in this study. The CO_2-slicing method has been forced down to 1000hPa for the cases shown here.

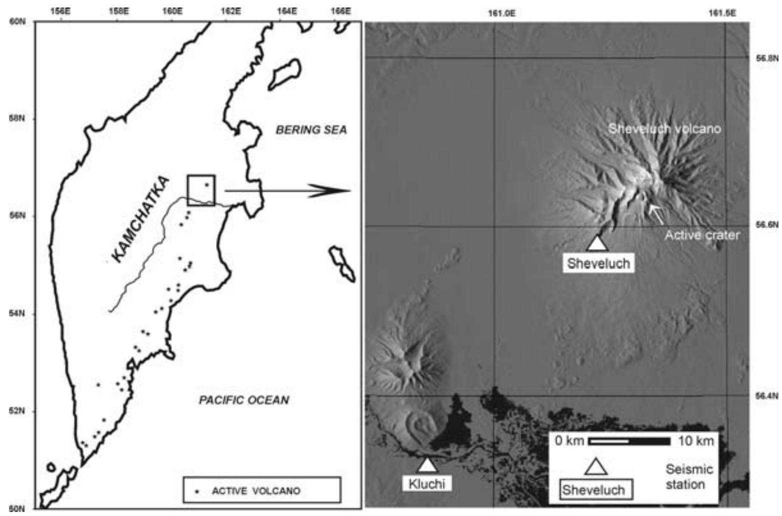

Figure 30. Map of the Kamchatka Penninsula, Russia and the Sheveluch volcano and its vicinity. Seismic station "Kluchi" is indicated by a triangular symbol. *Image taken from Senyukov et al. (2004 – unpublished data).*

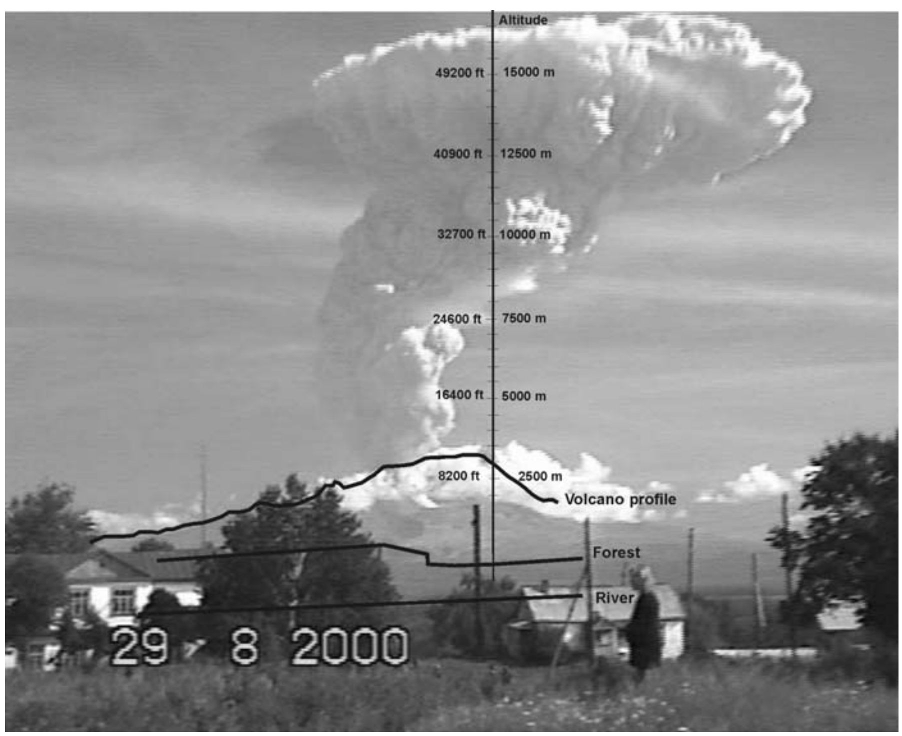

Figure 31. Sheveluch ash plume on 28 August 2000 at 2235Z with volcano profile overlaid on image. Photo by Yury Demyanchuk. *Image taken from Senyukov et al. (2004 – unpublished data).*

CO_2-slicing heights were retrieved for a MODIS pass at 0030Z on 23 August 2000 (panel “a”). This scan captured a volcanic plume from Sheveluch that has maximum retrieved heights near 16.2km. Approximately forty-five minutes prior to the MODIS pass, the video/photo technique estimates the ash column to be 17.5km high. A suggested error for this video/photo estimate is –42.86% and a possible source of this error is deviation of the eruption column from the vertical plain.

MODIS captured an eruption plume from Sheveluch at 2355Z on 28 August 2000 (panel “b”). Maximum CO_2-slicing heights for this plume are near 10.2km. About one and one half hour before this height retrieval, video/photo techniques estimated this eruption column to have a height of 16.5km. A suggested error for this video/photo estimate is –66.67%, again associated with the deviation of the eruption column from the vertical plain. This eruption is depicted in Figure 31.

At 0000Z on 27 August 2003, MODIS captured an eruption plume (panel “c”) that has maximum CO_2-slicing retrieved heights of near 3.8km. Estimates made by video/photo techniques at 0021Z, twenty-one minutes after the MODIS pass, place the eruption plume height at 3.5km.

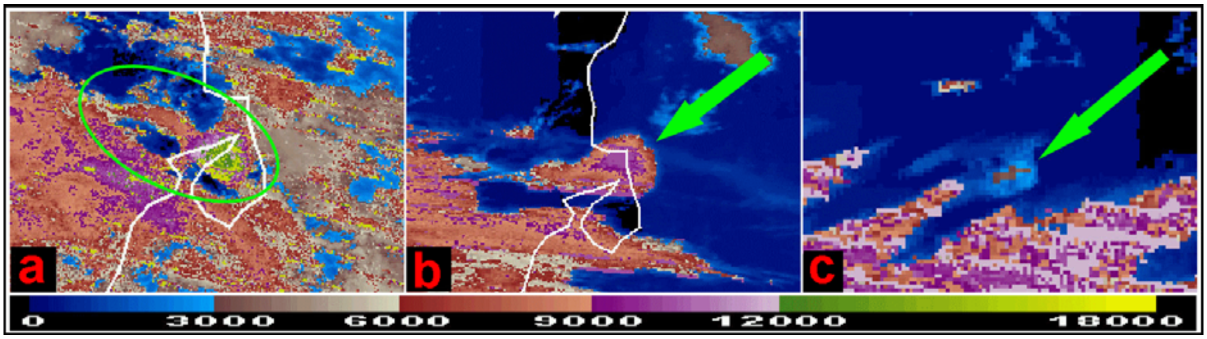

Figure 32. a) MODIS [TERRA] CO_2-slicing height products for Sheveluch eruptions. CO_2-slicing heights have been forced down to 1000hPa. a) 23 August 2000, 0030Z; b) 28 August 2000, 2355Z; c) 27 August 2003, 0000Z.

Table 6. CO_2-slicing height estimates compared with video/photo method estimations for Sheveluch Volcano

Date	Time(s) (UTC)	CO_2-slicing height estimate*	Video/photo height estimate#
23 August 2000	0030	16.2km	17.5km[1]
28 August 2000	2355	10.2km	16.5km[2]
27 August 2003	0000	3.8km	3.5km[3]

* 11μm brightness temperature method is applied on fields of view where CO_2-slicing fails (see text for description).

Video/photo estimates courtesy of Sergey Senyukov

1 Approximately 45 minutes prior to CO_2-slicing estimate

2 Approximately 90 minutes prior to CO_2-slicing estimate

3 Approximately 21 minutes after CO_2-slicing estimate

XI. Changes to the CO_2-slicing methodology in consideration of volcanic ash

The CO_2-slicing methodology is implemented with the assumption that cloud emissivities of the two spectral bands are equal. This assumption, however, may lead to errors in height retrievals. Zhang and Menzel (2002) investigated potential improvements to the cloud and surface emissivity assignments in the CO_2-slicing algorithm. Their study, which focused on high, thin cirrus clouds, found appropriate emissivity corrections that adjusted the cloud-top pressure retrievals for high, thin cirrus up to 10-20hPa (with root mean square bias differences of approximately 50hPa). In our study, we investigate potential adjustments to the cloud emissivity ratio in the CO_2-slicing algorithm in consideration of volcanic ash. The results presented here are not to be taken as necessary adjustments that should be implemented for volcanic ash clouds. Additional research, as well as a rigorous validation process, must be performed to establish new operational emissivity ratios. Rather, we provide these results to explore if this approach of including volcanic emissivity corrections to the CO_2-slicing algorithm would be useful.

The CO_2-slicing algorithm is based on a ratio of cloud signals for two closely spaced spectral bands (Equation {11} in section V). This ratio is built from the cloud-signals that are defined by Equation {10}. These ratios consist of a cloud fraction and a wavelength dependent cloud emissivity that may 'cancel' out with creation of Equation {11}. Neglecting the wavelength specific cloud emissivities is only possible if we consider them to be equal. If we do not make this assumption, the G-function would then become

$$G^{ij}(P_c) = \frac{I(v^i) - I_{CLR}(v^i)}{I(v^j) - I_{CLR}(v^j)} = \frac{\varepsilon_C{}^i \int_{P_s}^{P_c} t(v^i, P)\, dB\left[v^i, T(P)\right]}{\varepsilon_C{}^j \int_{P_s}^{P_c} t(v^j, P)\, dB\left[v^j, T(P)\right]} \qquad \{17\}$$

where all symbols are as they were before except for $\varepsilon_c{}^i$ and $\varepsilon_c{}^j$, which correspond to the cloud emissivity for wavelengths *i* and *j*, respectively. New height retrievals may now be conducted by the method described in section V.

Wavelength specific emissivities for volcanic ash are determined from the single scatter properties of the *andesite* mineral, which is a common model for "volcanic ash" (e.g. Yu et al, 2002; Pavolonis et al., 2005). The single scatter properties of andesite were determined by applying Mie calculations to assumed particle size distributions (containing only spherical particles) using the method outlined in Pavolonis et al. (2005). Asymmetry parameter, single scatter albedo, and the extinction (β_{ext}) and absorption (β_{sca}) coefficients were generated for five specific *effective radii* (0.33µm, 1.63µm, 2.41µm, 4.39µm, and 8.1µm) for each CO_2 band, where the *effective radius* for the size distribution is defined as the third moment over the second moment. Using these CO_2 band- and effective radius-dependent single scatter properties, β_{eff} is then approximated by substitution into Equation {18} (Parol et al., 1991):

$$\beta_{eff} \approx \frac{(1-\omega^i g^i)(1-\omega^j)}{(1-\omega^j g^j)(1-\omega^i)} \frac{\beta_{abs}{}^i}{\beta_{abs}{}^j} \qquad \{18\}$$

where ω is the single scatter albedo, g is the asymmetry parameter, $\beta_{abs} = \beta_{ext} - \beta_{sca}$ is the absorption coefficient, and β_{eff} is given in Giraud et al. (1997) by:

$$\varepsilon_c^{\ j} = 1 - \left[1 - \varepsilon_c^{\ i}\right]^{\beta_{eff}} \qquad \{19\}$$

The cloud emissivity ratios used by the CO_2-slicing algorithm are plotted in Figure 33 for the five effective radii.

Although there have been investigations into the physical size of ash particles from eruption plumes, due to the great variability of ash particle size from eruption to eruption, as well variability within the plumes themselves, β_{eff} is approximated (red dashed lines, Figure 33). By setting $\beta_{eff} = \varepsilon_c^{\ i} / \varepsilon_c^{\ j}$, we approximate the cloud emissivity ratio correction for band ratio 14.235μm/13.935μm to 1.07, and we approximate the corrections for band pairs 14.235μm/13.635μm, 13.935μm/13.635μm, 13.935μm/13.335μm, and 13.635μm/13.335μm to 0.93. Figure 34 presents a plot of Equation {19} for $\varepsilon_c^{\ i} / \varepsilon_c^{\ j}$ vs. $\varepsilon_c^{\ i}$ for $\beta_{eff} = 1.07$ (green) and $\beta_{eff} = 0.93$ (blue). Figure 34 indicates that these $\beta_{eff} = \varepsilon_c^{\ i} / \varepsilon_c^{\ j}$ approximations are appropriate for thinner volcanic ash (emissivity < ~0.6) as the adjusted emissivity corrections β_{eff} approximate the emissivity ratios better than the assumed ratio value of unity.

CO_2-slicing height retrievals have been run using the 1.07 and 0.93 emissivity correction factors for fifteen volcanic plumes presented in this study, and the results are presented in Figure 34 and Table 7. Figure 34 is a graphical representation of the pixel-by-pixel height changes that occurred for each of the volcanic plumes with the correction of cloud emissivities. Table 7 presents resultant height corrections in tabular form. The cloud emissivity corrections do not affect fields of view where the 11μm BT height retrieval method is used. Only pixels whose height was retrieved specifically by the CO_2-slicing algorithm are presented in these results. While the majority of volcanic plumes investigated in this study were almost entirely retrieved by the CO_2-slicing algorithm, several cases were limited to the 11μm method and are not presented here. In addition, several plumes (e.g. Chikurachki; Etna 27 Oct.) were retrieved *partially* by the CO_2-algorithm, and the height correction statistics for these cases do not reflect changes to the *entire* plumes.

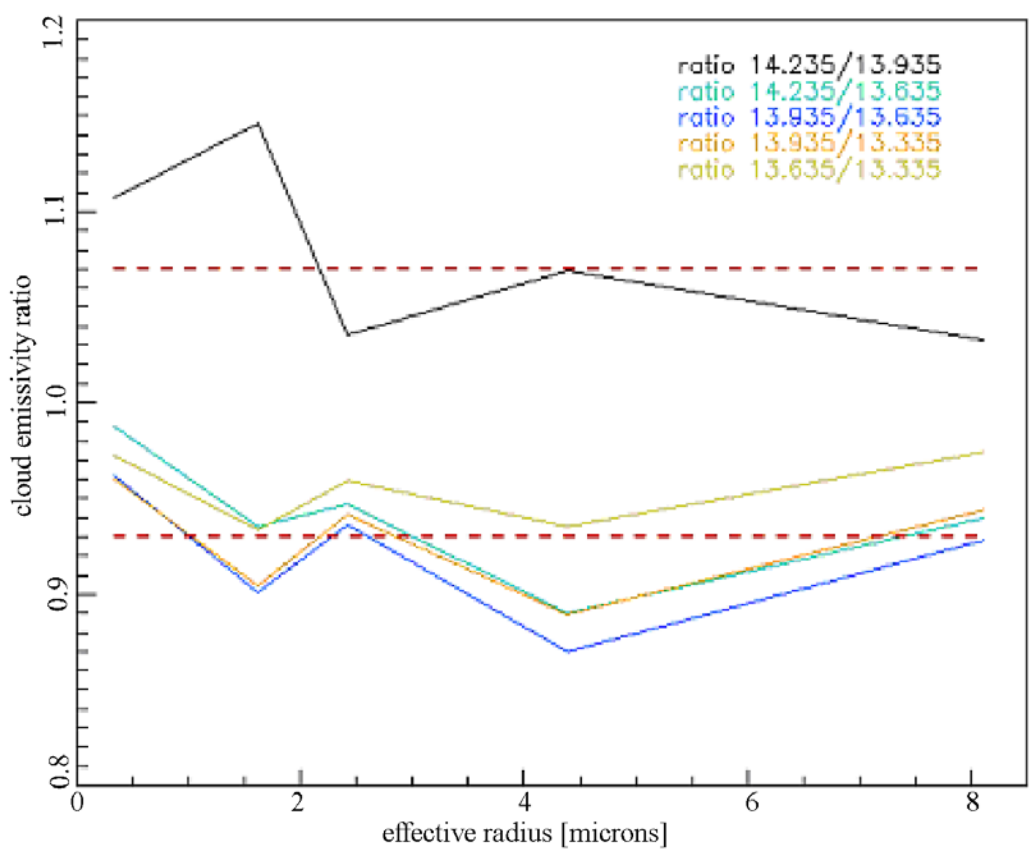

Figure 33. Cloud emissivity ratio plotted as a function of effective radius. Ratio corrections are indicated by the dashed red lines.

It should be noted that the MODIS trimmed-mean heights for several eruption clouds presented in Table 7 differ significantly from the MODIS trimmed-mean heights presented in Table 3 for the same clouds. The results presented in this section consider only pixels whose height was retrieved specifically by the CO_2-slicing algorithm, whereas the MODIS/MISR comparisons consider all pixels (either CO_2-slicing or 11µm method). The difference in means suggests that there were fields if view in the isolated lat/lon domains that were retrieved via the 11µm method, and that these fields of view were large in number compared to the number of fields of view retrieved by the CO_2-slicing algorithm and/or the fields of view retrieved by the 11µm method were significantly lower in heights than those retrieved by the CO_2-slicing algorithm.

Application of the 1.07 and 0.93 emissivity corrections causes an increase in the CO_2-slicing retrieved heights for all but one volcanic plume. For the fourteen plumes where the heights increased, the average increase is 870.5 meters. The average change to the heights for all cases with the emissivity correction is +755.4 meters. The height change for each plume was determined by calculating the difference between the pre- and post-adjusted trimmed-mean heights (pre-adjusted subtracted from post-adjusted). The trimmed-mean heights are mean values for the middle 80 percent of the individual plume data; the upper and lower 10 percent is not considered in order to prevent statistical contamination by outlying height values. The volcanic plumes we investigated reside in a variety of atmospheres and at differing altitudes. We applied the emissivity correction to two stratospheric cases: 1) Manam, 27 January 2005, 1535Z and 2) Ruang, 25 September 2002, 0450Z). While the application of the 1.07 and

0.93 emissivity correction increased the heights for the Ruang stratospheric ash cloud, it lowered the heights for the Manam ash cloud (Figure 34, panel "j") by 856.6 meters.

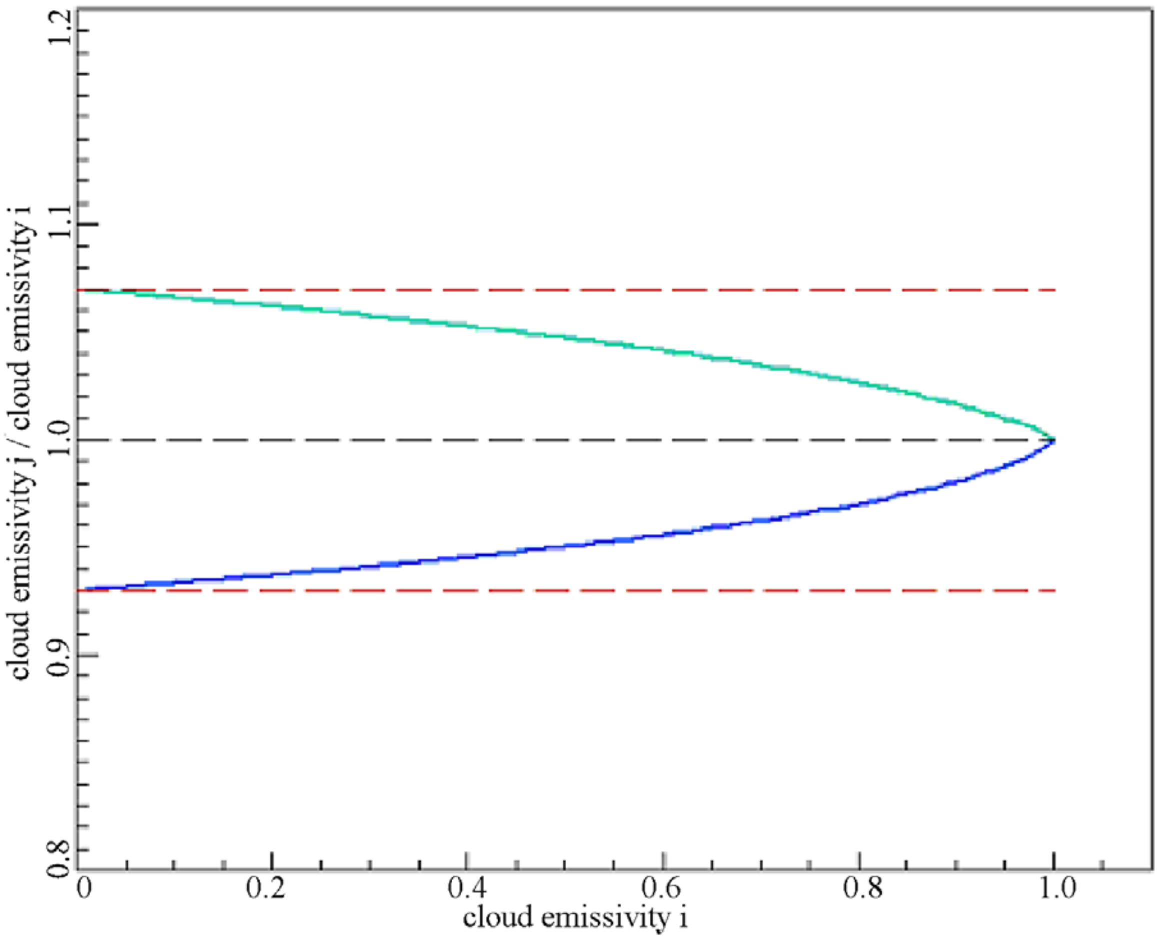

Figure 34. $\varepsilon_c^i / \varepsilon_c^j$ vs. ε_c^i for $\beta_{eff} = 1.07$ (green) and $\beta_{eff} = 0.93$ (blue) from Equation {19}. Red dashed lines indicate emissivity correction of 1.07 and 0.93.

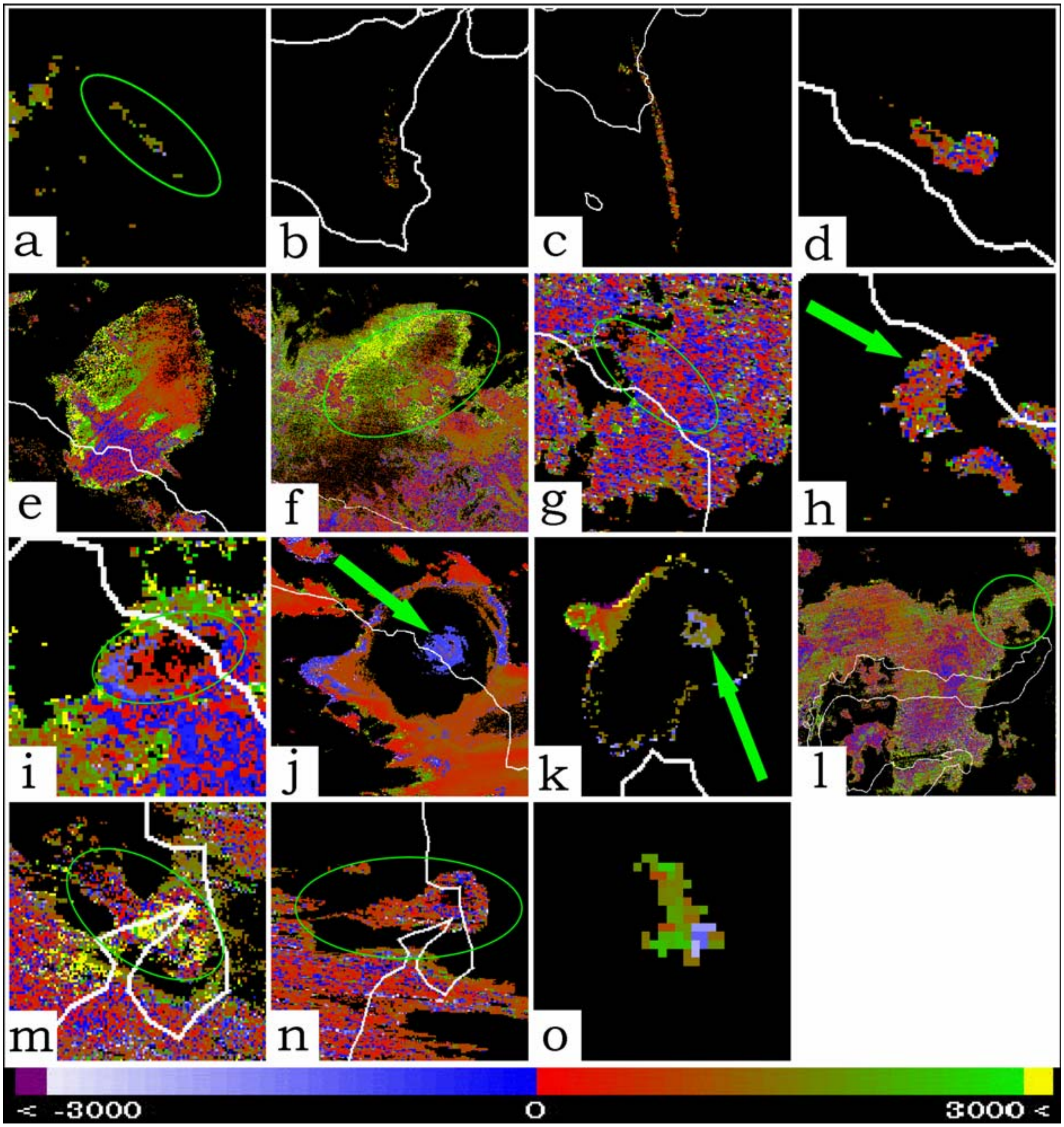

Figure 35. Height corrections to volcanic plumes from adjusted cloud emissivity ratios. Positive numbers indicate height increased with adjusted cloud emissivity ratios. a) Chikurachki, 22 April 2003, 0045Z; b) Etna, 27 October 2002, 1000Z; c) Etna, 29 October 2002, 0945Z; d) Manam, 24 October 2004, 0105Z; e) Manam, 24 October 2004, 0355Z; f) Manam, 24 October 2004,1620Z; g) Manam, 31 October 2004, 0110Z; h) Manam 19 December 2004, 1235Z; i) Manam, 19 December 2004, 1530Z; j) Manam, 27 January 2005, 1535Z; k) Ruang, 25 September 2002, 0450Z; l) Ruang, 25 September 2002, 1415Z; m) Sheveluch, 23 August 2000, 0030Z; n) Sheveluch, 28 August 2000, 2355Z; o) Sheveluch, 21 May 2001, 0120Z.

Table 7. CO_2-slicing height adjustments for volcanic ash plumes* in consideration of calculated cloud emissivity corrections

Volcano	Date	Time (UTC)	Pixels[1]	Trimmed-mean height[2]	Adjusted trimmed-mean height[3]	Height change[4]
Chikurachki	22 April 2003	0045	35	6431.5	7625.0	**1193.5**
Etna	27 October 2002	1000	140	4905.8	6017.0	**1111.2**
Etna	29 October 2002	0945	323	5409.5	6308.5	**899.0**
Manam	24 October 2004	0105	271	11375.0	11984.3	**609.3**
Manam	24 October 2004	0355	14062	14475.1	15437.7	**962.6**
Manam	24 October 2004	1620	7842	14835.4	16445.1	**1609.7**
Manam	31 October 2004	0110	244	15532.4	16008.1	**475.7**
Manam	19 December 2004	1235	659	9002.0	9476.2	**474.2**
Manam	19 December 2004	1530	158	16457.1	16598.0	**140.9**
Manam	27 January 2005	1535	1828	20015.2	19158.6	**-856.6**
Ruang	25 September 2002	0450	120	18668.5	19370.0	**701.5**
Ruang	25 September 2002	1415	2776	8895.5	9834.9	**939.4**
Sheveluch	23 August 2000	0030	661	12746.1	13970.6	**1224.5**
Sheveluch	28 August 2000	2355	1397	8409.4	8779.0	**369.6**
Sheveluch	21 May 2001	0120	37	8228.3	9704.8	**1476.5**

*Minor contamination by meteorological cloud is possible, though unlikely.

[1] The number of pixels investigated for each plume. The same pixels were used for both the 'trimmed-mean height' and the 'adjusted trimmed-mean height.' These pixels have been designated as "volcanic."

[2] The trimmed-mean height (middle 80% - in meters) for the volcanic pixels before the emissivity correction was applied.

[3] The trimmed-mean height (middle 80% - in meters) for the volcanic pixels after the emissivity correction was applied

[4] The height correction, calculated by ['trimmed-mean height' subtracted from 'adjusted trimmed-mean height'] (in meters)

XII. Conclusions and Future Work

This study compares the MODIS CO_2-slicing height product with heights retrieved from various other methods, including stereo height retrieval algorithms of MISR, flown on the same satellite. CO_2-slicing height estimations are also compared with operational height estimation techniques such as the 11μm brightness temperature technique, wind correlation methods, and a shadow technique, as well estimations made from a video/photo method. The CO_2-slicing height product is presented as a combination of the CO_2-slicing and 11μm height estimation products. For fields of view where the CO_2-slicing algorithm cannot be performed, height retrievals are supplemented via the 11μm brightness temperature method.

Pixel-to-pixel comparisons of the MODIS and MISR height products (Table 4) reveal that the CO_2-slicing product consistently retrieves lower heights than MISR for volcanic ash. For the cases presented in Table 4, MODIS does not come within 500 meters of either MISR height retrieval algorithm version. For the other three cases, MODIS does not come within 1000 meters of either MISR height retrieval algorithm version. An alternative MODIS/MISR height product comparison (Figure 22) reveals similar results with MODIS always retrieving lower height for volcanic ash. Figures 20 and 22 show that all six volcanic ash comparisons indicate MODIS to be lower than MISR. These volcanic ash plumes, however, are at relatively low altitudes, and the CO_2-slicing algorithm is not known to be accurate at altitudes below 700hPa. Figure 22 also indicates that the variability of these methods' height retrievals for these eruption are quite similar.

The CO_2-slicing height product is compared with operational techniques (e.g. 11μm BT-method, shadow technique, wind correlation methods) used professionally by meteorologists (Table 5). The CO_2-slicing height product compared well with the estimates made by the operational techniques for the majority of these cases. These volcanic plumes were at much higher altitudes overall than the MISR cases, with all but two residing near the tropopause or in the lower stratosphere. For the two stratospheric cases (Manam, 27 January 2005; Ruang, 25 September 2002 at 0450Z), the CO_2-slicing results fell squarely inside the three to four kilometer height window estimated by the operational techniques. Similar results are obtained for the tropopause cases (Manam, 24 October 2004; Manam, 31 October 2004; Manam, 19 December 2004; Ruang, 25 September 2002 at 1415Z), where the CO_2-slicing height product falls within ±50hPa of the operational estimate (Manam 31 October and 19 December were within ±25hPa) for three of the cases. In the fourth case (Ruang, 25 September 2002 at 1415Z), CO_2-slicing apparently misses the 'tropopausal' volcanic ash cloud completely and retrieves the height of an underlying cloud. CO_2-slicing estimates for the mid-troposphere also fall within the operation estimate windows, however their agreement is not as strong. For the vast majority of the Miyakejima volcanic cloud, the CO_2-slicing height estimates fall below the operational height estimates. Only the believed-to-be optically thick maxima produce height results that are high enough to fall within the operational estimate window. CO_2-slicing height results from Sheveluch 21 May 2001 vary too greatly to enable establishment of an official CO_2-slicing height estimate.

The CO_2-slicing height product is also compared with height estimates of volcanic plumes from the Sheveluch Volcano made by a video/photo technique (Table 6). The CO_2-slicing heights estimates for two of the cases compare well with the video/photo estimates. The first of these cases is a volcanic ash cloud near the tropopause (23 August 2000), where CO_2-slicing estimates the cloud to be 1.3 kilometers lower than the video/photo estimate made 45 minutes before. The second case is a lower-altitude plume (27 August 2003) where CO_2-slicing estimates 300 meters above the video/photo technique estimate made 21 minutes later. A third video/photo comparison shows CO_2-slicing falling well below the video/photo estimate. The video/photo technique estimated the height of the 28 August 2000 Sheveluch plume to be at a height of 16.5 kilometers. This estimate is 90 minutes after the MODIS overpass, where CO_2-slicing retrieved maximum heights of 10.2 kilometers.

The comparisons presented in this study suggest that improvements could be made to the MODIS CO_2-slicing methodology to improve its retrieval of volcanic ash cloud heights. While CO_2-slicing is seen to perform quite well for many cases (often the higher-altitude cases), the methodology often underestimates the height of airborne volcanic ash. Two situations where volcanic ash might be underestimated have been revealed in this study:

- The MODIS/MISR comparisons suggest that the CO_2-slicing height product might underestimate the height of low-level volcanic ash clouds. The cases investigated in this study were all retrieved by MODIS to be below 3000 meters, however MISR identified several of these clouds to be much higher (4–6 kilometers).
- Comparisons with operational techniques suggest that optically thin volcanic ash clouds might be a problem area for the CO_2-slicing methodology. The Miyakejima volcanic cloud (Figure 27) was an optically thin cloud around the edges, with regions of optically thick cloud in the middle (Andrew Tupper – personal communication

2005); the CO_2-slicing height retrievals varied accordingly. Evidence of a possible optical thickness limitation can be seen in the 28 August 2000 Sheveluch plume (Figure 32, panel "b"). The MODIS height retrieval was made 90 minutes after the video/photo estimate, which gave the higher ash particles time to descend to lower altitudes. While the video/photo technique saw the fine particles at the higher altitude, MODIS saw "through" them, retrieving heights from thicker cloud lying beneath. This perceived limitation is a topic for future research that is not restricted to volcanic ash clouds; it has applicability to cloud-top-pressure height retrievals for meteorological clouds.

An area of potential improvement to the CO_2-slicing algorithm is the cloud emissivity ratio assumption. For CO_2-slicing, the standard assumption is that the cloud emissivities for two spectrally close channels are the same (i.e. the cloud emissivity ratio is unity). This study investigated potential changes that could be made to this cloud emissivity assumption in consideration of volcanic ash. We arrived at cloud emissivity ratios that may be applied to volcanic ash clouds as *first corrections* to the standard cloud emissivity assumptions. Using cloud emissivity corrections of 1.07 (band combinations 36/35) and 0.93 (band combinations 36/34, 35/34, 35/33, and 34/33), MODIS CO_2-slicing height retrievals increased an average of 755.4 meters for fifteen volcanic ash cloud cases (Table 7). Only one of the fifteen cases investigated cases saw a decrease in heights with these emissivity corrections.

This is the first known investigation into the role CO_2-slicing might play in retrieving the heights of volcanic ash clouds. It is difficult to validate the height retrievals and thus where improvement needs to be made. The comparisons chosen for this study were based on their differing methodologies. While MISR is a space-borne instrument, it retrieves cloud heights by a stereophotogrammetric technique. The operational techniques were chosen due to their continued use amongst the scientists and meteorologists tracking volcanic ash clouds operationally in real- and near real-time. Additional future research aimed at determining CO_2-slicing's applicability to real- or near real-time estimation of volcanic ash cloud heights will need to focus on the cloud and surface emissivity assumptions inherent in the CO_2-slicing methodology. Emissivity adjustments in consideration of volcanic ash will likely differ from adjustments made for meteorological clouds. A necessary additional component to CO_2-slicing comparisons with other height estimation methods is an examination of the CO_2-slicing product itself. Cloud emissivity corrections will not affect height retrievals made by the 11μm BT-method. An investigation into the situations where CO_2-slicing fails and where the 11μm method is applied for volcanic ash clouds is appropriate. This will assist in determining appropriate adjustments to the CO_2-slicing algorithm.

XIII. References

Ardanuy, P. A., Han, D., and Salomonson, V. V., (1991) The Moderate Resolution Imaging Spectrometer (MODIS) science and data system requirements. *IEEE Transactions on Geoscience and Remote Sensing*, 29, 75–88.

Barnes, W. L., Pagano, T. S., and Salomonson, V. V. (1998) Prelaunch characteristics of the "Moderate Resolution Imaging Spectroradiometer (MODIS) on EOS-AM1. *IEEE Transactions on Geoscience and Remote Sensing*, 36, 1088–1100.

Baum, B. A. and Wielicki, B. A. (1994) Cirrus cloud retrieval using infrared sounding data: Multilevel cloud errors. *Journal of Applied Meteorology*, 33, 107-117.

Bedka, S. T., Feltz, W. F., Schreiner, A. J., and Holz, R. E. Satellite derived cloud top pressure product validation using aircraft based cloud physics lidar data from the AtREC field campaign. *International Journal of Remote Sensing* - accepted for publication.

Bruegge, C. J., Duval, V. G., Chrien, N. L., Korechoff, R. P., Gaitley, B. J., and Hochberg, E. B. (1998) MISR prelaunch instrument calibration and characterization results. *IEEE Transactions on Geoscience and Remote Sensing*, 36, 1186-1198.

Casadevall, T. J. (1994). The 1989-1990 eruption of Redoubt Volcano, Alaska: impacts on aircraft operations. *Journal of Volcanology and Geothermal Research*, 62, 301-316.

Casadevall, T. J. and M. D. Krohn (1995). Effects of the 1992 Crater Peak eruptions on airports and aviation operations in the United States and Canada. *U.S. Geological Survey Bulletin 2139*, 205-220.

Casadevall, T. J., Delos Reyes, P. J., and Schneider, D. J. (1996) The 1991 Pinatubo eruptions and their effects on aircraft operations, in *Fire and Mud: eruptions and lahars of Mount Pinatubo, Philippines*. Edited by C. G. Newhall and R. S. Punongbayan, pp. 637-645, Philippines, Institute of Volcanology and Seismology & University of Washington Press, Quezon City & Seattle.

Clothiaux, E. E., Ackerman, T. P., Mace, G. G., Moran, K. P., Marchand, R. T., Miller, M. A., and Martner, B. E. (2000) Objective determination of cloud heights and radar reflectivities using a combination of active remote sensors at the ARM CART sites. *Journal of Applied Meteorology*, 39, 645-665.

Diner D. J., Beckert, J. C., Reilly, T. H., Bruegge, C. J., Conel, J. E., Kahn, R. A., Martonchik, J. V., Ackerman, T. P., Davies, R., Gerstl, S. A. W., Gordon, H. R., Muller, J., Myneni, R. B., Sellers, P J., Pinty, B., and Verstraete, M. M. (1998) Multi-angle Imaging SpectroRadiometer (MISR) instrument description and experiment overview. *IEEE Transactions on Geoscience and Remote Sensing*, 36, 1072-1087.

Diner, D. J., Davies, R., DiGirolamo, L., Horvath, A., Moroney, C., Muller, J. -P., Paradise, S., Wenkert, D., and Zong, J. (1999) MISR level 2 cloud detection and classification algorithm theoretical basis document. Jet Propulsion Laboratory (JPL), California Institute of Technology, Pasadena, CA, *JPL Technical Document D-11399*.

Diner, D. J., Beckert, J. C., Bothwell, G. W., and Rodriguez, J. I. (2002) Performance of the MISR instrument during its first 20 months in orbit. *IEEE Transactions on Geoscience and Remote Sensing,* 40, 1449-1466.

Dunn, M. G. and Wade, D. P. (1994) Influence of Volcanic Ash Clouds on Gas Turbine Engines, in *Volcanic Ash and Aviation Safety - Proceedings of the First International Symposium on Volcanic Ash and Aviation Safety*. Edited by T. J. Casadevall, *U.S. Geological Survey Bulletin 2047*, 107-118.

Frey, R. A., Baum, B. A., Menzel, W. P., Ackerman, S. A., Moeller, C. C., and Spinhirne, J. D. (1999) Validation of CO_2-slicing cloud heights computed from MAS radiance data during SUCCESS. *Journal of Geophysical Researc*h, 104(D20), 24,547-24,555.

Giraud, V., Buriez, J. C., Fouquart, Y., Parol, F., and Seze, G. (1997) Large-scale analysis of cirrus clouds from AVHRR data: Assessment of both a microphysical index and the cloud-top temperature. *Journal of Applied Meteorology*, 36, 664-675.

Glaze, L. S., Francis, P. W., Self, S., and Rothery, D. A. (1989) The 16^{th} September 1986 eruption of Lascar volcano, north Chile: satellite investigations. *Bulletin of Volcanology*, 51, 149-160.

Grindle, T. J. and F. W. Burcham (2002) Even minor volcanic ash encounters can cause major damage to aircraft. *ICAO journal*, 57, 12-14, 29.

Holasek, R. E., Self, S., and Woods, A. W. (1996) Satellite observations and interpretation of the 1991 Mount Pinatubo eruption plumes. *Journal of Geophysical Research*, 100, 8469-8487.

Jin, Y., Gao, F., Shaaf, C. B., Li, X., Strahler, A. H., Bruegge, C. J., and Martonchik, J. V. (2002) Improving MODIS surface BRDF/albedo retrieval with MISR multiangle observations. *IEEE Transactions on Geoscience and Remote Sensing*, 40,1593-1604.

Johnson, R. W. and T. J. Casadevall (1994) Aviation safety and volcanic ash clouds in the Indonesia-Australia region. *U.S. Geological Survey Bulletin 2047*, 191-197.

Kahn, R., Banerjee, P., McDonald, D., and Martonchik, J. (2001) Aerosol properties derived from aircraft multiangle imaging over Monterey Bay. *Journal of Geophysical Research*, 106 (D16), 11977-11995.

King, M. D., Kaufman, Y. J., Menzel, W. P., and Tanré, D. (1992) Remote sensing of cloud, aerosol, and water vapor properties from the Moderate Resolution Imaging Spectrometer (MODIS). *IEEE Transactions on Geoscience and Remote Sensing*, 30, 2–27.

King, M. D., Menzel, W. P., Kaufman, Y. J., Tanre, D., Gao, B. –C., Platnick, S., Ackerman, S. A., Remer, L. A., Pincus, R., and Hubanks, P. A. (2003) Cloud and aerosol and water vapor properties, precipitable water, and profiles of temperature and humidity from MODIS. *IEEE Transactions Geoscience and Remote Sensing*, 41, 442-458.

Lacasse, C., Karlsdottir, S., Larsen, G., Soosalu, H., Rose, W. I., and Ernst, G. G. J. (2004) Weather radar observations of the Hekla 2000 eruption cloud, Iceland. *Bulletin of Volcanology*, 66, 457-473.

Lynch, J. S., and Stephens, G. (1996) Mount Pinatubo: A satellite perspective of the June 1991 eruption, in *Fire and Mud: eruptions and lahars of Mount Pinatubo, Philippines*. Edited by C. G. Newhall and R. S. Punongbayan, pp. 637-645, Philippines, Institute of Volcanology and Seismology & University of Washington Press, Quezon City & Seattle.

McGarragh, G. (2004) The effect of multilayered clouds on cloud pressure retrievals in near-global MODIS data. [Masters Thesis] Department of Atmospheric and Oceanic Sciences, University of Wisconsin-Madison, Madison, Wisconsin, USA.

McNutt, S. R. (1994) Volcanic tremor amplitude correlated with eruption explosivity and its potential use in determining ash hazards to aviation, in *Volcanic ash and aviation safety: proceedings of the First international symposium on Volcanic ash and aviation safety*. Edited by T. J. Casadevall. *U.S. Geological Survey Bulletin B 2047*, 377-385.

Menzel, W. P., Smith, W. L., and Stewart, T. R. (1983) Improved cloud motion wind vector and altitude assignment using VAS. *Journal of Applied Meteorology*, 22, 377-384.

Menzel, W. P., Wylie, D. P., and Strabala, K. I. (1992) Seasonal and diurnal changes in cirrus clouds as seen in four years of observations with the VAS. *Journal of Applied Meteorology*, 31, 370-385.

Moroney, C., Davies, R., and Muller, J. (2002a) Operational retrieval of cloud-top heights using MISR data. *IEEE Transactions on Geoscience and Remote Sensing*, 40, 1532-1540.

Moroney, C., Horvath, A., and Davies, R. (2002b). Use of stereo-matching to coregister multiangle data from MISR. *IEEE Transactions on Geoscience and Remote Sensing,* 40, 1541-1546.

Muller, J. –P., Mandanayake, A., Moroney, C., Davies, R., Diner, D. J., and Paradise S. (2002) MISR stereoscopic image matchers: Techniques and results. *IEEE Transactions on Geoscience and Remote Sensing*, 40, 1547-1559.

Naud, C., Muller, J. –P., Haeffelin, M., Morille, Y., and Delaval, A. (2004) Assessment of MISR and MODIS cloud top heights through inter-comparison with a back-scattering lidar at SIRTA. *Geophysical Research Letters*, 31, L04114, doi:10.1029/2003GL018976.

Oppenheimer, C. (1998) Volcanological applications of meteorological satellites. *International Journal of Remote Sensing*, 10, 2829-2864.

Parol, F., Buriez, J. C., Brogniez, G., and Fouquart, Y. (1991) Information content of AVHRR Channels 4 and 5 with respect to the effective radius of cirrus cloud properties. *Journal of Applied Meteorology*, 30, 973-984.

Pavolonis, M. J., Feltz, W. F., Heidinger, A. K., andGallina, G. M. (2005) A daytime compliment to the reverse absorption technique for improved automated detection of volcanic ash. Submitted to *Journal of Oceanic and Atmospheric Technology*.

Platnick, S., King, M. D., Ackerman, S. A., Menzel, W. P., Baum, B. A., Riédi, J. C., and Frey, R. A. (2003) The MODIS Cloud Products: Algorithms and Examples from Terra. *IEEE Transactions on Geoscience and Remote Sensing*, 41, 459-473.

Prata, A. J. (1989a) Observations of volcanic ash clouds using AVHRR-2 radiances. *International Journal of Remote Sensing*, 10 (4-5), 751-761.

Prata, A. J. (1989b) Radiative transfer calculations for volcanic ash clouds. *Geophysical Research Letters*, 16 (11), 1293-1296.

Prata, A. J., Bluth, G., Rose, B., Schneider, D., and Tupper, A. (2001) Comments on "Failures in detecting volcanic ash from a satellite-based technique". *Remote Sensing of Environment*, 78, 341-346.

Prata, A. J.and Grant, I. F. (2001) Determination of mass loadings and plume heights of volcanic clouds from satellite data. CSIRO Technical Paper 48, CSIRO Dept. of Atmospheric Science, Melbourne, Australia, 39 pp

Rose, W. I., Bluth, G. J. S., and Ernst, G. G. J. (2000) Integrating retrievals of volcanic cloud characteristics from satellite remote sensors: A summary. *Philosophical Transactions of the Royal Society of London*, A, 358, 1585-1606.

Rossier, R. N. (2002, February) Volcanic Ash: Avoid at all costs. *Business and Commercial Aviation*, 70-71.

Sawada, Y. (1987) Study on analysis of volcanic eruptions based on eruption cloud image data obtained by the Geostationary Meteorological Satellite (GMS). Meteorology Research Institute (Japan), Tokyo, 335 pp.

Seemann, S., Li, J., Menzel, W. P., and Gumley, L. (2003) Operational Retrieval of Atmospheric Temperature, Moisture, and Ozone from MODIS Infrared Radiances. *Journal of Applied Meteorology*, 42, 1072-1091.

Senyukov, S. L., Droznin, D. V., and Droznina, S. Ya. (2004 – unpublished data) The ongoing eruption of Sheveluch Volcano (Kamchatka Peninsula, Russia): Remote determination of ash plume initiation and height using local seismicity. Kamchatkan Experimental-Methodical Seismological Department GS RAS.

Simpson, J. J., Hufford G., Pieri D., and Berg, J. (2000a) Failures in detecting volcanic ash from a satellite-based technique. *Remote Sensing of Environment*, 72, 191-217.

Simpson, J. J., McIntire, T., Jin, Z., and Stitt, J. R. (2000b) Improved cloud top height retrieval under arbitrary viewing and illumination conditions using AVHRR data. *Remote Sensing of the Environment*, 72, 95-110.

Simpson, J. J., Hufford, G. L., Pieri, D., Servranckx, R., Berg, J. S., and Bauer, C. (2002) The February 2001 eruption of Mt. Cleveland, Alaska: a case study of an aviation hazard. *Weather and Forecasting*, 17, 691-704.

Smith, W. L., and Platt, C. M. R. (1978) Comparison of satellite-deduced cloud heights with indications from radiosonde and ground-based laser measurements. *Journal of Applied Meteorolog*y, 17, 1796-1802.

Soulakellis, N., Yates, J., and Tataris, G. (2003) Global Island Image-Maps (GIIM): A set of digitally processed MODIS images. *International Cartographic Association 2003 Conference*. Durban, South Africa.

Sparks, R. J. S. and Wilson, L. (1982) Explosive volcanic eruptions – V. Observations of plume dynamics during the 1979 Soufrière eruption, St Vincent. *Geophysical Journal of the Royal Astronomical Society*, 69, 551-570.

Tupper, A. S., and Kinoshita, K. (2003) Satellite, air and ground observations of volcanic clouds over islands of the southwest Pacific. *South Pacific Study*, 23, 21-46.

Tupper, A., Kinoshita, K., Kanagaki, C., Iino, N., and Kamada, Y. (2003) Observations of volcanic cloud heights and ash-atmosphere interactions. WMO/ICAO Third International Workshop on Volcanic Ash, Toulouse, France, September 29 -October 3, 2003.

Tupper, A., Carn, S., Davey, J., Kamada, Y., Potts, R., Prata, F., and Tokuno, M. (2004) An evaluation of volcanic cloud detection techniques during recent significant eruptions in the western 'Ring of Fire'. *Remote Sensing of Environment*, 91, 27-46.

Tupper, A., Oswalt, J. S., and Rosenfeld, D. (2005) Satellite and radar analysis of the volcanic-cumulonimbi at Mount Pinatubo, Philippines, 1991. *Journal of Geophysical Research*, 110(D09204): doi:10.1029/2004JD005499.

Wielicki, B. A. and Coakley Jr., J. A. (1981) Cloud retrieval using infrared sounder data: Error analysis. *Journal of Applied Meteorology*, 20, 157-169.

Wylie, D. P., and Menzel, W. P. (1989) Two years of cloud cover statistics using VAS. *Journal of Climate,* 2, 380–392.

Wylie, D. P., Menzel, W. P., Woolf, H. M., and Strabala, K. I. (1994) Four years of global cirrus cloud statistics using HIRS. *Journal of Climate*, 7, 1972-1986.

Yu, T. X., Rose, W. I., and Prata, A. J. (2002) Atmospheric correction for satellite-based volcanic ash mapping and retrievals using "split window" IR data from GOES and AVHRR. *Journal of Geophysical Research*, 107 (D16), 4311.

Zhang H. and Menzel, W. P. (2002) Improvement in thin cirrus retrievals using an emissivity-adjusted CO_2 slicing algorithm. *Journal of Geophysical Research*, 107 (D17), 4327.

XIV. Appendices

Appendix A. Radiosonde observations from Momote at 00Z on 24 October 2004.

92044 Momote W.O. Observations at 00Z 24 Oct 2004

PRES hPa	HGHT m	TEMP C	DWPT C	RELH %	MIXR g/kg	DRCT deg	SKNT knot	THTA K	THTE K	THTV K
1011.0	5	30.8	23.8	66	18.76	70	6	303.0	358.9	306.4
1002.0	86	28.4	22.4	70	17.35	78	6	301.4	352.7	304.5
1000.0	104	28.4	22.4	70	17.39	80	6	301.6	353.0	304.7
960.0	466	25.0	21.5	81	17.14	104	5	301.6	352.4	304.7
925.0	793	23.0	18.3	75	14.52	125	4	302.8	346.1	305.5
900.0	1030	21.3	17.8	81	14.48	110	4	303.4	346.6	306.1
899.0	1040	21.2	17.8	81	14.48	110	4	303.4	346.6	306.1
800.0	1864	15.8				110	6	307.9		307.9
788.0	1971	15.1				75	2	308.5		308.5
95.7	16875	-83.3				85	6	371.2		371.2
83.0	17658	-84.2				35	19	384.6		384.6
80.0	17860	-84.5				31	15	388.2		388.2
79.0	17930	-81.0				30	14	396.7		396.7
78.5	17965	-79.3				3	9	401.1		401.1
78.0	18001	-78.8				335	4	402.8		402.8
76.4	18119	-77.3				258	3	408.4		408.4
75.0	18225	-76.7				190	2	411.9		411.9
70.0	18620	-74.3				205	8	425.1		425.1
67.0	18883	-72.8				210	12	433.7		433.7
66.0	18973	-72.3				235	17	436.7		436.7
64.0	19158	-71.2				245	23	442.9		442.9
58.0	19749	-67.8				235	14	463.2		463.2
56.0	19960	-66.6				215	12	470.6		470.6
53.0	20290	-64.7				245	10	482.5		482.5
52.0	20405	-64.0				270	8	486.6		486.6
51.0	20521	-63.4				325	14	490.9		490.9
50.0	20640	-62.7				320	19	495.3		495.3
48.0	20893	-62.5				325	23	501.5		501.5
47.0	21023	-62.5				305	21	504.7		504.7
43.0	21573	-62.1				305	17	518.6		518.6
42.0	21719	-62.0				320	21	522.3		522.3
40.0	22020	-61.8				310	31	530.1		530.1
36.0	22672	-61.4				285	14	547.4		547.4
35.0	22846	-61.3				245	17	552.1		552.1
32.0	23401	-61.0				240	37	567.3		567.3
30.0	23800	-60.7				240	29	578.6		578.6
29.0						230	21			
27.0						280	17			

Appendix B. Radiosonde observations from Momote at 00Z on 20 December 2004.

92044 Momote W.O. Observations at 00Z 20 Dec 2004

PRES hPa	HGHT m	TEMP C	DWPT C	RELH %	MIXR g/kg	DRCT deg	SKNT knot	THTA K	THTE K	THTV K
1010.0	5	31.0	23.0	62	17.87	30	6	303.3	356.6	306.5
1007.0	30	29.2	22.2	66	17.05	31	6	301.8	352.3	304.8
1000.0	89	28.8	24.2	76	19.45	35	6	301.9	359.7	305.4
955.0	498	25.0	23.4	91	19.41	47	8	302.1	359.7	305.6
925.0	779	23.0	20.5	86	16.71	55	10	302.8	352.5	305.9
923.0	798	22.8	20.5	87	16.75	56	10	302.8	352.6	305.8
850.0	1513	19.2	15.5	79	13.20	85	10	306.2	346.1	308.7
825.0	1769	17.7	14.3	80	12.55	90	8	307.3	345.4	309.6
773.0	2326	14.4	11.6	83	11.22	88	9	309.5	344.0	311.6
701.0	3150	11.6	2.6	54	6.63	85	10	315.2	336.4	316.4
700.0	3162	11.6	2.6	54	6.64	85	10	315.3	336.5	316.6
623.0	4119	5.6	0.2	68	6.27	80	17	319.1	339.5	320.3
574.0	4791	1.4	-1.5	81	6.01	75	16	321.7	341.5	322.9
534.0	5366	-2.0	-5.7	76	4.71	70	16	324.4	340.2	325.3
500.0	5890	-5.1	-9.5	71	3.74	65	12	326.8	339.6	327.5
485.0	6129	-6.9	-10.6	75	3.54	53	12	327.4	339.6	328.1
482.0	6177	-6.8	-13.7	58	2.78	50	12	328.2	337.9	328.7
481.0	6194	-6.7	-14.7	53	2.56	50	12	328.4	337.4	328.9
473.0	6324	-7.3	-19.3	38	1.77	52	11	329.3	335.6	329.6
457.0	6592	-9.3	-14.3	67	2.78	55	10	330.0	339.8	330.6
446.0	6780	-10.5	-21.5	40	1.55	57	9	330.8	336.4	331.1
436.0	6954	-11.5	-18.5	56	2.05	59	8	331.7	339.1	332.1
409.0	7442	-14.5	-26.5	35	1.08	65	6	333.9	338.0	334.1
400.0	7610	-15.5	-25.5	42	1.21	50	8	334.8	339.3	335.0
389.0	7819	-17.6	-25.5	50	1.24	55	12	334.8	339.4	335.0
384.0	7916	-18.5	-25.5	54	1.26	57	13	334.7	339.4	335.0
379.0	8014	-18.9	-23.7	66	1.50	59	15	335.5	341.0	335.8
371.0	8172	-19.3	-26.3	54	1.21	63	18	337.0	341.6	337.2
356.0	8476	-21.2	-26.9	60	1.19	70	23	338.4	342.9	338.7
333.0	8968	-24.3	-27.9	72	1.16	64	27	340.7	345.2	340.9
318.0	9302	-26.3	-35.3	42	0.60	60	30	342.4	344.9	342.6
303.0	9649	-29.1	-38.1	42	0.47	55	33	343.3	345.2	343.4
300.0	9720	-29.9	-37.9	46	0.49	55	33	343.1	345.1	343.2
281.0	10182	-33.5	-38.6	60	0.48	65	25	344.4	346.4	344.5
279.0	10232	-33.9	-38.7	62	0.48	65	26	344.6	346.5	344.6
271.0	10435	-35.1	-45.1	35	0.25	67	28	345.7	346.8	345.7
250.0	10990	-40.7				70	33	345.4		345.4
210.0	12153	-50.1				82	39	348.4		348.4
200.0	12470	-53.1				85	41	348.5		348.5
186.0	12934	-57.7				85	39	348.4		348.4
185.0	12967	-58.0				85	39	348.5		348.5
169.0	13525	-62.7				75	54	349.8		349.8
150.0	14260	-68.9				70	54	351.2		351.2
146.0	14421	-70.1				70	53	351.9		351.9
143.0	14541	-70.7				70	52	352.9		352.9
124.0	15366	-74.6				95	41	360.4		360.4
118.0	15653	-76.0				105	35	363.1		363.1
110.0	16060	-77.9				60	8	366.8		366.8
109.0	16113	-78.2				60	8	367.2		367.2
101.0	16554	-80.3				354	8	371.3		371.3
100.0	16610	-79.9				345	8	373.1		373.1
86.0	17450	-84.2				195	8	380.9		380.9
83.2	17634	-85.1				140	10	382.7		382.7
79.0	17921	-83.6				90	16	391.4		391.4
78.0	17991	-83.3				65	16	393.5		393.5
76.4	18106	-82.7				68	17	397.1		397.1
73.5	18326	-74.5				74	21	418.8		418.8
73.0	18365	-74.6				75	21	419.5		419.5
72.0	18445	-74.7				73	16	420.9		420.9
71.0	18527	-72.8				70	10	426.6		426.6
70.0	18610	-70.9				120	6	432.4		432.4
69.1	18687	-68.1				171	8	440.0		440.0
68.0	18783	-68.3				235	12	441.5		441.5
66.0	18960	-68.8				230	14	444.4		444.4
64.0	19143	-69.2				260	16	447.4		447.4
58.0	19728	-70.6				275	8	457.0		457.0
56.0	19937	-71.1				310	16	460.5		460.5
54.0	20153	-71.6				325	12	464.1		464.1
51.3	20458	-72.3				302	9	469.3		469.3
50.0	20610	-69.5				290	8	479.3		479.3
49.0	20731	-67.8				235	6	486.1		486.1
48.7	20768	-67.3				226	5	488.1		488.1
46.2	21084	-69.3				151	2	490.7		490.7
46.0	21110	-69.0				145	2	491.9		491.9
44.0	21378	-66.5				335	10	504.4		504.4
42.0	21660	-63.9				310	19	517.6		517.6
37.7	22323	-62.5				289	33	537.4		537.4
37.0	22438	-62.8				285	35	539.5		539.5
34.1	22939	-64.1				278	32	548.9		548.9
33.0	23142	-63.1				275	31	556.7		556.7
32.0	23332	-62.1				260	31	564.2		564.2
31.0	23528	-61.1				260	25	572.0		572.0
30.0	23730	-60.1				245	21	580.2		580.2
29.0						205	10			
28.0						180	6			
27.0						110	35			
26.0						90	37			
24.0						95	47			
21.0						80	41			

Appendix C. Radiosonde observations from Momote at 00Z on 27 January 2005.

92044 Momote W.O. Observations at 00Z 27 Jan 2004

PRES	HGHT	TEMP	DWPT	RELH	MIXR	DRCT	SKNT	THTA	THTE	THTV
hPa	m	C	C	%	g/kg	deg	knot	K	K	K
1008.0	5	28.8	24.6	78	19.78	0	0	301.3	359.8	304.8
1000.0	71	27.8	22.8	74	17.83	85	2	300.9	353.6	304.1
925.0	760	23.2	19.8	81	15.98	120	6	303.0	350.6	305.9
859.0	1404	19.0	16.6	86	14.03	111	11	305.1	347.3	307.7
850.0	1495	18.8	15.9	83	13.55	110	12	305.8	346.7	308.3
842.0	1576	18.4	15.6	84	13.43	115	12	306.2	346.8	308.7
788.0	2143	15.4	13.6	89	12.58	115	14	308.9	347.3	311.2
753.0	2529	14.8	7.8	63	8.89	115	16	312.3	340.1	313.9
712.0	3000	11.9	5.7	66	8.10	115	17	314.1	339.7	315.6
700.0	3143	11.0	5.0	66	7.87	100	17	314.6	339.6	316.1
691.0	3250	10.3	4.6	68	7.73	85	17	315.0	339.6	316.5
617.0	4184	4.2	0.7	78	6.57	100	23	318.4	339.6	319.6
612.0	4250	3.8	-1.2	70	5.76	101	24	318.7	337.4	319.8
594.0	4492	3.2	-5.3	53	4.34	105	25	320.7	335.2	321.6
587.0	4588	3.0	-7.0	48	3.87	104	25	321.6	334.6	322.3
560.0	4968	0.8	-2.9	76	5.55	101	25	323.3	341.7	324.4
527.0	5454	-1.5	-10.5	50	3.28	97	25	326.2	337.5	326.9
512.0	5682	-3.4	-10.1	60	3.50	95	25	326.6	338.7	327.3
500.0	5870	-4.9	-9.7	69	3.68	90	25	327.0	339.6	327.7
496.0	5933	-5.3	-9.0	75	3.92	88	26	327.3	340.7	328.0
489.0	6045	-5.7	-11.6	63	3.23	85	27	328.1	339.3	328.7
466.0	6422	-7.2	-20.5	34	1.61	70	25	330.8	336.7	331.1
464.0	6456	-7.3	-21.3	32	1.51	71	25	331.1	336.6	331.4
445.0	6780	-9.3	-18.9	46	1.94	80	21	332.5	339.6	332.9
434.0	6975	-10.5	-17.5	56	2.24	110	14	333.4	341.5	333.8
415.0	7318	-12.1	-22.0	44	1.59	90	16	335.6	341.5	336.0
408.0	7449	-12.7	-23.7	39	1.39	95	16	336.5	341.7	336.8
400.0	7600	-13.9	-24.9	39	1.28	100	16	336.8	341.6	337.1
390.0	7791	-15.6	-27.3	36	1.05	105	14	337.1	341.1	337.3
386.0	7869	-16.3	-28.3	35	0.97	98	14	337.1	340.8	337.3
370.0	8186	-19.1	-27.1	49	1.13	72	17	337.5	341.8	337.7
369.0	8206	-19.1	-27.0	50	1.14	70	17	337.8	342.1	338.0
360.0	8390	-19.1	-26.2	53	1.26	85	17	340.2	345.0	340.4
359.0	8411	-19.1	-26.1	54	1.27	85	17	340.4	345.3	340.7
341.0	8792	-22.5	-27.5	64	1.18	85	17	340.9	345.4	341.1
331.0	9008	-24.0	-31.2	51	0.85	85	17	341.7	345.1	341.9
316.0	9346	-26.3	-37.1	36	0.50	70	12	343.1	345.1	343.2
311.0	9462	-27.1	-39.1	31	0.42	70	12	343.5	345.2	343.6
300.0	9720	-29.3	-44.3	22	0.25	70	14	344.0	345.0	344.0
292.0	9912	-30.7	-46.6	20	0.20	60	17	344.6	345.5	344.7
291.0	9936	-30.9	-46.9	19	0.19	61	17	344.7	345.5	344.7
277.0	10283	-33.9	-40.9	49	0.39	74	14	345.3	346.9	345.3
276.0	10308	-34.1	-41.7	46	0.36	75	14	345.3	346.8	345.4
270.0	10461	-35.3	-46.3	32	0.22	72	14	345.8	346.7	345.8
263.0	10642	-36.9	-42.9	54	0.33	68	15	346.0	347.4	346.1
258.0	10774	-37.9	-48.2	33	0.19	65	16	346.4	347.3	346.5
256.0	10828	-38.3	-50.3	27	0.15	69	16	346.6	347.3	346.7
250.0	10990	-39.7	-47.7	42	0.21	80	16	346.9	347.8	346.9
248.0	11045	-40.2				85	16	347.0		347.0
229.0	11586	-44.9				78	16	347.8		347.8
210.0	12160	-49.7				70	17	349.0		349.0
207.0	12256	-50.5				71	17	349.2		349.2
200.0	12480	-52.7				75	17	349.1		349.1
199.0	12512	-53.3				75	17	348.7		348.7
186.0	12940	-56.8				80	16	349.8		349.8
178.0	13219	-59.1				74	17	350.5		350.5
162.0	13799	-63.4				60	21	352.8		352.8
154.0	14111	-65.7				60	16	354.0		354.0
150.0	14270	-67.1				60	14	354.3		354.3
149.0	14310	-67.5				60	14	354.4		354.4
138.0	14768	-71.5				37	11	355.1		355.1
117.0	15725	-78.9				347	6	358.6		358.6
109.0	16124	-83.1				326	3	358.0		358.0
105.0	16330	-84.3				315	2	359.5		359.5
100.0	16600	-85.9				225	8	361.5		361.5
95.0	16877	-87.3				245	12	364.1		364.1
88.0	17291	-89.4				185	14	367.9		367.9
83.0	17607	-91.0				180	10	370.8		370.8
80.5	17773	-91.9				150	16	372.3		372.3
74.0	18229	-86.1				100	29	393.6		393.6
72.5	18340	-84.7				93	34	398.9		398.9
71.1	18450	-77.3				86	39	416.8		416.8
70.5	18499	-77.1				83	41	418.3		418.3
70.0	18540	-77.5				80	43	418.3		418.3
67.0	18789	-78.8				75	47	420.7		420.7
65.0	18961	-79.7				65	38	422.4		422.4
64.5	19005	-73.5				63	35	436.9		436.9
64.0	19052	-73.1				60	33	438.7		438.7
60.0	19435	-70.0				80	27	454.0		454.0
58.0	19637	-68.3				90	31	462.1		462.1
54.8	19975	-65.5				80	26	476.1		476.1
52.1	20280	-66.3				70	22	481.1		481.1
52.0	20292	-66.2				70	21	481.6		481.6
50.0	20530	-64.5				95	17	491.1		491.1
49.0	20654	-63.9				110	19	495.4		495.4
48.0	20781	-63.2				115	16	499.9		499.9
46.4	20990	-62.1				151	14	507.4		507.4
46.0	21043	-62.4				160	14	508.1		508.1
45.0	21177	-63.0				155	14	509.8		509.8
43.0	21455	-64.3				115	14	513.2		513.2
41.0	21747	-65.6				105	10	516.9		516.9
39.5	21975	-66.7				80	17	519.7		519.7
39.0	22053	-66.1				75	19	523.1		523.1
37.0	22375	-63.8				65	31	537.0		537.0
36.0	22543	-62.6				65	19	544.4		544.4
35.3	22663	-61.7				100	17	549.7		549.7
35.0	22716	-62.0				115	16	550.2		550.2
34.0	22893	-63.1				135	23	551.9		551.9
31.1	23440	-66.5				130	38	557.0		557.0
31.0	23459	-66.1				130	39	558.6		558.6
30.2	23619	-62.9				110	22	571.5		571.5
30.0	23660	-63.3				105	17	571.5		571.5
28.0	24089	-61.3				125	6	588.4		588.4
26.1	24525	-59.3				2	8	606.0		606.0
26.0	24549	-59.5				355	8	606.1		606.1
25.0	24794	-61.5				7	7	607.2		607.2
24.0	25056	-58.6				20	6	622.7		622.7
23.0	25330	-55.6				80	25	639.2		639.2
22.0	25616	-52.5				80	27	656.8		656.8
21.0	25916	-49.1				60	19	675.5		675.5
20.0	26230	-45.7				305	29	695.5		695.5
19.8	26297	-45.5				303	32	698.1		698.1
18.0	26923	-48.3				285	58	708.6		708.6
15.9	27738	-51.9				265	41	722.4		722.4
15.0	28115	-52.5				255	33	732.4		732.4
14.8	28202	-52.7				247	31	734.7		734.7
14.0	28564	-49.0				215	23	758.8		758.8
13.8	28658	-48.1						765.1		765.1